The Pennsylvania State University

The Graduate School

Eberly College of Science

ORGANOMETALLICS FOR THE DEVELOPMENT OF SELF-MOTILE AND CRACK REPAIR SYSTEMS

A Dissertation in

Chemistry

by

Ryan A. Pavlick

Submitted in Partial Fulfillment

of the Requirements

for the Degree of

Doctor of Philosophy

August 2013

The dissertation of Ryan A. Pavlick was reviewed and approved* by the following:

Ayusman Sen
Distinguished Professor of Chemistry
Dissertation Advisor
Chair of Committee

Tom Mallouk
Evan Pugh Professor of Materials Chemistry and Physics

Ben Lear
Assistant Professor of Chemistry

Darrell Velegol
Distinguished Professor of Chemical Engineering

Barbara Garrison
Head of the Department of Chemistry

*Signatures are on file in the Graduate School

Abstract.

Since 2004, research into nano and microscopic motors has exploded in the literature. The main focus of these endeavors has been using catalytic reactions to power such motors in a directed manner. Research beyond the basic concept is currently explored, such as using powered systems to drive pumps, transport materials, and even looking at self-assembly. While there are many aspects to this research, my research has focused on using organometallic systems to accomplish directed motion and to utilize them to create systems with real world applications.

Chapter 1 of this thesis provides an introduction to the physics involved in creating powered systems. Mechanisms to achieve directed motion are also reviewed.

Chapter 2 focuses on the development of an organometallic catalysis powered motor. This motor uses a polymerization reaction to achieve directed motion and enhanced diffusion. The chemotactic ability of these motors is evaluated.

Chapter 3 looks at using a single molecular catalyst, Grubbs' catalyst, as a catalytically powered motor. This motor displays enhanced diffusion while performing ring-closing metathesis. The diffusion of this system is evaluated via NMR diffusion spectroscopy.

Chapter 4 expands on the previous chapter and delves into potential mechanisms. The interaction between the catalysts and the environment are probed. It is evaluated that there is a coupling phenomenon between catalyst molecules that leads to the observed powered motion.

Chapter 5 explores a crack repair and detection system based on the Grubbs' polymerization reaction. This system utilizes salt-powered transport to direct reagents to a

damaged surface. The damaged is detected by using fluorescent particles or the surface is repaired by using polymerization reagents.

Chapter 6 concludes the research presented. It also provides a general outlook and perspective on motors research in general.

Table of Contents

LIST OF FIGURES…….....vii

LIST OF TABLES……..xiii

ACKNOWLEDGEMENTS……..xv

Chapter 1 Introduction…….....1
1.1 Mechanisms of Motility…….....2
1.2 Non-electrolyte Diffusiophoresis……3
1.3 Electrolyte Diffusiophoresis……5
1.4 Electrophoresis……7
1.5 Other Phoretic Mechanisms……8
1.6 Bubble Propulsion……9
1.7 Chemotaxis……10
1.8 The Use of Organometallics as Power Sources……10
1.9 References…….....11
Chapter 2 Polymerization Powered Motor……13
2.1 Introduction……...13
2.2 Synthesis…….....14
2.3 Characterization……..18
2.3.1 XPS Analysis of the Motors…….....18
2.3.2 Activity Assay……..18
2.3.3 SEM……...21
2.4 Calculation of Diffusion Coefficient……23
2.5 Evaluation of the Mechanism of Motility…….....30
2.5.1 Osmophoresis……..30
2.5.2 Thermal Effect……31
2.6 Chemotaxis……..33
2.7 Conclusion……...38
2.8 References…….....39
Chapter 3 A Catalytically Driven Organometallic Molecular Motor……..40
3.1 Introduction……40
3.2 NMR Diffusion Measurements……..42
3.3 Measurement of turnover frequency (TOF)…….....48
3.4 Enhanced Diffusion Mechanism……...50
3.4.1 Structural Changes……50
3.4.2 Density functional theory calculations of molecular volume, radius and energetics……54
3.5 ^{31}P NMR spectroscopy of the phosphine ligand……...55

3.6 Phoretic Effect……56
3.7 Efficiency……57
3.8 Conclusion……59
3.9 References……59
Chapter 4 Dynamic Coupling at the Nanoscale……62
4.1 Introduction……62
4.2 Calculation of Diffusion Coefficient……64
4.3 Diffusion of a Spectator (DCM)……67
4.3.1 Increasing the amount of DCM……71
4.4 Measurement of Rate……71
4.5 Dependence on Reaction Rate……73
4.6 Dependence on Total Rate of a Polymer Tracer……75
4.7 Effect of catalyst concentration at a Constant Reaction Rate……78
4.8 Calculation of Power Output……80
4.9 Theory……81
4.10 Conclusion……82
4.11 References……82
Chapter 5 Salt Triggered Detection and Polymer Deposition……84
5.1 Introduction……84
5.2 Salt Flows……88
5.2.1 Coating Synthesis……88
5.2.2 Observation of Flows……88
5.3 Quantum Dot Based Detection……90
5.3.1 Confocal Experiments……90
5.4 Repair of Damaged Polymer Film……94
5.4.1 Emulsion Fabrication……94
5.4.2 Stability of Emulsions in Varying Ionic Strengths……95
5.4.3 Salt Triggered Polymer Deposition……97
5.4.4 Analysis of Polymer Deposition via Micro AT-IR……99
5.5 Conclusions……100
5.6 References……100
Chapter 6 Conclusions……102

LIST OF FIGURES

Figure 1-1: Diagram showing the active mechanism for the polymerization powered motor. Fluid flows from low concentration to high concentration causing the motor to move in the opposite direction……5

Figure 1-2: Scheme for Pt/Au bimetallic rod movement in hydrogen peroxide solution…….8

Figure 2-1: Structure of the bound Grubbs catalyst as attached to the silica side of a 0.96 μm Au-Silica Janus microsphere……15

Figure 2-2: Schematic for monolayer synthesis and evaporation of metals to form Janus Particles……16

Figure 2-3: Reaction scheme for the attachment of Grubbs' catalyst to the gold-silica Janus microspheres……17

Figure 2-4: The calculated turnover frequency (TOF) in nmol/g s for 0.01, 0.1, 0.5, and 1 M norbornene solutions in dichloromethane versus concentration. The plot begins to level off as the momomer concentration approaches 1 M…….....19

Figure 2-5: NMR spectrum in $CDCl_3$ of polynorbornene produced by the polymerization motors……20

Figure 2-6: Scale bar = 400nm (A) SEM image of as synthesized Au-Silica Janus motor particles. (B) SEM image of motor particles after exposure to a monomer solution showing clear polymer deposition on the motor surface. This is most prevalent on the silica side where the catalyst is bound……..22

Figure 2-7: (A) Calculated diffusion coefficients of the Janus Motors at varying monomer concentrations**.** The diffusion coefficients exhibit a steady increase over the monomer concentrations (red). After treatment with an inhibitor there was a significant decrease in the diffusion coefficient (blue) showing that the enhanced diffusion was a result of substrate turnover. (B) Plot of the diffusion coefficient versus the natural logarithm of turnover frequency at the same monomer concentration. This shows a linear relationship between the two parameters with the intercept through the expected diffusion coefficient without fuel……28

Figure 2-8. Temporal particle tracks of the Janus motor with no fuel (red) and in 0.5 M norbornene (blue). Each point represents a displacement in μm over 0.5 sec, beginning from the origin over a 20 sec time span. The motor particles in the fuel show longer displacements in a single direction……...29

Figure 2-9: The Janus motor consumes monomers at the silica face creating an area of low monomer concentration. Fluid in the low concentration region flows towards the higher concentration region at the gold face. Consequently the motor moves in the opposite direction…….31

Figure 2-10. Normalized particle population at the gel edge as a function of time. The populations were normalized so that the initial population is taken to be 1. The motor particles in a norbornene gradient (red) exhibit a higher average agglomeration at the gel over both unfunctionalized Au-Silica Janus spheres in norbornene gradient (blue) and motor particles in a norbornane gradient (green)……....35

Figure 3-1: Structure of Grubbs' 2nd generation catalyst and reaction scheme for the cross metathesis (CM) of 1-pentene and the ring closing metathesis (RCM) of diethyl diallylmalonate……42

Figure 3-2: (A) Diffusion coefficients of Grubbs' catalyst over a range of concentrations of DDM. The diffusion increases as the concentration is increased saturating at around 0.1 M. (B) Diffusion coefficient of the catalyst with the addition of an inhibitor and after the reaction has reached equilibrium. The diffusion coefficient is reduced to the base value in presence of the inhibitor and when the reaction reaches equilibrium……..46

Fig 3-3: Diffusion coefficient at various concentrations of 1-pentene. Controls were run with inhibitor and after the reaction was completed. No significant change in diffusion was observed……...47

Figure 3-4: Structure of diethyl diallyl malonate…….48

Figure 3-5: Correlation between diffusion coefficient and turnover frequency…….....50

Figure 3-6: Structural changes to the catalyst molecule during the catalytic cycle……...52

Figure 3-7: DFT calculated structures for (top left) $(H_2IMes)(PCy_3)Cl_2Ru=CHPh$, (bottom left) $(H_2IMes)(PCy_3)Cl_2Ru=CH_2$, (top right) $(H_2IMes)Cl_2Ru=CHPh$ (bottom-right) $(H_2IMes)Cl_2Ru=CH_2$, showing the change in effective radius during the catalytic cycle…….53

Figure 4-1: Schematic of the motor molecule catalyzing the ring closing metathesis of diethyl diallylmalonate……...64

Figure 4-2: The change in diffusion coefficient of the catalyst as a function of reaction rate for four different catalyst concentrations. For each catalyst concentration, diffusivity

increases with increasing DDM concentration due to the increase in total reaction rate in thesystem.……66

Figure 4-3: (A) The change in diffusion coefficient of DCM as a function of reaction rate for four different catalyst concentrations. For each catalyst concentration, the diffusion increases with increasing DDM concentration due to the increase in total reaction rate in the system. (B) The change in diffusion coefficient of DCM in the presence of 1-pentene and DDM as a function of reaction rate. The cross metathesis of 1-pentene produced no significant increase in diffusion when compared to the ring closing metathesis of DDM, especially at higher rates……69

Figure 4-4: The diffusion of DCM was measured as the amount of DCM was increased compared to the catalyst concentration. There was a slight decrease in diffusion as the amount was raised from 5 times to 50 times.……71

Figure 4-5. The change in diffusion of the catalyst was plotted against reaction rate of the system (mol sub. /s). The trend is generally linear, especially at high catalyst concentration. ……..74

Figure 4-6. The change in diffusion of the catalyst was plotted against reaction rate of the system (mol sub. /s). The trend is generally linear but seems to saturate off at higher rates.……75

Figure 4-7. The change in diffusion coefficient of the PDMS as a function of reaction rate for four different catalyst concentrations. For each catalyst concentration the diffusion increases with increasing DDM concentration due to the increase total in reaction rate in the system.……76

Figure 4-8. The change in diffusion of the polymer was plotted against reaction rate of the system (mol sub. /s). The trend is generally linear.……77

Figure 4-9. Diffusion of the catalyst as a function of catalyst concentration at a constant rate of 6.7 $x10^{-8}$ mol sub/ sec. There is no consistent trend between the diffusion and catalyst concentration suggesting that the number a reaction centers does not matter.……..79

Figure 4-10. Diffusion of the spectator DCM as a function of catalyst concentration at a constant rate of 6.7 $x10^{-8}$ mol sub/ sec. There is no clear trend between the diffusion and catalyst concentration suggesting that the number a reaction centers does not matter.……..80

Figure 5-1: Diagram of the surface coating setup. The calcium chloride is mixed into a PDMS layer and sealed with a thin layer of PDMS. The surface is scratched, exposing the calcium chloride to the water causing an increase in the ionic strength. The quantum dots (Q-dots) then begin to aggregate due to the decreased electrostatic repulsion.…….86

Figure 5-2: Schematic using salt/PDMS film as a coating for a repair system. The catalyst emulsions (red) and monomer emulsions (grey) flow over the crack due to density driven flows. At the crack the emulsion stability is perturbed due to the high ionic strength, and the emulsions begin to break apart and aggregate. This process causes polymer deposition.…….87

Figure 5-3: Inverted (top) and upright (bottom) setups showing the flow patterns (blue) caused by the salt leaching. The dependence of the flow direction on gravity suggests the flows are density driven……..……...89

Figure 5-4: Fluorescence confocal imaging of the crack at 5 min and 35 min (Scale bar = 325 μm). The fluorescence intensity remains constant in the crack while the quantum dots

outside the crack move away around the crack, showing a more defined fluorescence from the damaged site…….91

Figure 5-5. Fluorescence intensity ratio of the intensity in the crack divided by the intensity 100 μm away from the crack as a function of time. Run 1 shows the ratio change for the images in Figure 5-4. Run 1 and the control dhows the ratio change for the images in Figure 5-7. The ratio in run 1 increases linearly while in run 2 the increase is slightly exponential. However, the control shows no significant increase……..…….92

Figure 5-6: Image of the crack with a quantum dot solution a) with and b) without $CaCl_2$ after 1 hour. The quantum dots clearly concentrate at the crack when there is salt……..93

Figure 5-7: Fluorescence confocal images of carboxylated quantum dots over a crack in pure PDMS over time (Scale bar = 325μm). The fluorescence in and around the crack does not change with time…….93

Figure 5-8: Optical Images of oil in water emulsions containing dicyclopentadiene (left, scale bar = 25 μm) and Grubbs' 2nd generation catalyst (right, scale bar = 50 μm)……...95

Figure 5-9: a) Graph displaying the number of particles observed at 100x as a function of concentration. There is a clear dramatic drop in concentration as the $CaCl_2$ concentration approaches 0.1 M. c) Picture of the solution of oil-in-water emulsions after 20 hrs. The 0M and 0.01M salt solutions are still turbid while the high salt concentrations are clear and show floating polymer deposits……..96

Figure 5-10: ESEM images of selected areas of the cut showing polymer deposition (Scale bar = 50 μm). a) The image of cut before treatment with emulsions. b) Cut in polymer with no salt c) $CaCl_2$ inverted after 1hr exposure to emulsions…….98

Figure 5-11: Micro AT-IR spectrum showing key peaks for polyDCPD (1665 cm^{-1} and 956 cm^{-1} for the acyclic C=C and acyclic =C-H respectively) compared to the flat spectrum for the unrepaired crack…….99

LIST OF TABLES

Table 2-1: The diffusion coefficients of Janus motors normalized for change in viscosity of the medium…….24

Table 2-2: Mean squared displacements for each time step of Janus motors……...25

Table 2-3: Calculated velocities at varying monomer concentrations for Janus Motors…….26

Table 2-4. Diffusion coefficients for uniformly coated silica particles (uniform motors)…..**.....**27

Table 2-5: Average normalized particle concentrations over the 4 h in chemotaxis experiment…….36

Table 2-6: Statistical analysis of a) motor particles in norbornene versus Au-Silica Janus spheres in norbornene and b) motor particles in norbornene versus motor particles in norbornane…….**.....**37

Table 3-1: Average diffusion coefficients, D, of Grubbs' catalyst in the presence of diethyl diallyl malonate (DDM)…….**.....**44

Table 3-2: Average diffusion coefficients, D, of Grubbs' catalyst measured in the presence of 1-pentene……..45

Table 3-3: TOF for the catalyst at varying concentrations of DDM and the concentration of substrate after the initial 15min equilibration period……49

Table 3-4: Calculated effective radii from DFT of various intermediates……..54

Table 3-5: ^{31}P NMR data for Grubbs' 2nd generation catalyst in the absence and presence of substrates……...56

Table 4-1: Diffusion coefficients of the catalyst measured over a range of catalyst concentrations and rates. The T and P values were calculated by performing a two tailed equal variance T-test against the diffusion coefficient with no substrate.……...67

Table 4-2: Diffusion coefficients of dichloromethane (DCM) measured over a range of catalyst concentrations and rates. The concentration of DCM was 0.03 M. The T and P values were calculated by performing a two tailed equal variance T-test against the diffusion coefficient with no substrate.……..**.....**70

Table 4-3: Turnover frequencies and reaction rates of the catalyst at different substrate and catalyst concentrations.……72

Table 4-4: Diffusion coefficients of monoglycidyl ether-terminated poly(dimethylsiloxane) M_n ~5000 (PDMS) measured over a range of catalyst concentrations and rates. The concentration of PDMS was 1.6 μM. The T and P values were calculated by performing a two tailed equal variance T-test against the diffusion coefficient with no substrate.……..……78

Acknowledgement

First, I would like to thank my thesis advisor, Prof. Ayusman Sen. His constant guidance has allowed me to accomplish my thesis work and become an able chemist. Also his willingness to support my ideas has led to several publications. Next I would like to thank Prof. Tom Mallouk for being an excellent thesis advisor and always providing me with more questions to answer. Also, Prof. John Badding and Prof. Benjamin Lear, as committee members, have provided useful perspective as scientists outside my area of study. Finally, I would like to thank Prof. Darrell Velegol for providing me with knowledge of hydrodynamics and colloidal chemistry. He has given me great advice many times on my research.

Outside of my thesis committee I would like to thank Dr. Alan Benesi for his help with learning and utilizing the NMR. Also, a thank you to Dr. Emmanuel Hatzakis and Wenbin Luo for helping me with several NMR experiments. I would like to thank members of the MCL and Nanofab including Josh Stapleton, Bangzhi Liu, and Vince Bojan. Finally a big thank you to NSF MRSEC and the Air Force Office of Scientific Research for funding.

I would like to thank all my lab mates especially Samundra Sengupta for training me when I first arrived in 2009. Mike Ibele, for showing me the Zen of being a grad student and sharing his profound knowledge. Frances Pong for listening to me ramble when I needed someone. I would like to thank my two undergrads, Timothy McFadden (who still owes me a drink), and Stephen Meckler for doing excellent work beyond the requirements of an undergrad. Vinita Yadav, who I trained and who has become a very accomplished chemist. Krishna Dey, for

showing me the power of working with a physicist. Isamar Ortiz and Flory Wong, for being my coffee and snack buddies. And a big thank you to the rest of my labmates Sambeeta Das, Hua Zhang, Can Zhang, Wentao Duan, Scott Biltek, Deb, Dave, Matt, Eve, Ying, and Shak. But most of all I would like to thank the Care Bears for helping me enforce lab safety.

Outside of my lab I would of course like to thank my parents, Marilyn Pavlick and William Pavlick, for supporting me in my endeavors. Thank you to Casey Kilpatrick, for being my external coffee buddy, confidant, and good friend. Andrew Sirjooshish for doing spectacular computation work for my research. A big thank you to my lovely girlfriend Christine Weyde for all her support, love, and awesome cooking. A thank you to Derek Keefer for helping me keep my head in the game. Also a thank you to David Kirby for being a good roommate and excellent friend.

Chapter 1

Introduction

The study, synthesis, and application of nano- and micron-sized self-powered objects and systems are areas of great interest due to their potential use in drug delivery systems, self-assembly, and cargo delivery applications. The advantage of exploring these in synthetic systems is that the motors operate in the same size scale and the physics is identical to many biological systems including bacteria, cells, and proteins. As objects become smaller the physics that dominates their motion begins to deviate from the everyday classical Newtonian physics. At these scales, inertial forces become less important to motion and viscous forces begin to dominate. The Reynold's number (Re) describes the ratio of inertial forces to viscous forces and its magnitude provides information on which of these two forces dominates the motion of the object of interest[1]

$$Re = \frac{\rho V l}{\eta} \tag{1-1}$$

where ρ is the density of the medium, V is velocity, l is length, and η is viscosity. Other forces that affect the motion of objects at low Reynold's numbers are the rapid thermal "bumping" of the solvent particles against the objects' surface. This effect creates what is known as Brownian motion, where the objects are driven to "move" and diffuse in a solution. The diffusion coefficient for an object is then defined as:

$$D = \frac{kT}{f} \tag{1-2}$$

where k is the Boltzmann constant, T is the temperature in Kelvin, and f is the viscous drag coefficient which changes based on the geometry of the system (for a sphere, this is $6\pi\eta a$).[2] Thermal "bumping" also causes an object to rotate, known as Brownian rotation. The frequency of this rotation for a sphere is defined by the equation:

$$\tau_R = \frac{kT}{8\pi\eta a^3} \tag{1-3}$$

where τ_R is the rotational coefficient, k is the Boltzmann constant, T is the temperature in Kelvin, η is the viscosity of the solution, and a is the radius of the particle.[2] This is important to consider in creating self-powered motors for if the motor is rotating (tumbling) too fast it will move in a more random fashion and be less directional. Creating powered motion at low Reynold's number regimes requires methods to overcome both viscous forces and Brownian effects. This leads to the necessity of generating surface forces, whereby surface forces move the fluid across the surface circumventing the viscous drag.

1.1 Mechanisms of Motility.

Most motility mechanisms require the creation of a gradient across the particle surface, where there is a change in some property (temperature, surface tension, concentration, etc.) over a given distance. In other words, a non-equilibrium condition has to be applied to the particle to generate directed motion. The gradient gives rise to a force that acts on the fluid at the surface of the object which is then made to flow causing the object to move in the opposite direction.

1.2 Non-electrolyte Diffusiophoresis

Non-electrolytic diffusiophoresis is movement, which is caused by a gradient of uncharged solutes across a surface. These solutes interact with the surface with a certain potential determined by the Gibbs' absorption length, K, and the length of the particle-solute interaction, L. The overall equation that defines the velocity of a particle in the gradient is,

$$U = \frac{kT}{\eta} KL\, \nabla C \tag{1-4}$$

where k is the Boltzmann constant, T is the temperature of the solution, η is the solution's viscosity, and ∇C is the concentration gradient of the solute.[2] The direction of particle movement depends on whether the particle-solute interaction is repulsive or attractive. Based on a gradient of small neutral particles, Anderson can give an estimation for a typical velocity. A good approximation for KL for small molecules is 5.8 x 10^{-16} cm^2 and, assuming a reasonable solute gradient of 0.1 mole/cm^{-4}, this results in a velocity of 1.4 μm/s in water at room temperature. If the solute molecules are bigger, an approximation for KL is given by the equation,

$$KL = \frac{a^2}{2} \tag{1-5}$$

where a is the solute's radius. This non-electrolyte mechanism was confirmed experimentally by Stafford and Quinn who tracked the motion of particles in a stop flow cell in a gradient of dextran and polymer nanoparticles.[3] They showed that the particles traveled down the gradient. The reason behind this movement is that the solute sterically excludes solvent from the particles surface. This exclusion leads to areas of high and low solvent pressure, which caused the fluid to flow. In this case, the fluid flowed up the gradient allowing the particles to move down the gradient.

The above mechanism, as first postulated, affected a relatively large area. The same mechanism, however, can function in some form on a smaller scale, leading to bots that generate their own gradients via catalytic reactions. This mechanism, sometimes referred to as the osmotic mechanism in relation to particles, functions by a catalytic motor depleting surrounding reactant molecules at the catalyst end creating an osmotic force around the motor.[4] This force then drives the motion of the bot. An example that is believed to function by this mechanism is the polymerization motor reported by Pavlick et al.[5] This motor was fabricated from an asymmetric gold/silica Janus particle that was coated with a polymerization catalyst on the silica face. This motor exhibited a 70% increase in diffusion when placed in a solution of monomer. Since the motor depletes monomer molecules at the catalyst face and releases very few polymer molecules, this creates a gradient of monomer around the particle. Fluid will then flow towards the area with a high concentration of monomer (silica face) propelling the particle catalyst end forward (Figure 1-1).[5]

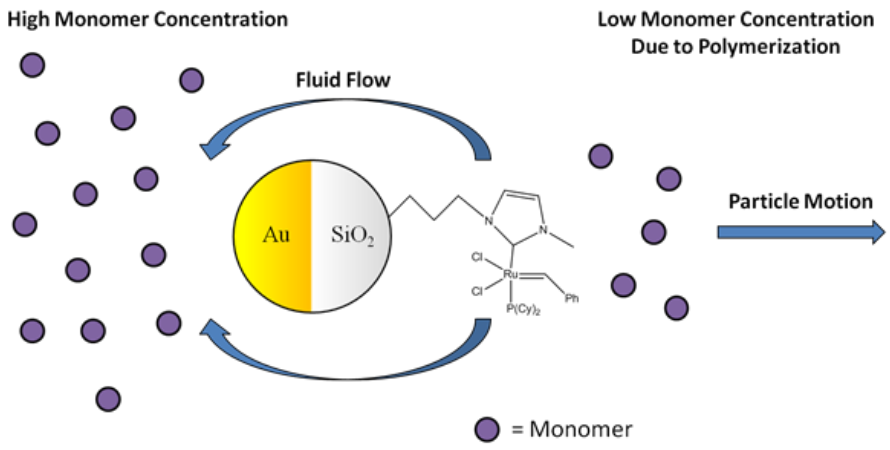

Figure 1-1: Diagram showing the active mechanism for the polymerization powered motor. Fluid flows from low concentration to high concentration causing the motor to move in the opposite direction.[5]

There are other proposals on how non-electrolyte motor systems can function. The inverse of the above osmotic motor has been explored where one side of the particle creates more products than reactants.[6] One example of a motor that functions this way involves platinum/silica Janus particles.[7,8] The platinum side of these particles decomposes hydrogen peroxide into water and oxygen. This decomposition creates an oxygen gradient across the particle. The gradient then creates a force that acts on the motor causing it to move in a directed fashion.

1.3 Electrolyte Diffusiophoresis

Another powerful transport mechanism is electrolyte diffusiophoresis. This mechanism works when a gradient of electrolytes is formed across a charged surface. For diffusiophoresis near a wall, there are two effects contributing to the movement of a particle: an electrophoretic effect and a chemophoretic effect, and the speed of the diffusiophoretic movement can be approximated by Equation (1-6)[9]:

$$U=\underbrace{\left[\frac{\mathrm{dln(C)}}{\mathrm{dx}}\right]\left[\frac{D_C-D_A}{D_C+D_A}\right]\left[\frac{k_BT}{e}\right]\left[\frac{\varepsilon(\zeta_p-\zeta_w)}{\eta}\right]}_{\text{Electrical Field Term}}+$$
$$\underbrace{\left[\frac{\mathrm{dln(C)}}{\mathrm{dx}}\right]\left[\frac{2\varepsilon k_B^2T^2}{\eta e^2}\right]\left\{\ln\left[1-\tanh^2(\frac{e\zeta_w}{4k_BT})\right]-\ln\left[1-\tanh^2(\frac{e\zeta_p}{4k_BT})\right]\right\}}_{\text{Chemophoretic Term}} \quad (1\text{-}6)$$

where U is the particle velocity, k_b is the Boltzmann constant, T is temperature in Kelvin, κ^{-1} is the Debye length, *e* is the charge of an electron, $\nabla\ln(C)$ is the gradient of the electrolyte, D^+ is the diffusion coefficient of the cation, D^- is the diffusion coefficient of the anion, ζ_P is the zeta potential of particles, and ζ_W is the zeta potential of the wall. As shown in Equation (1-6), electrophoresis results from a difference in diffusion between the cation and anion which contributes to the ion gradient in a given direction. This difference leads to a net electric field, which acts both electrophoretically on the *nearby* particles and osmophoretically on the ions adsorbed in the double layer of the wall. Also, the concentration gradient of the electrolytes causes a gradient in the thickness of the electric double layer, and thus a "pressure" difference along the wall is created. As a result, the solution will flow from the area of higher electrolyte concentration to that of lower concentration, known as the chemophoretic effect. The combination of electrophoretic and chemophoretic effects leads to an overall diffusiophoretic flow, which powers the movement of particles. The enhanced movement of the enzyme urease in the presence of its substrate is thought to be a result of this mechanism. In the presence of the enzyme, urea is converted to ammonium and hydroxide ions, the latter which having a significantly higher diffusion coefficient.[10] Other examples include the silver chloride and gold schooling motors, which school due to overlapping ion gradients.[11, 12] More recently, pump systems have been developed based on this mechanism.[13]

Each of the two previously mentioned mechanisms has their own set of advantages. Non-electrolyte diffusiophoresis has no dependence on surface charge and is able to function in high ionic strength media. Electrolyte diffusiophoresis, however, is not effective in high ionic strength media because as the double layer collapses, the net electric field cannot act on the particle surface resulting in a velocity of zero. Conversely, in a low ionic strength medium electrolyte diffusiophoresis is a more powerful mechanism resulting in higher speeds. This is shown qualitatively by considering that the chemophoretic component of electrolyte diffusiophoresis has similar origins as non-electrolyte diffusiophoresis. Both of these mechanisms occur by the chemical species responsible for the gradient being attracted to the surface either by electrostatic (electrolyte) or through van der Waals (non-electrolyte) interactions. If these two effects are comparable, the electrolyte diffusiophoresis is stronger because it has an additional electric field term (Equation 1-6).

1.4 Electrophoresis

Electrophoresis is the movement of charged objects in an electric field. Typically, an electric field is applied across a suspension of particles in a fluid. This electric field drives the motion of the charges on the surface of the object creating a slip velocity, whereby the fluid is allowed to flow around the particle. The particle is thus driven in the opposite direction at a velocity U governed by the equation,

$$U = \frac{\varepsilon \zeta E}{\eta} \tag{1-7}$$

where ε is the dielectric constant of the solution, ζ is the zeta potential of the particles, E is the magnitude of the electric field, and η is viscosity.[2] Redox reactions occurring at the two ends of an object can result in an electric field similar to an externally applied field resulting in motion. The Pt/Au nanorod motor discovered by Paxton et al. functions by this mechanism; the catalytic decomposition of hydrogen peroxide localizes the field to the length of the rod (Figure 1-2)[14]. Recently, Liu et al. synthesized a copper-platinum nanowire battery that was self-propelled in bromine and iodine solutions via the oxidation of copper and the concomitant platinum catalyzed reduction of the halogen.[15]

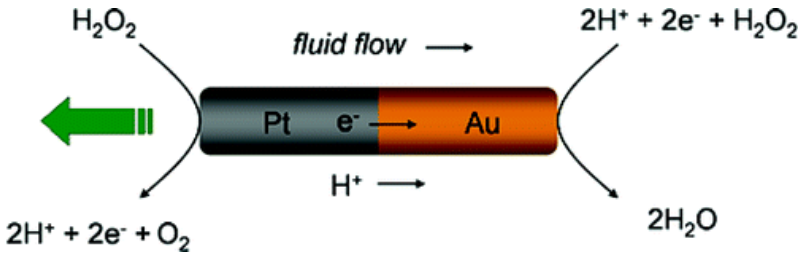

Figure 1-2: Scheme for Pt/Au bimetallic rod movement in hydrogen peroxide solution.

1.5 Other Phoretic Mechanisms

There are also less explored (in terms of motors research) yet still significant phoretic mechanisms that have been used to engineer motion of nanoscale objects. Magnetophoresis, motion due to a gradient of a magnetic field, has been used extensively in biological applications such as separations.[16] Thermal gradients, also known as thermophoresis and/or Soret effect, have been employed in some systems, and finally movement due to surface tension gradients known

as Marangoni effect have been described in droplet and bubble systems[17-19]. The general concept here is that by creating a gradient across an object, an entropic force is generated causing directed movement. More recently, a gradient of light has been used to direct the motion of a particle coated by azobenzene molecules.[20]

1.6 Bubble Propulsion

Another way to create motion is via bubble propulsion. Motors that utilize this type of motion create bubbles on their catalytic side and the force from the release of the bubble causes the motion known as bubble recoil. This is a gradient-like mechanism since bubbles need to be generated on one side and not the other so there is a change in bubble concentration with distance. Building on earlier work by Whitesides[21], the most effective motor to utilize this mechanism was first synthesized by Schmidt and Sanchez and later improved upon by Wang's lab.[22-24] The motor consists of a rolled up microtube with an exposed platinum surface on the inside. The platinum decomposes hydrogen peroxide present in solution to form oxygen and in the confined volume of the tube the oxygen molecules coalesce to form oxygen bubbles. These bubbles are then released out of the larger open end (one end always ends up being slightly larger than the other). Motor speeds of hundreds of microns per second have been reached using this method. An advantage of this motor is that it is able to work in high ionic strength systems, where other motors often fail. This allows for their use in biological systems and by adding recognition sites to these motors, it is possible to transport specific cargo including cancer cells.[24]

1.7 Chemotaxis

Chemotaxis is a common phenomenon observed in biological systems[25] and recently it has been shown in some non-biological systems as well. Unlike biological systems, the mechanism for chemotaxis is not well understood in the latter systems. According to a hypothesis put forth by Hong et al., when a catalytic motor experiences different diffusivities at different substrate (fuel) concentrations it will chemotaxis towards areas of higher diffusivity.[26] Movement occurs in this direction because, with higher diffusivity, the motor experiences a higher average displacement. It will continue to move further as it travels up the gradient.[26] This was demonstrated experimentally by the authors by placing Pt/Au nanorods in a gradient of hydrogen peroxide. Over time the density of rods began to increase in the area of the highest concentration of hydrogen peroxide (where the diffusivity was highest). Another example comes from Pavlick et al. who observed that when their polymerization motor was placed in a concentration gradient of the monomer, the density of motor particles increased with time in the area of highest monomer concentration.[5]

1.8 The Use of Organometallics as Power Sources

Organometallics has been an area of study in chemistry for the better part of a century. They span uses in materials, drugs, and most importantly catalysis.[27-29] Many organometallic catalysts have been synthesized and tuned to accomplish a variety of reactions. These reactions span small molecule synthesis, fuel conversion, and polymer synthesis.[30-32] What makes them useful in the view of creating nanomotors is their ability to rapidly convert reactants to products on one centralized location. Furthermore, there has been a long history of fabricating these

catalysts onto surfaces. This wealth of knowledge makes using them in nanomotors highly advantageous.

1.9 References

1. Purcell, E. M. *Am. J. Phys.* **1977**, *45*, 9.
2. Anderson, J. L. *Ann. N. Y. Acad. Sci.* **1986**, *469*, 166.
3. Staffeld, P. O.; Quinn, J. A. *J. Colloid Interface Sci.* **1989**, *130*, 88.
4. Córdova-Figueroa, U. M.; Brady, J. F. *Phys. Rev. Lett.* **2008**, *100*, 158303.
5. Pavlick, R. A.; Sengupta, S.; McFadden, T.; Zhang, H.; Sen, A. *Angew. Chem., Int. Ed.* **2011**, *50*, 9374.
6. Golestanian, R. *Phys. Rev. Lett.* **2009**, *102*, 188305.
7. Howse, J. R.; Jones, R. A. L.; Ryan, A. J.; Gough, T.; Vafabakhsh, R.; Golestanian, R. *Phys. Rev. Lett.* **2007**, *99*, 048102.
8. Ke, H.; Ye, S.; Carroll, R. L.; Showalter, K. *J. Phys. Chem. A* **2010**, *114*, 5462.
9. Ibele, M.; Mallouk, T. E.; Sen, A. *Angew. Chem. Int. Ed.* **2009**, *48*, 3308.
10. Muddana, H. S.; Sengupta, S.; Mallouk, T. E.; Sen, A.; Butler, P. J. *J. Am. Chem. Soc.* **2010**, *132*, 2110.
11. Ibele, M.; Mallouk, T.E.; Sen, A. *Angew. Chem. Int. Ed.* **2009**, *48*, 3308.
12. Kagan, D.; Balasubramanian, S.; Wang, J. *Angew. Chem. Int. Ed.* **2011**, *50*, 503.
13. Yadav, V.; Zhang, H.; Pavlick, R.A.; Sen, A. *J. Am. Chem. Soc.* **2012**, *134*, 15688.
14. Sen, A.; Ibele, M.; Hong, Y.; Velegol, D. *Faraday Discuss.* **2009**, *143*, 15.
15. Liu, R.; Sen, A. *J. Am. Chem. Soc.* **2011**.
16. Suwa, M.; Watarai, H. *Anal. Chim. Acta* **2011**, *690*, 137.
17. Brochard, F. *Langmuir* **1989**, *5*, 432.
18. Eli, R. *J. Colloid Interface Sci.* **1981**, *83*, 77.
19. Nagai, K.; Sumino, Y.; Yoshikawa, K. *Colloids and Surfaces B: Biointerfaces* **2007**, *56*, 197.
20. Abid, J.-P.; Frigoli, M.; Pansu, R.; Szeftel, J.; Zyss, J.; Larpent, C.; Brasselet, S. *Langmuir* **2011**, *27*, 7967.
21. Ismagilov, R. F.; Schwartz, A.; Bowden, N.; Whitesides, G. M. *Angew. Chem., Int. Ed.* **2002**, *41*, 652.
22. Mei, Y.; Solovev, A. A.; Sanchez, S.; Schmidt, O. G. *Chem. Soc. Rev.* **2011**, *40*, 2109.
23. Gao, W.; Sattayasamitsathit, S.; Orozco, J.; Wang, J. *J. Am. Chem. Soc.* **2011**, *133*, 11862.
24. Balasubramanian, S.; Kagan, D.; Jack Hu, C.-M.; Campuzano, S.; Lobo-Castañon, M. J.; Lim, N.; Kang, D. Y.; Zimmerman, M.; Zhang, L.; Wang, J. *Angew. Chem., Int. Ed.* **2011**, *50*, 4161.
25. H.C. Berg, D.A. Brown, *Nature.* **1972**, *239*, 500-504.

26. Hong, Y.; Blackman, N.M.K.; Kopp, N.D.; Sen, A.; Velegol, D. *Phys. Rev. Lett*. **2007**, *99*, 178103 (1-4).
27. Wei, D. *Int. J. Mol. Sci.* **2010**, *11*, 1103.
28. Gasser, G.; Metzler-Nolte, N. *Current Opinion in Chemical Biology*. **2012**, *16*(1-2), 84.
29. Steinborn, D. Fundamentals of Organometallic Catalysis. 1st Edition, **2011**.
30. Koskinen, A.M.P. Asymetric Synthesis of Natural Products. 2nd Edition, **2012**.
31. Matsumoto, T.; Kim, K.; Nakai, H.; Hibino T.; Ogo, S. *Chem.Cat. Chem.* **2013**, *5*, DOI: 10.1002/cctc.201200595.
32. Grubbs, R.H.; Tumas, W. *Science*. **1989**, 242, 907.

Chapter 2

Polymerization Powered Motor

2.1 Introduction

The increased research and potential applications of motors in the delivery of materials, self-assembly, and roving sensors has led to the search for new catalytic sources to expand the range of applications of motor systems. [1-5] The motors described thus far involve the catalytic conversion of small molecules that typically results in a gradient of charged or neutral species that drives the motor. *Listeria* has been observed to move by actin polymerization implicating polymerization powered motion in biological systems.[6,7] However, there have been no reports of motion at the nano and micron scale driven by polymerization reaction. Given the large catalog of known organometallic polymerization catalysts, the design of polymerization driven motors would considerably increase the scope of catalytic reaction that could be employed to power autonomous motion. In addition, polymerization reactions offer the unique opportunity to both power motion and, simultaneously, allow the deposition of polymer along the motion track.[8] Generating motion by polymerization has been previously suggested, although not demonstrated.[9]In this chapter, the first motor to be powered by a polymerization reaction outside biological systems is reported. The motor is powered by ring-opening metathesis polymerization (ROMP) of norbornene. These motors show increased diffusion of up to 70% when placed in solutions of the monomer. Further, the motors were observed to display the phenomenon of chemotaxis when placed in a monomer gradient; an extremely rare example outside biology.[10]

2.2 Synthesis

We chose to employ a form of Grubbs‘ ROMP catalyst [11] for our initial study because of its relatively high stability and high polymerization activity with norbornene (Figure 2-1). The motors were fashioned by first synthesizing gold-silica Janus particles using 0.96 μm silica particles. These particles were deposited as thin films using a published method.[12] Gold was then deposited onto the monolayers creating the asymmetric Janus particles. The particles were then chemically modified with the Grubbs‘ catalyst on the silica side utilizing previously published methods (Figure 2-3).[13]

Silica-Gold Janus Particles where made by placing a glass slide at the bottom of a petri dish and deionized water was added to completely submerge the slide. A layer of hexanes was added on top of the water. To this interface a concentrated solution of silica particles in ethanol was added. The slide was slowly pulled through the interface and allowed to dry to form a monolayer of particles on the slide. Then 7 nm of chromium and 56 nm of gold were evaporated on to the monolayer of particles. The particles were then freed from the slide via sonication to yield the gold silica Janus microspheres (Figure 2-2).

The synthesis of the motor particles was made by first making a linker to attach the catalyst to the particle surface. The linker was synthesized by mixing 3-(chloro)propyl trimethoxy silane (1 equiv.) with 1-methyl imidazole (1 equiv.) at 60°C for 6 d under nitrogen. ^{1}H NMR ($CDCl_3$, 300MHz, ppm): 0.53 (t, 2H J = 8.0Hz), 1.91 (m, 2H J = 7.5Hz), 3.22 (s, 9H), 3.79 (s, 3H), 4.23 (t, 2H J = 7.1Hz), 7.37 (s, 1H), 7.67 (s, 1H), 10.51 (s, 1H). The linker was then

attached to the Janus particles by adding the particles to a 3 mM solution of linker in dichloromethane and stirring overnight in a sealed vial under nitrogen. The particles were centrifuged and washed three times with dichloromethane (DCM). The particles were then dried for several hours in a vacuum oven. To attach Grubbs' catalyst, the particles were suspended in tetrahydrofuran (THF) and then stirred for 1 h with potassium tert-butoxide (K^tOBu 1 equiv.). The particles were centrifuged and washed several times with THF to remove any excess base. Then the particles were added to a 3 mM solution Grubbs' 1^{st} generation catalyst in THF under nitrogen and stirred overnight. The particles were centrifuged and washed five times with DCM under nitrogen (Figure 2-3). The same procedure was followed for coating non-Janus silica spheres (uniform particles).

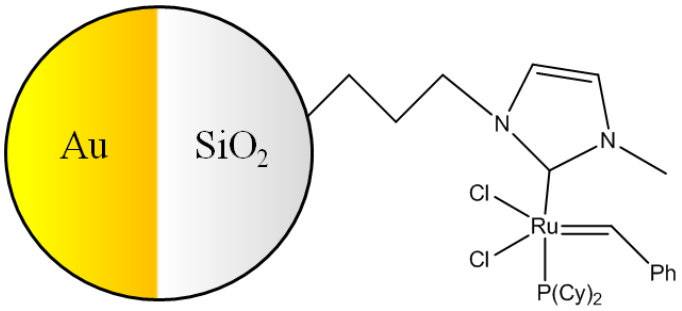

Figure 2-1: Structure of the bound Grubbs catalyst as attached to the silica side of a 0.96 μm Au-Silica Janus microsphere.

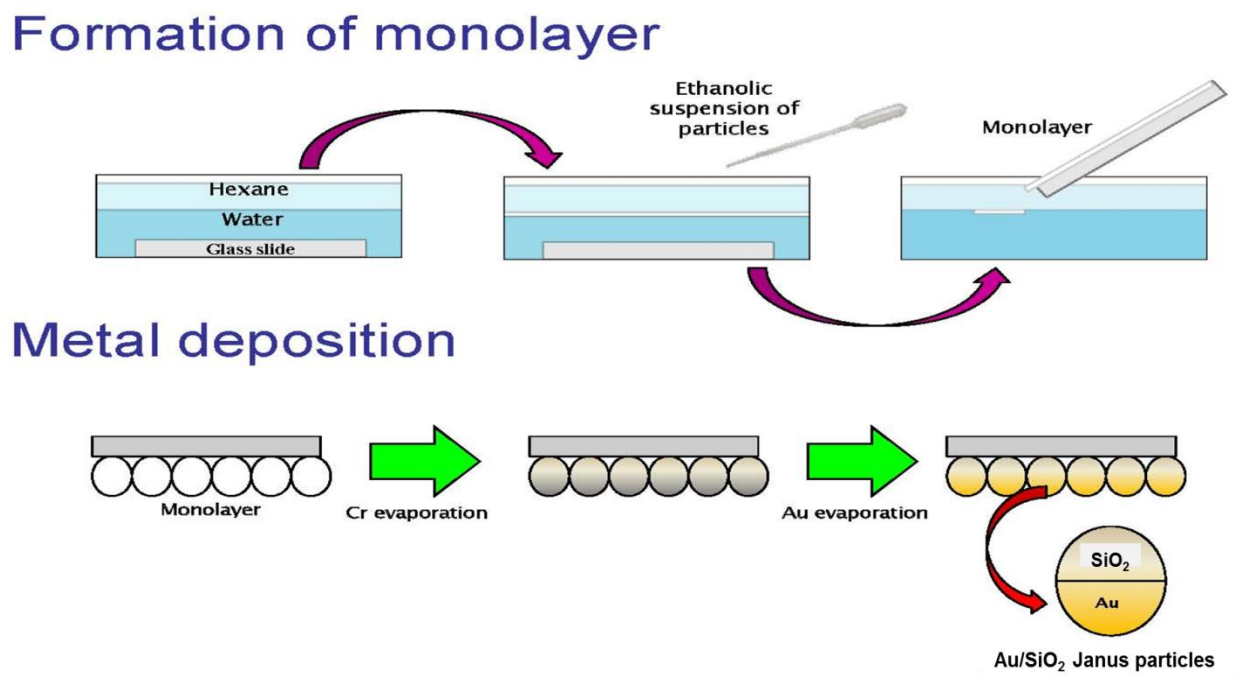

Figure 2-2: Schematic for monolayer synthesis and evaporation of metals to form Janus Particles

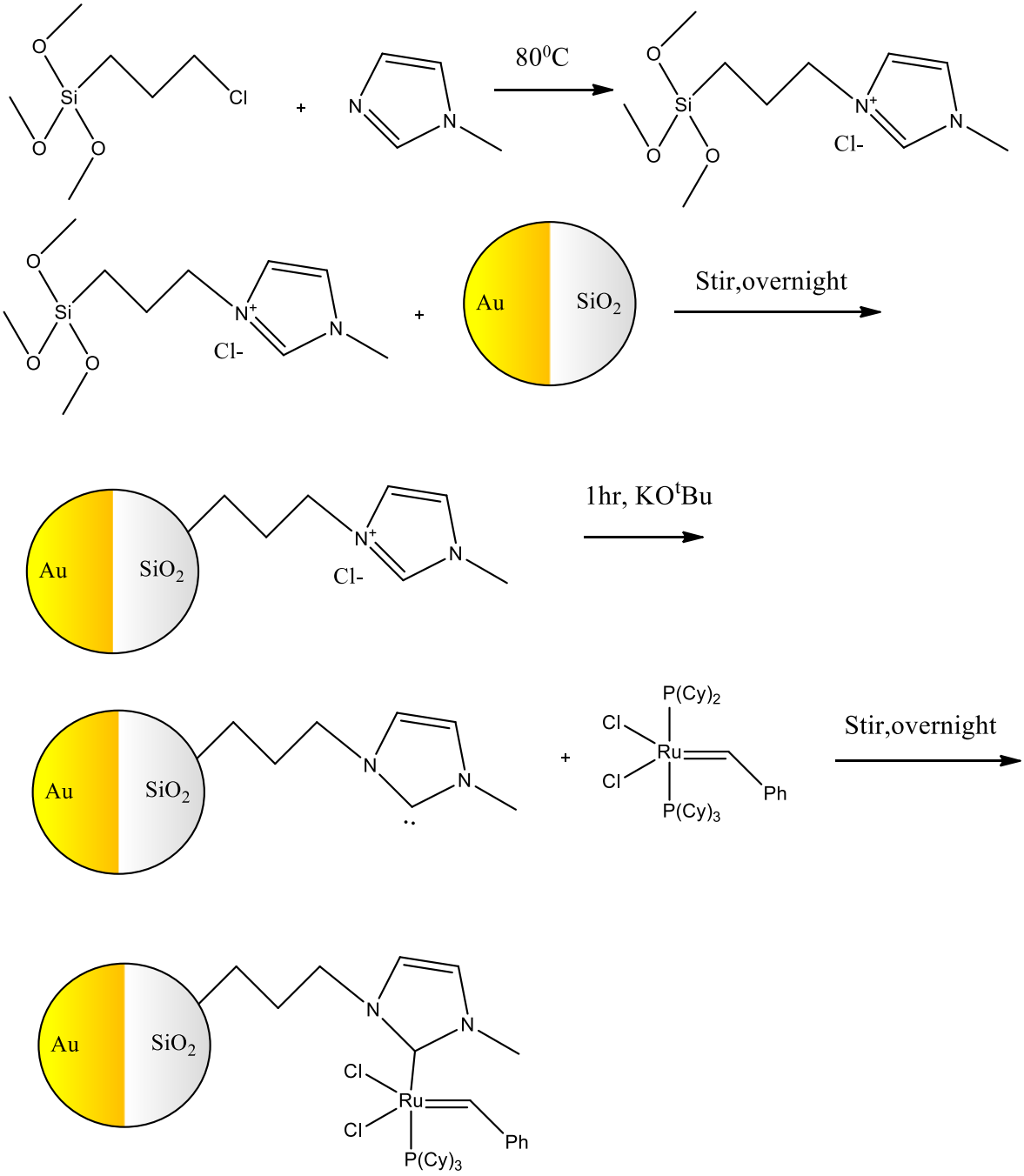

Figure 2-3: Reaction scheme for the attachment of Grubbs' catalyst to the gold-silica Janus microspheres.

2.3 Characterization

2.3.1 XPS Analysis of the Motors

To show that the catalyst was indeed attached to the particles, X-ray Photoelectron Spectroscopy (XPS) was performed to take advantage of the technique's high surface selectivity. The spectrum showed clear peaks for ruthenium, nitrogen, carbon, silicon, oxygen, and gold. The only missing element is phosphorous. Since analysis was performed after the particles were used for polymerization, the phosphine ligand was expected to dissociate off the metal. The XPS binding energies were Ru $3d^{5/2}$: 280 eV; N 1s: 401 eV; Cl $2p^{3/2}$: 198e V; C 1s: 285 eV; O 1s: 532 eV; Si 2s: 154 eV; Au $d^{5/2}$: 334 eV

2.3.2 Activity Assay

To determine the turnover frequency (TOF), a suspension of ~100 mg of particles in 0.01, 0.1, 0.5, and 1 M norbornene in DCM spiked with 0.5 mM chlorobenzene as the internal standard was made and stirred for 6 h. The reaction was monitored using gas chromatography by looking at the ratio of the norbornene peak to the standard and relating that to a calibration curve to determine the moles of monomer consumed. The TOF was shown to be proportional to concentration and begins to saturate at 1 M norbornene (Figure 2-4). Nuclear Magnetic Resonance Spectroscopy (NMR) and Gel Permeation Chromatography (GPC) analysis were performed on the polymer product. The NMR showed all the key peaks except for a water impurity from the $CDCl_3$ (Figure S3). ^{1}H NMR ($CDCl_3$, 300MHz, ppm): 1.33 (m), 1.38 (s), 1.82 (s), 1.86 (m), 1.93 (s, trans), 2.45 (s, cis), 5.24 (s, cis), 5.37 (s, trans) (Figure 2-5). The GPC indicated the formation of polymer with molecular weight 27,000-34,000 (PDI 1.5-1.7) relative to polystyrene standards. This is equivalent to the incorporation of approx. 300 monomer units.

If each monomer is about 0.6 nm (3 C-C bonds at 0.15 nm and 1 C=C bond at 0.13 nm), then the largest possible increase in radius is 0.18 μm (assuming the polymer chains are fully extended from the particle surface) which is about 20% of the starting radius.

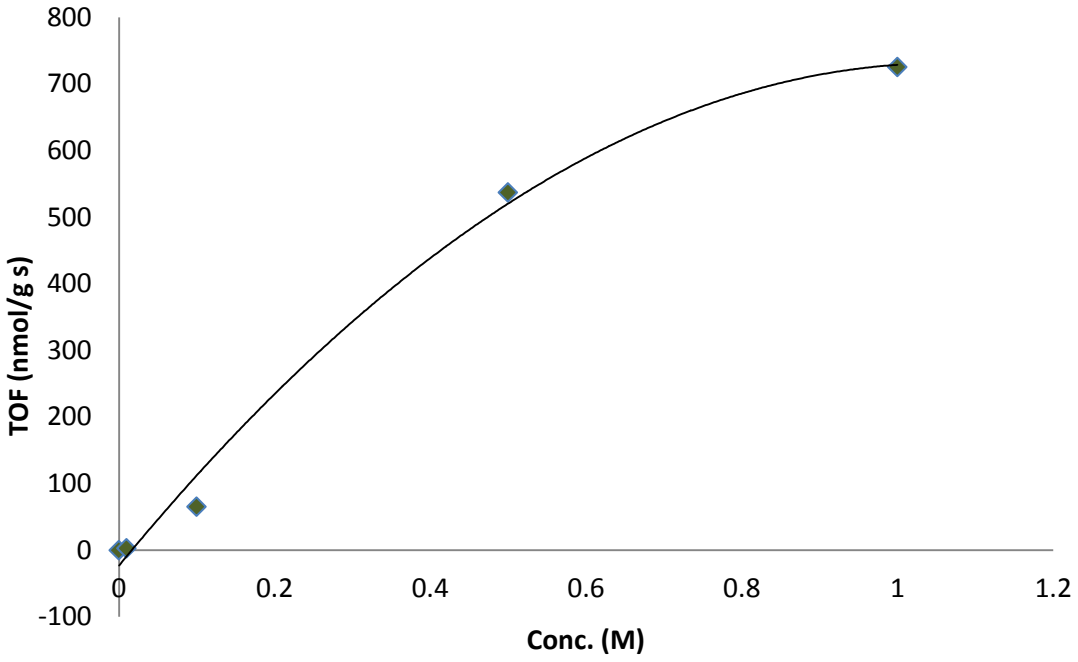

Figure 2-4: The calculated turnover frequency (TOF) in nmol/g s for 0.01, 0.1, 0.5, and 1 M norbornene solutions in dichloromethane versus concentration. The plot begins to level off as the momomer concentration approaches 1 M.

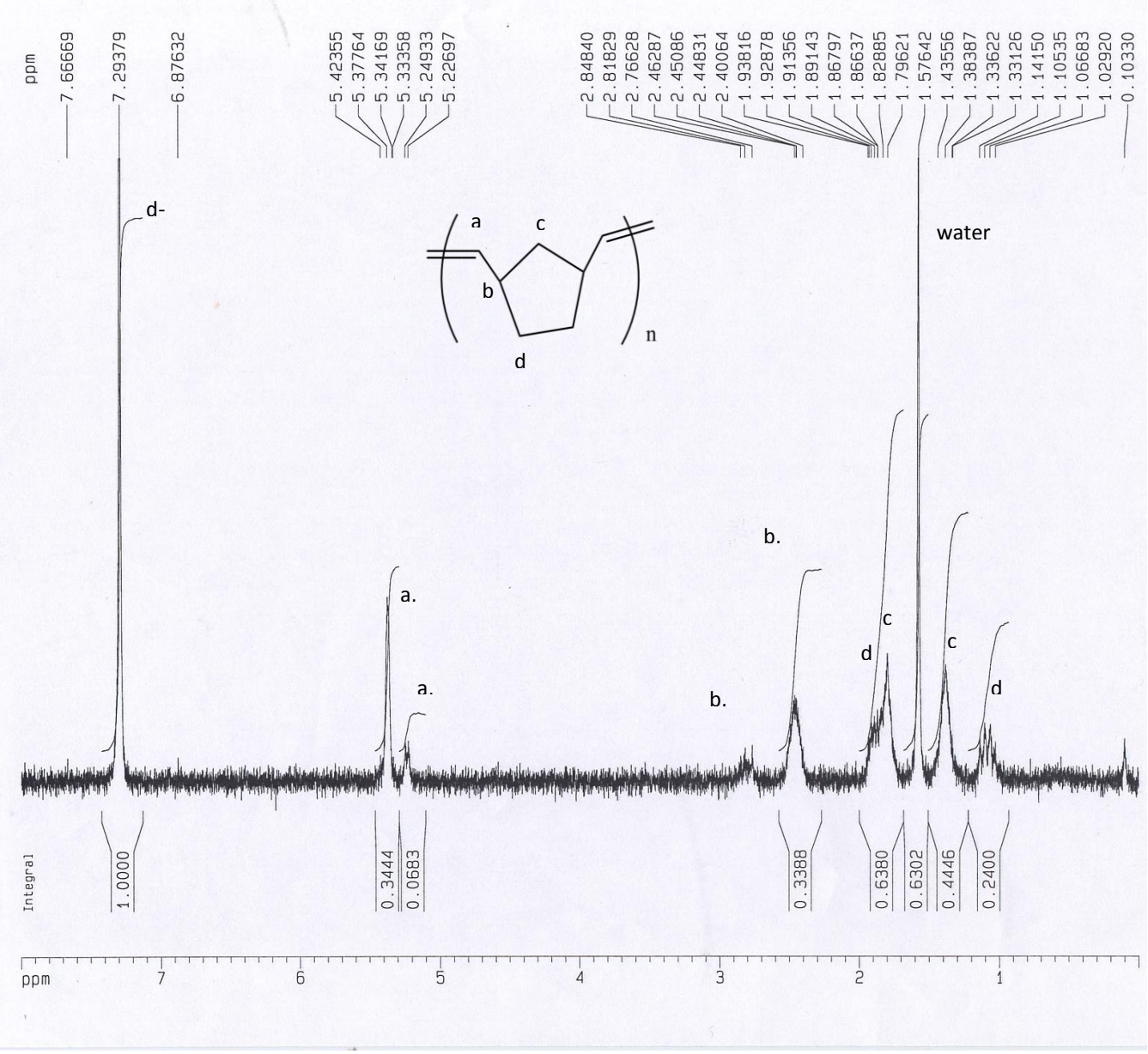

Figure 2-5: NMR spectrum in $CDCl_3$ of polynorbornene produced by the polymerization motors.

2.3.3 SEM

SEM images of these particles before and after exposure to a monomer solution shows the formation of polymer at the particle surface (Figure 2-6). The size increase of the particles due to polymer formation is not significant under the experimental conditions. Further, this increase would decrease the diffusion coefficient and not increase it as is experimentally observed.

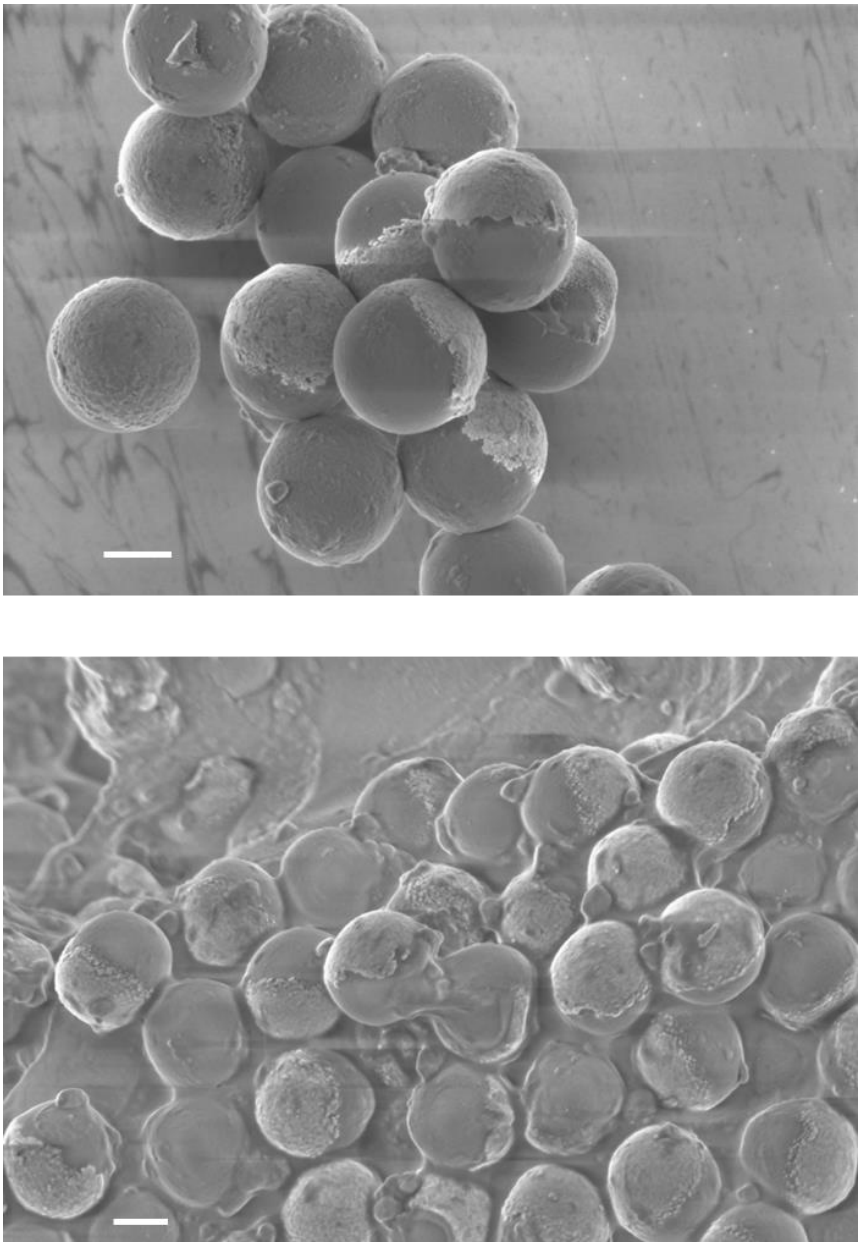

Figure 2-6: Scale bar = 400nm (A) SEM image of as synthesized Au-Silica Janus motor particles. (B) SEM image of motor particles after exposure to a monomer solution showing clear polymer deposition on the motor surface. This is most prevalent on the silica side where the catalyst is bound.

2.4 Calculation of Diffusion Coefficient

The motors (Janus particles and uniform particles) were observed using optical microscopy in varying concentrations of monomer in 1,1,1-trichloroethane to study their motion. Note that the formed polymer is freely soluble in this solvent. The particles were tracked over a 10 sec period using PhysVis. The diffusion coefficients were extrapolated from the tracking data on ~80 particles by processing with MatLab to generate mean squared displacement (MSD) plots and calculating the slope. Changes in viscosity with different monomer concentrations were taken into account when the diffusion coefficients were computed. This was accomplished by normalizing the diffusion coefficients so that the viscosity at each concentration was taken to be the same as that of the pure solvent (Table 2-1).

Diffusion coefficients were calculated by observing suspensions of motors in varying concentrations of norbornene in 1,1,1-trichloroethane using optical microscopy. The solutions were placed in a spacer on a glass slide. Particle movement was observed under a microscope and 30 sec videos were taken in different areas of the observation volume. The particles were then tracked by hand as a function of time using PhyVis to determine the spatial coordinates. Points were taken every 0.5 sec for a period of 10 sec for ~80 particles (~40 particles for the uniformly coated particles). This was done for norbornene concentrations of 0.01, 0.1, 0.5, and 1 M. Controls were also performed by tracking the particles in pure 1,1,1-trichloroethane and tracking particles after being exposed to an inhibitor (ethyl vinyl ether (inhib.)). The data was then evaluated using a Matlab program which calculated the mean squared displacement for each particle using different time steps and then averaging them together (Table 2-2). The mean square displacement (MSD) was then plotted against the time step and the diffusion coefficient

was calculated from the slope of the line. These values were then adjusted by taking into account the change in viscosity, which tend to increase with increasing norbornene concentration (Table 2-1). The velocities were calculated using the equation,

$$D^* = \frac{U^2}{D_r} \qquad (2\text{-}1)$$

where D* is the enhanced diffusion coefficient, U is the velocity, and D_r is the rotational diffusion coefficient (0.19 s^{-1}) (Table 2-3).[14]

Table 2-1: The diffusion coefficients of Janus motors normalized for change in viscosity of the medium.

Sample	Diffusion Coefficient ($\mu m^2/s$)	S.D.	Viscosity (Pa sec)	Corrected Diffusion Coefficient ($\mu m^2/s$)	Corrected S.D.
0 M	0.29	0.025	7.00E-04	0.29	0.025
0.01 M	0.35	0.03	7.17E-04	0.36	0.031
0.1 M	0.37	0.027	7.56E-04	0.39	0.029
0.5 M	0.40	0.025	8.02E-04	0.46	0.029
1 M	0.38	0.03	9.08E-04	0.49	0.039
0.1 M (Inhibitor)	0.29	0.026	7.56E-04	0.31	0.028
0.5 M (Inhibitor)	0.30	0.055	8.02E-04	0.34	0.063

Table 2-2: Mean squared displacements for each time step of Janus motors.

Time Step	0M	0.01M	0.1M	0.5M	1M	0.1M (Inibitor)	0.5M (Inhibitor)
0.5	0.58	0.70	0.74	0.80	0.76	0.58	0.60
1.0	1.16	1.40	1.48	1.60	1.52	1.16	1.20
1.5	1.74	2.10	2.22	2.40	2.28	1.74	1.80
2.0	2.32	2.80	2.96	3.20	3.04	2.32	2.40
2.5	2.90	3.50	3.70	4.00	3.80	2.90	3.00
3.0	3.48	4.20	4.44	4.80	4.56	3.48	3.60
3.5	4.06	4.90	5.18	5.60	5.32	4.06	4.20
4.0	4.64	5.60	5.92	6.40	6.08	4.64	4.80
4.5	5.22	6.30	6.66	7.20	6.84	5.22	5.40
5.0	5.80	7.00	7.40	8.00	7.60	5.80	6.00
5.5	6.38	7.70	8.14	8.80	8.36	6.38	6.60
6.0	6.96	8.40	8.88	9.60	9.12	6.96	7.20
6.5	7.54	9.10	9.62	10.40	9.88	7.54	7.80
7.0	8.12	9.80	10.36	11.20	10.64	8.12	8.40
7.5	8.70	10.50	11.10	12.00	11.40	8.70	9.00
8.0	9.28	11.20	11.84	12.80	12.16	9.28	9.60
8.5	9.86	11.90	12.58	13.60	12.92	9.86	10.20
9.0	10.44	12.60	13.32	14.40	13.68	10.44	10.80
9.5	11.02	13.30	14.06	15.20	14.44	11.02	11.40
10.0	11.60	14.00	14.80	16.00	15.20	11.60	12.00

Table 2-3: Calculated velocities at varying monomer concentrations for Janus Motors.

Sample	Diffusion Coefficient ($\mu m^2/s$)	Velocity ($\mu m/s$)
0 M	0.29	0.24
0.01 M	0.36	0.26
0.1 M	0.39	0.28
0.5 M	0.46	0.30
1 M	0.49	0.31
0.1 M (Inhibitor)	0.31	0.25
0.5 M (Inhibitor)	0.34	0.26

The calculated diffusion coefficients of the Janus motors increased from 0.29 $\mu m^2/s$ to 0.49 $\mu m^2/s$ going from 0 to 1 M norbornene concentration (Figure 2-7). This translates to a 70% overall increase in mobility. As a control, diffusion of the motor was observed after treatment with an inhibitor, ethyl vinyl ether. The increase in diffusion is significantly reduced to 18% when the motors were treated with an inhibitor. This clearly demonstrated that the increase in diffusion stems from substrate turnover. The velocity of the particles also increased from 0.24 μm/s to 0.31 μm/s as the substrate turnover was increased by the addition of fuel (Table 2-3). Experiments were also done on silica microspheres uniformly coated in Grubbs‘ catalyst (uniform motors) in 0.1M and 0.5M norbornene solution. For these motors the diffusion increase was only 40% compared to 60% for the Janus motor particles in a 0.5 M solution (Table 2-4). Note that the gold segment is missing in these particles. Thus, the asymmetry of the Janus

particle causes an increase in directionality leading to the higher overall increase in diffusion. Further, a plot of the diffusion coefficient versus the natural logarithm of turnover frequency (TOF) revealed a linear relationship between the two with the intercept through the expected diffusion coefficient of the motor without fuel (Figure 2-7). The reason for the observed precise relationship remains unclear. Temporal tracks of the particles reveal that in the presence of monomer the motors exhibit longer linear trajectories and have greater displacements (Figure 2-8).

Table 2-4. Diffusion coefficients for uniformly coated silica particles (uniform motors)

	Diffusion Coefficient ($\mu m^2/s$)	Standard Deviation	Viscosity (Pa sec)	Corrected Diffusion Coefficient ($\mu m^2/s$)	Corrected Standard Deviation
0 M	0.28	0.01	7.00E-04	0.28	0.01
0.1 M	0.36	0.01	7.56E-04	0.39	0.01
0.5 M	0.34	0.01	8.02E-04	0.39	0.01
0.1M (inhib.)	0.30	0.02	7.56E-04	0.32	0.02
0.5 M (inhib.)	0.25	0.02	8.02E-04	0.29	0.02

A

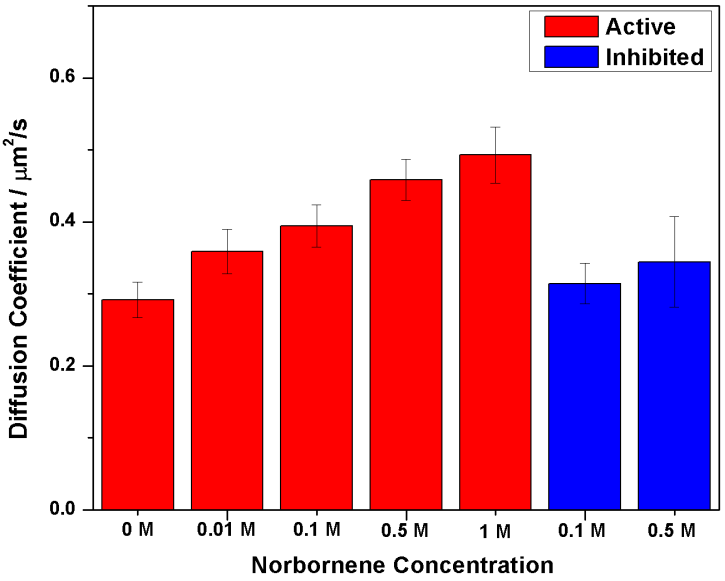

B

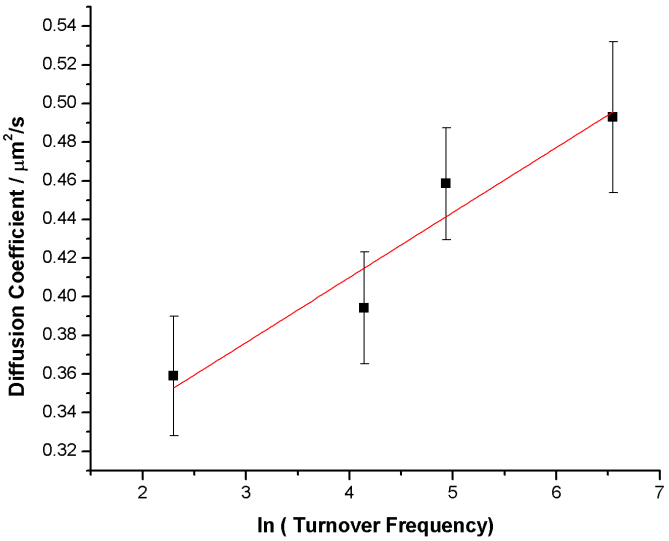

Figure 2-7: (A) Calculated diffusion coefficients of the Janus Motors at varying monomer concentrations**.** The diffusion coefficients exhibit a steady increase over the monomer concentrations (red). After treatment with an inhibitor there was a significant decrease in the diffusion coefficient (blue) showing that the enhanced diffusion was a result of substrate turnover. (B) Plot of the diffusion coefficient versus the natural logarithm of turnover frequency

at the same monomer concentration. This shows a linear relationship between the two parameters with the intercept through the expected diffusion coefficient without fuel.

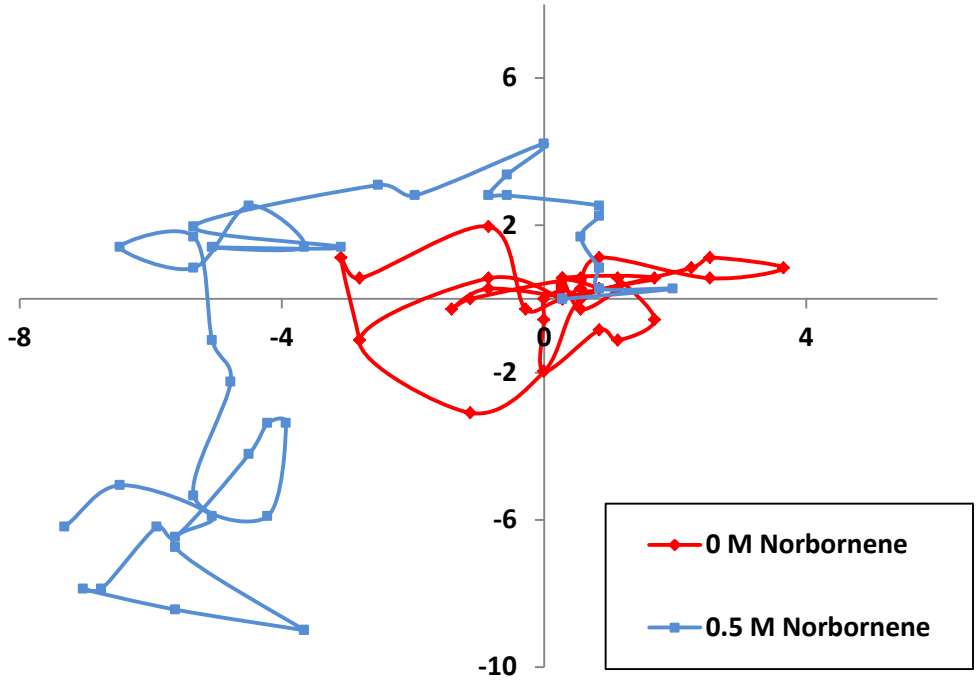

Figure 2-8. Temporal particle tracks of the Janus motor with no fuel (red) and in 0.5 M norbornene (blue). Each point represents a displacement in μm over 0.5 sec, beginning from the origin over a 20 sec time span. The motor particles in the fuel show longer displacements in a single direction.

2.5 Evaluation of the Mechanism of Motility

2.5.1 Osmophoresis

The observed substrate concentration-dependent increase in motor diffusion can be ascribed to osmophoresis.[15-20] Theoretical calculations suggest that an asymmetric catalyst that consumes substrate on one side of the particle and releases either a lower concentration of products and/or a more slowly diffusing product, creates an osmotic force across the particle. This force causes net fluid flow from the side with lower substrate concentration (the catalytic side) to the side with higher substrate concentration (the non-catalytic side). The particle will then move in the direction opposite to the fluid flow (Figure 2-9). In the present case, the asymmetrically placed Grubbs catalyst consumes many monomer molecules while forming only a few polymer chains. This allows the motor to set up the necessary monomer gradient.

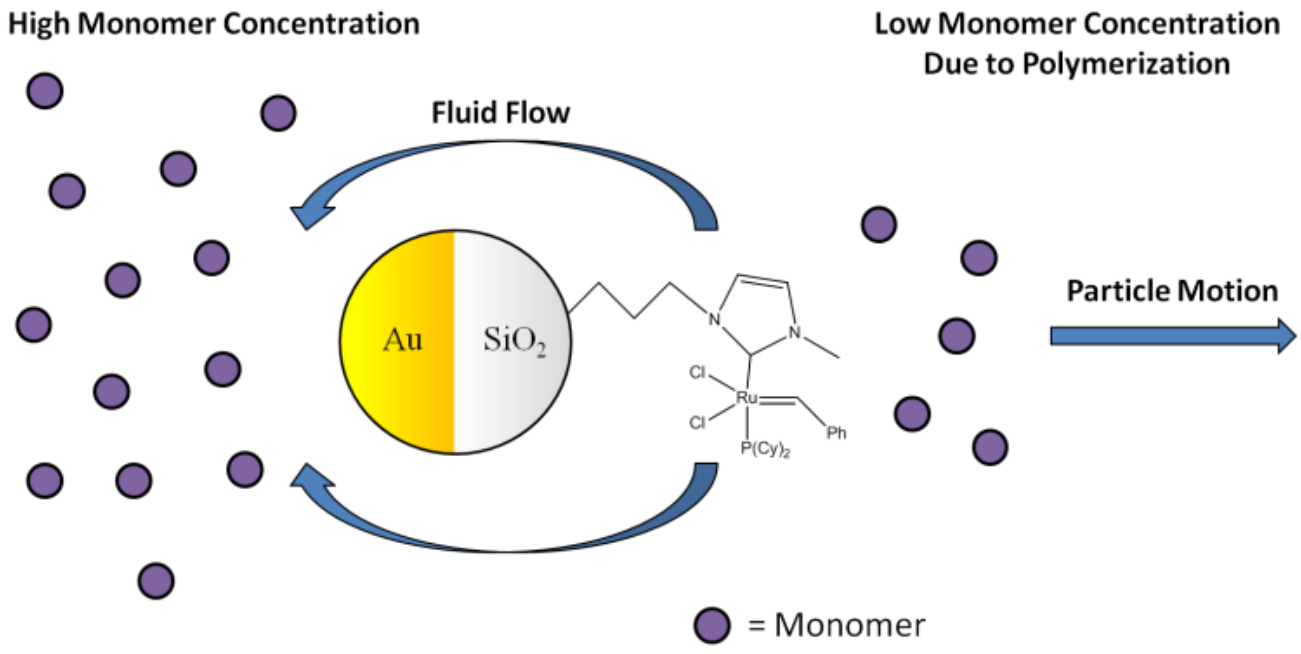

Figure 2-9: The Janus motor consumes monomers at the silica face creating an area of low monomer concentration. Fluid in the low concentration region flows towards the higher concentration region at the gold face. Consequently the motor moves in the opposite direction.

2.5.2 Thermal Effect

Another possible mechanism is a thermal effect. This effect occurs if the reaction is producing enough heat locally to cause an enhancement in the diffusion coefficient. However, our calculations show that, at the highest TOF, the temperature change would only be 1.8 μK, which is too small to account for the observed enhancement. The local rise in temperature in 1 sec was estimated for the motor. The heat liberated (q) by one motor was found using the equation,

$$q = \frac{k\Delta H}{N_a} \tag{2-2}$$

where, k is the turnover number (1.24 x 10^7 s^{-1}) for an individual particle at 1 M norbornene, ΔH is the enthalpy change in the reaction (-56,000 J mol^{-1})[21], and N_a is Avogadro's number (6.023 x 10^{23} molecules mol^{-1}). The heat transfer (q) to the surrounding solvent is

$$q = 4\pi\kappa R\Delta T \tag{2-3}$$

where κ is thermal conductivity of 1,1,1- trichloroethane (0.101 W m^{-1} K^{-1}), R is the radius of the particle (0.48 x 10^{-6} m), and ΔT is change in temperature in Kelvin. Using equations 2 and 3, we calculate ΔT to be 1.8 x 10^{-6} K.

Also, if the enhanced diffusion was due to changes in temperature, the observed diffusion would be *directly* related to the turnover frequency. Since,

$$D = \frac{kT}{6\pi\eta a} \quad (2\text{-}4)$$

where D is the diffusion coefficient, k is the Boltzmann constant, T is temperature, η is viscosity, and a is the particle radius, and the amount of heat released is directly related to the turnover frequency. Therefore,

$$D \propto TOF \quad (2\text{-}5)$$

However, as shown in Figure 2-7, the diffusion coefficient increase is proportional to the natural log of the TOF.

2.6 Chemotaxis

One of the defining features of living systems is their ability to sense and move up a fuel/food concentration gradient.[22] This phenomenon has very rarely been observed outside biology but can form the basis for the design of intelligent sensors that respond to information in the form of gradients. We tested our polymerization motors for their ability to chemotax up a norbornene concentration gradient.

To determine if the particles move up a monomer gradient, a gel of octadecyl acrylate crosslinked with ethylene glycol dimethacrylate was soaked in either a 1 M norbornene solution or a 1 M norbornane solution overnight. The gel (with either norbornene or norbornane as a control) was then placed on a glass slide and then a suspension of motor particles was added. The particles were observed over a 4 h period near the gel edge after an initial settling period of 0.5 h. As another control a solution of unfunctionalized gold-silica Janus microspheres was also observed in the presence of a norbornene-soaked gel. Particle densities were normalized so that the initial density was set to 1. Multiple runs were then averaged together (Table 2-5). Statistical analysis was run and p values are reported in Table 2-6.

To perform the chemotaxis experiments a crosslinked acrylate gel containing 1 M norbornene was placed in a solution containing the motor particles. The number of particles at the gel edge was observed over a 4 h period after an initial settling period of 0.5 h. The first observation was taken to be at 0 h. The particle densities were normalized by dividing the number of particles at each time period by the number of particles at 0 hours, so that the initial density was taken to be 1 (Table 2-5). Several runs were averaged together to produce the graph shown in Figure 2-10. On average, the motor particles increased in concentration at the gel edge with time. After the first hour, the rate of agglomeration began to plateau. This is to be expected since the concentration gradient of the monomer leaching from the gel is steepest at short times and should begin to level off over longer time spans in accordance with Fick's second law.

To rule out a non-electrolyte diffusiophoretic mechanism for the observed chemotactic behavior, several controls were run. Non-electrolyte diffusiophoresis is a mechanism by which

particles move in response to a gradient of an uncharged solute. The velocity is given by equation 6,

$$U = KL\frac{kT}{\eta}\nabla C \tag{2-6}$$

where U is the velocity of the particle, K is the Gibbs absorption length, L is the length of the particle-solute interaction, k is the Boltzmann constant, T is temperature, η is viscosity, and C is the solute concentration.[23] If such a mechanism was operating, non-catalytic particles should behave similarly in the presence of the monomer gradient. Accordingly, a control was run with unfunctionalized gold-silica Janus particles in the presence of a norbornene-soaked gel. These particles, on average, did not show increased agglomeration at the gel. Another control was run with catalytic motor particles using a norbornane-soaked gel (unlike norbornene, norbornane lacks vinyl functionality and is unreactive). Again, there was no appreciable increase in particle density at the gel over a 4 h period. Therefore it is unlikely that a diffusiophoretic mechanism is behind the observed agglomeration. The control experiments also serve to rule out other non-catalytic advection mechanisms. It should also be noted the particles at the gel edge are not stuck and continue to undergo Brownian-type motion.

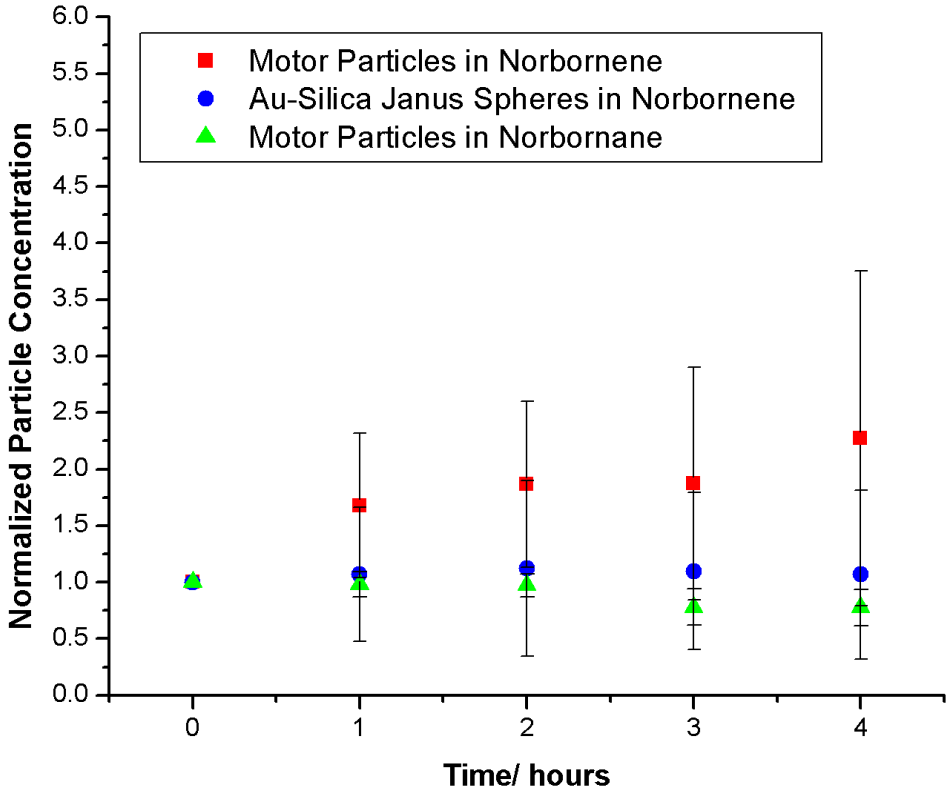

Figure 2-10. Normalized particle population at the gel edge as a function of time. The populations were normalized so that the initial population is taken to be 1. The motor particles in a norbornene gradient (red) exhibit a higher average agglomeration at the gel over both unfunctionalized Au-Silica Janus spheres in norbornene gradient (blue) and motor particles in a norbornane gradient (green).

Table 2-5: Average normalized particle concentrations over the 4 h in chemotaxis experiment.

Time (h)	Motor Particles in Norbornene	S.D.	Au-Silica Janus Spheres in Norbornene	S.D.	Motor Particles in Norbornane	S.D.
0	1.00	0.00	1.00	0.00	1.00	0.00
1	1.68	0.64	1.07	0.59	0.98	0.11
2	1.87	0.73	1.12	0.78	0.97	0.10
3	1.87	1.03	1.10	0.70	0.78	0.16
4	2.27	1.48	1.07	0.75	0.78	0.16

Table 2-6: Statistical analysis of a) motor particles in norbornene versus Au-Silica Janus spheres in norbornene and b) motor particles in norbornene versus motor particles in norbornane

A

Time	Motor Particles in Norbornene	S.D.	Au-Silica Janus Spheres in Norbornene	S.D.	P value
0	1.00	0.00	1.00	0.00	-
1	1.68	0.64	1.07	0.59	0.22
2	1.87	0.73	1.12	0.78	0.23
3	1.87	1.03	1.10	0.70	0.24
4	2.27	1.48	1.07	0.75	0.17

B

Time	Motor Particles in Norbornene	S.D.	Motor Particles in Norbornane	S.D.	P value
0.00	1.00	0.00	1.00	0.00	-
1.00	1.68	0.64	0.98	0.11	0.08
2.00	1.87	0.73	0.97	0.10	0.05
3.00	1.87	1.03	0.78	0.16	0.08
4.00	2.27	1.48	0.78	0.16	0.09

The agglomeration of the motor particles at the gel may arise from an enhanced diffusion mechanism as described by Hong.[9] The substrate concentration increases continuously as the motor travels up the gradient. Thus, the diffusion rate increases on moving up the gradient and decreases on moving down the gradient. A higher diffusion coefficient results in a higher average displacement causing the motor to move, on average, more towards the gel. This mechanism is absent in the two controls because the particle diffusion coefficient remains relatively constant over the range of norbornene/norbornane concentrations. The proposed mechanism is stochastic in nature and describes an *average* trend towards the gel and is different from biological chemotaxis which requires temporal memory of the concentration gradient. The stochastic nature of the motion is consistent with the observed random trajectories of the motors in the gradient. The observed phenomenon is important since it creates a way to direct the motion of these motors.

2.7 Conclusion

In conclusion, a synthetic motor system was designed that exhibits enhanced diffusion by harnessing the energy of a catalytic polymerization reaction. The motor was also found to exhibit the phenomenon of chemtaxis by moving up the monomer gradient. This allows the directed movement of the motor towards specific targets, and should permit the deposition of polymer along the motion track in a solvent in which the polymer is insoluble. Furthermore, the work expands the scope of catalytic reactions that can be utilized to create motion of micron-scale objects.

2.8 References

1. Paxton, W.F. ; Sundararajan, S.; Mallouk, T.E.; Sen, A. *Angew. Chem. Int. Ed.* **2006**, *45*, 5420.
2. Sanchez, S.; Pumera, M. *Chem. Asian. J.* **2009**, *4*, 1402.
3. Wang, J.; Manesh, K. M. *Small.* **2010**, *6*, 338.
4. Mirkovic, T.; Zacharia, N.S.; Scholes, G.D. ; Ozin, G.A. *Small.* **2010**, *6*, 159.
5. Hong, Y.; Velegol, D.; Chaturvedi, N.; Sen, A. *Phys. Chem. Chem. Phys.* **2010**, *12*, 1423.
6. Carlier, M.F.; Wiesner, S.; Clainche, C.L.; Pantaloni, D. *C.R. Biologies*. **2003**, *326*, 161.
7. Watarai, H.; Suwa, M.; Iiguni, Y. *Anal Bioanal Chem.* **2004**, *378***,** 1693.
8. Manesh, K. M.; Balasubramanian, S.; Wang, J. *Chem Commun.* **2010**, *46*, 5704.
9. Godoy, J.; Vives, G.; Tour, J.M. *ACS Nano*. **2011**, *5*, 85.
10. Hong, Y.; Blackman, N.M.K.; Kopp, N.D.; Sen, A.; Velegol, D. *Phys. Rev. Lett*. **2007**, *99*, 178103 (1-4).
11. Vougioukalakis, G. C.; Grubbs, R. H. *Chem. Rev*. **2010**, *110*, 1746.
12. Goldenberg, L.M.; Wagner, J.; Stumpe, J. ; Paulke, B.R.; Gornitz, E. *Langmuir*. **2002**, *18*, 5627.
13. Park, K.H.; Kim, S.; Chung, Y.K. *Bull. Korean Chem. Soc.* **2008**, *29*, 2057.
14. Hong, Y.; Blackman, N.M.K.; Kopp, N.D.; Sen, A.; Velegol, D. *Phys. Rev. Lett*. **2007**, *99*, 178103 (1-4).
15. Golestanian, R.; Liverpool, T.B.; Ajdari, A.*Phys. Rev. Lett.* **2005**, *94*, 220801.
16. Ruckner, G.; Kapral, R. *Phys. Rev. Lett.* **2007**, *98*, 150603.
17. Co´rdova-Figueroa, U. M. ; Brady, J. F. *Phys. Rev. Lett.* **2008**, *100***,** 158303.
18. Ke, H.; Ye, S.; Carroll, R.L.; Showalter, K. *J. Phys. Chem. A.* **2010**, *114*, 5462.
19. Ebbens, S.; Jones, R.A.L.; Ryan, A.J.; Golestanian, R.; Howse, J.R. *Phys. Rev. E.* **2010**, *82*, 015304.
20. Delogu, F. *J. Phys. Chem. C.* **2009**, *113*, 15909.
21. Lebedev, B.; Smirnova, N.; Kiparisova, Y.; Makovetsky, K.*Makromol. Chem.* **1992**, *193*, 1399.
22. Berg, H.C.; Brown, D.A. *Nature.* **1972**, *239*, 500.
23. Anderson, J.L. *Ann. Rev. Fluid Mech.* **1989**, *21*, 61.

Chapter 3

A Catalytically Driven Organometallic Molecular Motor

3.1 Introduction

In biology there are many examples of molecular motor systems, including single enzymes, actin and myosin, and even rotary motors such as ATPase.[1-5] There has also been work in synthetic molecular systems, which include the rotors synthesized by the Feringa group, the nanocar by the Tour group, and the shuttle systems designed by Stoddart, Leigh, and others that move a molecule along a chain.[6-17] These systems are useful as switches, transport devices, and even as sub-nanometer pumps.[6-17] Taking a cue from the biological systems, the ideal way to power motion in nanoscale systems is though small molecule catalysis. Thus, to expand the catalog of nm and sub-nm-scale machines available, it is necessary to investigate catalytically-powered motion that is compatible with such small length scales. In this chapter, a simple sub-nm scale molecular catalyst is shown to experience enhanced motility when performing a catalytic reaction in a manner similar to that observed for larger micromotors.[18-31]

Since molecular systems are difficult to observe via optical microscopy it is necessary to utilize other forms of spectroscopy to study their motion. One such technique is diffusion Nuclear Magnetic Resonance (NMR) spectroscopy. The NMR technique works by applying a pulse field gradient of varying magnitude to the sample to "encode" the molecules. After a set time, a "decoding" pulse field gradient is applied. If the molecule has moved sufficiently there is a decrease in the intensity of the NMR resonances associated with the molecule. This phenomenon is related to the diffusion coefficient through the following equation,[32-34]

$$\ln\left(\frac{I}{I_0}\right) = -D\left(G\delta\gamma\right)^2\left(\Delta - \frac{\delta}{3} - \frac{\tau}{2}\right) \quad (3\text{-}1)$$

where I is the final resonance intensity, I_o is the initial intensity, D is the diffusion coefficient, G is the magnitude of the gradient, γ is the nuclear gyromagnetic ratio, δ is the gradient duration, τ is the gradient relaxation time, and Δ is the time between gradient pulses. Using this method, a proton signal related to the catalyst is monitored as a function of gradient intensity to reveal the diffusion coefficient. The technique only measures the change in diffusivity of an ensemble rather than a single catalyst molecule. For our purpose, we performed diffusion NMR studies to measure the diffusivity of a Grubbs' 2nd generation metathesis catalyst while performing ring closing metathesis (RCM) and cross metathesis (CM) (Figure 3-1).

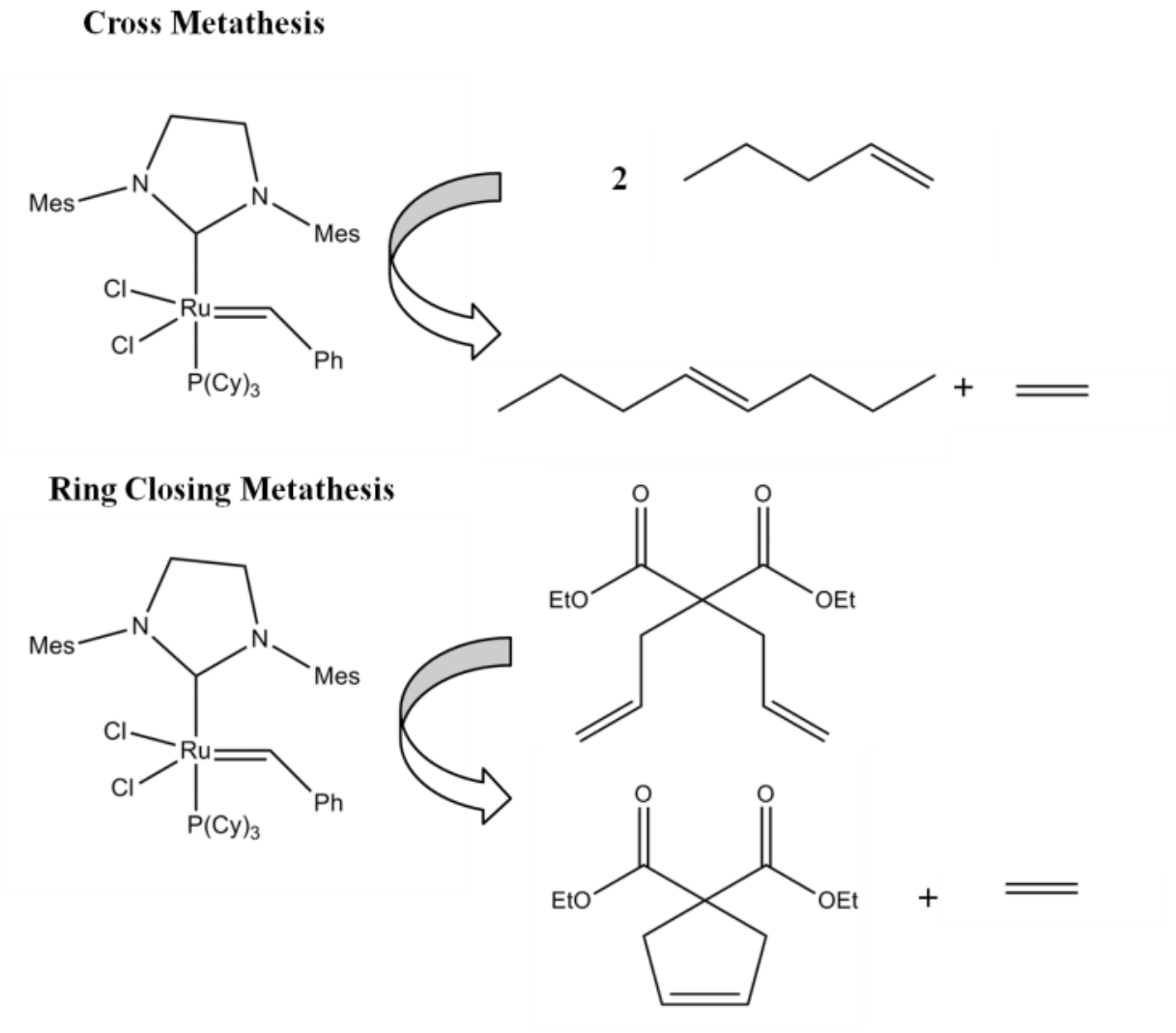

Figure 3-1: Structure of Grubbs' 2nd generation catalyst and reaction scheme for the cross metathesis (CM) of 1-pentene and the ring closing metathesis (RCM) of diethyl diallylmalonate.

3.2 NMR Diffusion Measurements

In a typical RCM experiment, 3 mg (3mM) of Grubbs' 2nd generation catalyst and 0.003 ml to 0.145 ml (0.01M to 0.5M) of diethyl diallylmalonate (DDM) were dissolved in 1.2 ml of

chloroform-d under nitrogen. Then 0.6 ml of the solution was added to the NMR tube. The tube was allowed to vent the generated ethylene gas in order to avoid possible pressure build-up. The NMR sample was allowed to equilibrate in the NMR probe for at least 15 min. The diffusion experiment was then run three times on each sample. To improve the accuracy of the measurements, the spectra were taken of only the singlet around 2.31 ppm, corresponding to the ortho-methyl groups of the mesityl moiety. For the CM of 1-pentene, 0.0035 ml to 0.07 ml (0.05M to 1M) was added to 0.6 ml of the 3mM catalyst solution. For catalyst inhibition, 0.05 ml (20mM) of ethyl vinyl ether was added to the reduced volume (0.6 ml) before NMR analysis. The same protocol was then followed for CM as was for RCM. The extent of reaction occurring during the 15 min equilibration time was <5% for both RCM and CM. To see if the diffusion coefficient returned to that of the base value following completion of the reaction, the RCM and CM reactions were run in an open NMR tube in the glove box for 3 h and then sealed and analyzed by NMR. Each sample was run three times and multiple samples were averaged together and then corrected for changes in viscosity, shown in Table 3-1 and 3-2. To check for possible structural changes on the catalyst during reaction, the phosphorous and hydrogen NMR signals were examined in the presence and absence of the substrate. Finally, computational calculations were performed on the different intermediate structures.

Table 3-1: Average diffusion coefficients, D, of Grubbs' catalyst in the presence of diethyl diallyl malonate (DDM).*

[DDM]	D (x $10^{-9}m^2/s$)	Std. Dev.	Viscosity (cP)	D (x $10^{-9}m^2/s$) corr. for visc.	Std. Dev. corr. for visc.
0M	0.662	0.018	0.400	0.662	0.018
0.01M	0.903	0.049	0.400	0.903	0.049
0.02M	0.770	0.01	0.405	0.768	0.008
0.05M	1.270	0.33	0.39	1.223	0.322
0.1M	1.250	0.203	0.467	1.458	0.237
0.5M	1.193	0.267	0.515	1.536	0.343
0.1M inhib.	0.701	0.026	0.467	0.818	0.030
0.5M inhib.	0.581	0.034	0.515	0.748	0.044
0.1M (completed)	0.672	0.072	0.467	0.784	0.084

*Measured at 295K in 0.6 ml of $CDCl_3$ in a AV-III-850MHz Bruker NMR with a diffusion probe. Catalyst concentration is 3mM and inhibitor concentration is 0.2M.

Table 3-2: Average diffusion coefficients, D, of Grubbs' catalyst measured in the presence of 1-pentene.*

[1-Pentene]	D (x $10^{-9}m^2/s$)	Std. Dev.	Viscosity (cP)	D (x $10^{-9}m^2/s$) corr. for visc.	Std. Dev. corr. for visc.
0M	0.66	0.02	0.33	0.66	0.02
0.05M	0.64	0.01	0.37	0.72	0.02
0.1M	0.86	0.12	0.35	0.91	0.12
0.5M	1.07	0.06	0.26	0.85	0.05
1M	0.81	0.03	0.26	0.64	0.02
0.05M inhib.	0.77	0.02	0.37	0.86	0.02
0.1M inhib.	0.81	0.07	0.35	0.86	0.08
0.5M inhib	0.81	0.02	0.26	0.64	0.02
1M inhib.	0.86	0.01	0.26	0.67	0.01
0.5M completed	0.86	0.04	0.26	0.68	0.03

* Measured at 295K in 0.6 ml of deuterated chloroform in a AV-III-850MHz Bruker NMR with a diffusion probe. Catalyst concentration is 3mM and inhibitor concentration is 0.2M.

The diffusion coefficient of the catalyst ensemble was found to increase for RCM (Table 3-1, Figure 3-2). For CM, the increase in diffusivity was not significant (Table 3-2, Figure 3-3). Since CM also generates ethylene gas at comparable rates, this shows that ethylene production is not the cause of the enhanced diffusion in RCM. Moreover, due to the high solubility of ethylene in the reaction solvent, no gas bubbles were observed visually. For RCM, the highest observed diffusion coefficient was about 2 times that of the base diffusion coefficient. Increased

diffusivity was not observed upon the addition of an inhibitor, ethyl vinyl ether. When the RCM was allowed to go to completion, the observed diffusion coefficient also returned to the base value for the catalyst with no substrate. The observed diffusion coefficient for the Grubbs' catalyst in the absence of substrate correlates well to a hydrodynamic radius of about 6.0Å.

A

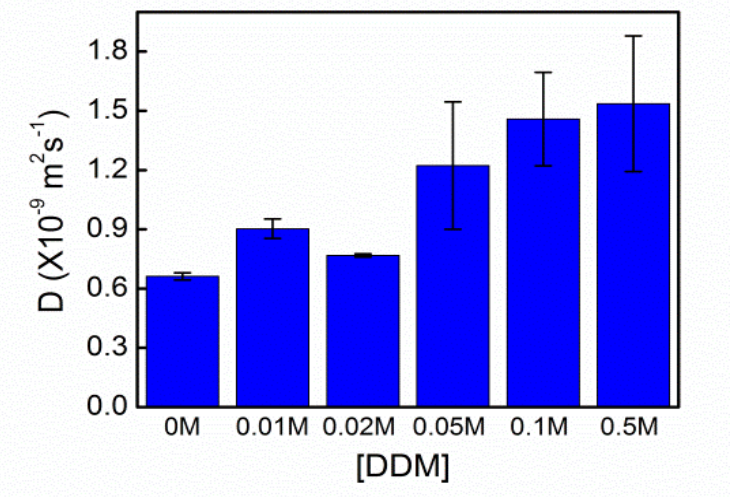

B

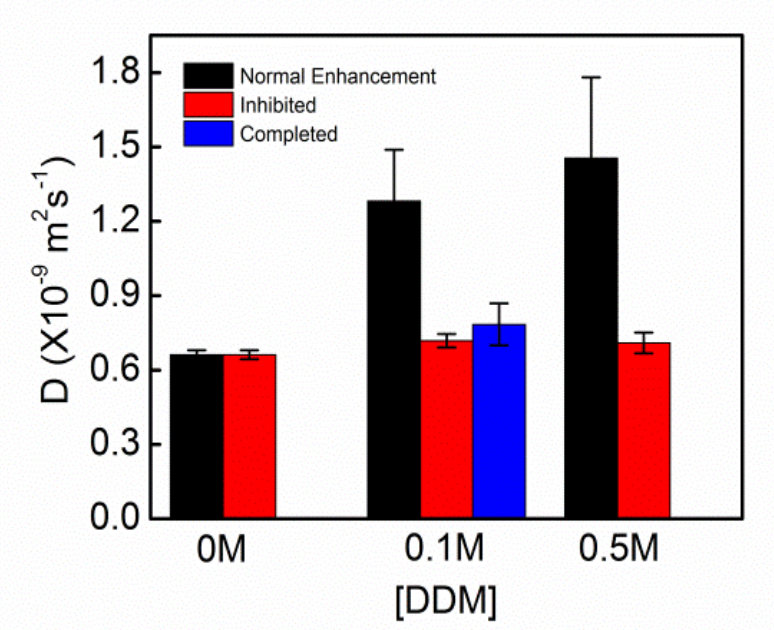

Figure 3-2: (A) Diffusion coefficients of Grubbs' catalyst over a range of concentrations of DDM. The diffusion increases as the concentration is increased saturating at around 0.1 M. (B) Diffusion coefficient of the catalyst with the addition of an inhibitor and after the reaction has reached equilibrium. The diffusion coefficient is reduced to the base value in presence of the inhibitor and when the reaction reaches equilibrium.

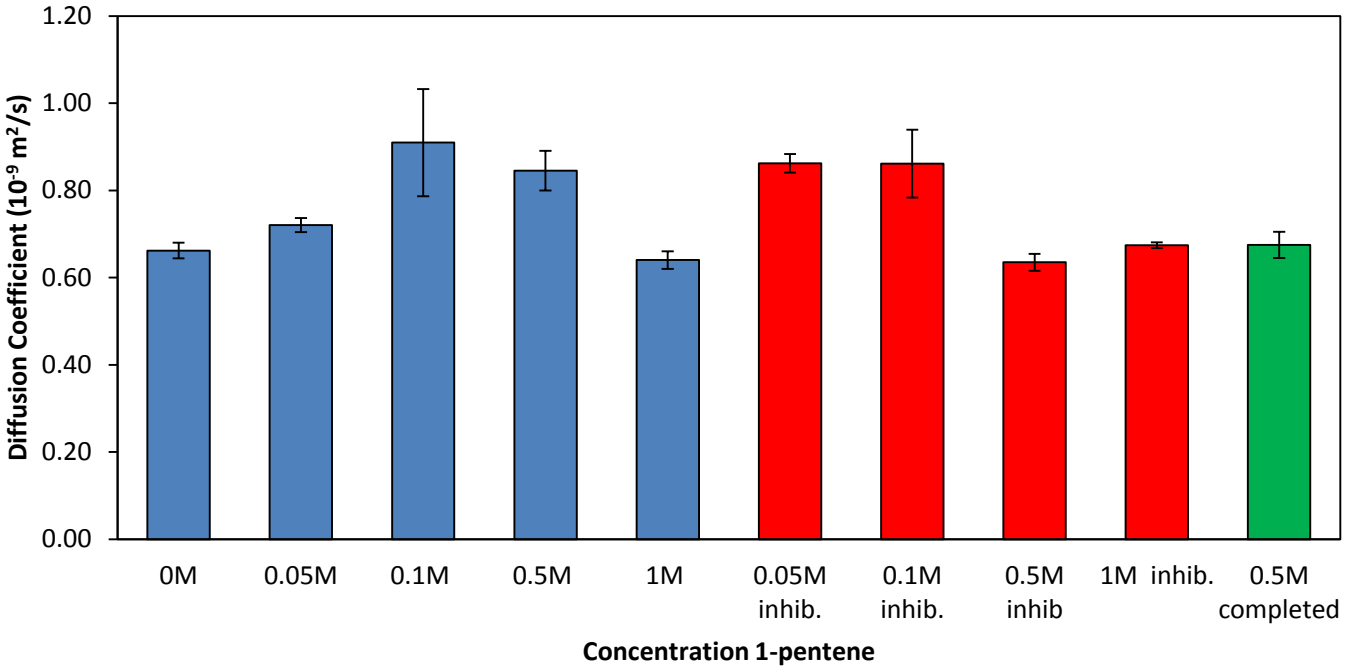

Fig 3-3: Diffusion coefficient at various concentrations of 1-pentene. Controls were run with inhibitor and after the reaction was completed. No significant change in diffusion was observed.

3.3 Measurement of turnover frequency (TOF)

While the rate constants are known in the literature[35,36], the turnover frequencies (TOF) were measured experimentally for all of the concentrations. The TOF were calculated from experiments run for 30 min with NMR spectra taken every 10 min. The ethyl protons at the *1* position were standardized to integrate to 6 protons (Figure 3-4). The integration value for the protons at position *3* was divided by 4 to find the percent of substrate left in solution. This was then related to a molar value since the starting amount of substrate was known. The moles of substrate left in solution was plotted versus time and a linear fit was used to extrapolate the reaction rate (mol sub./s). The velocity was then divided by the amount of catalyst in solution to obtain the TOF. The results are summarized in Table S3. It should be noted that all the measured TOFs are close to the values found in the literature[35,36]. There is a direct relationship between the TOF and diffusion coefficient (Figure 3-5).

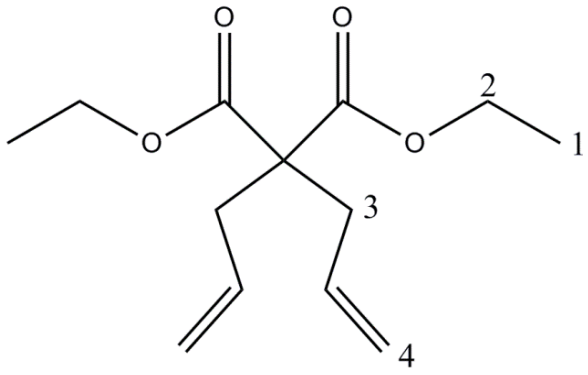

Figure 3-4: Structure of diethyl diallyl malonate.

Table 3-3: TOF for the catalyst at varying concentrations of DDM and the concentration of substrate after the initial 15min equilibration period.*

Conc.	TOF*	Conc. After 15 min (M)
0M DDM	0	0.00
0.01M DDM	8.30E-04	0.01
0.02 DDM	1.50E-03	0.02
0.05M DDM	2.20E-03	0.04
0.1M DDM	4.20E-03	0.09
0.5M DDM	9.70E-03	0.47
0.5M 1-pentene	1.00E-02	0.5

*Measured in moles of substrate per mole of catalyst per sec. Measured at 295K in $CDCl_3$ by a DPX-300MHz Bruker NMR. Catalyst concentration is 3mM.

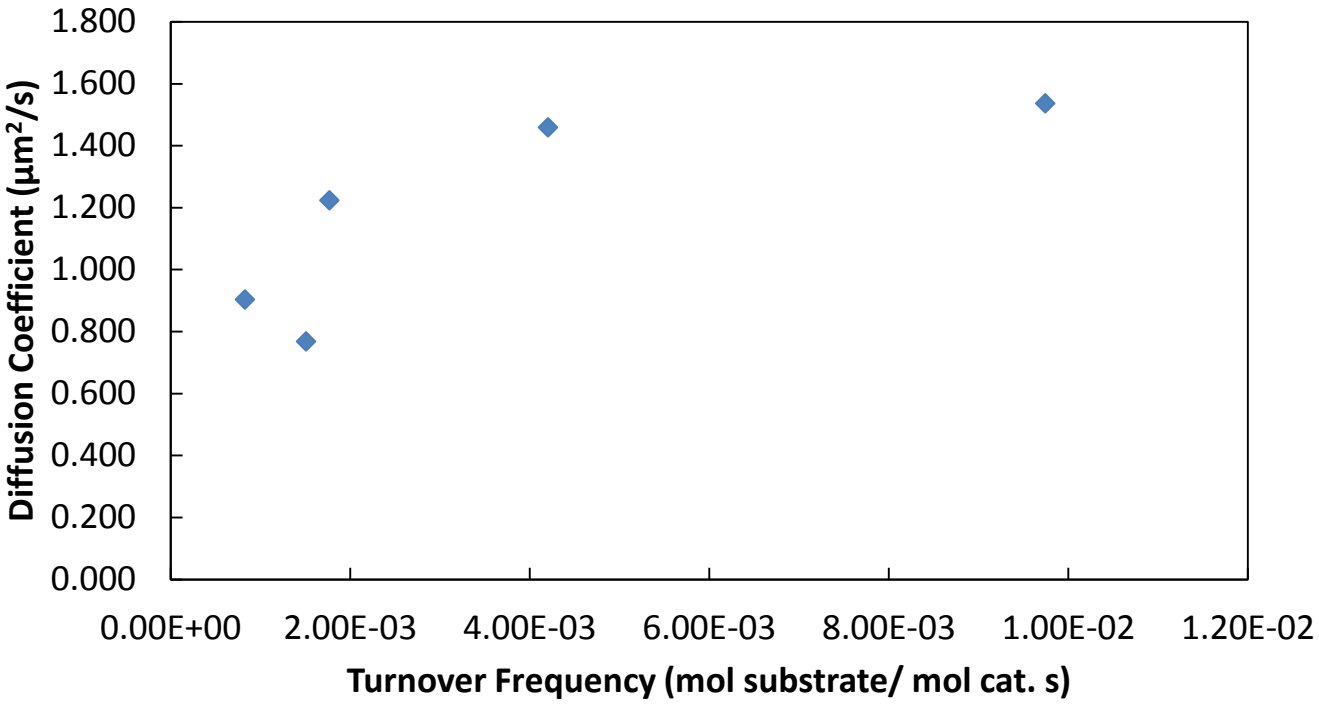

Figure 3-5: Correlation between diffusion coefficient and turnover frequency.

3.4 Enhanced Diffusion Mechanism

3.4.1 Structural Changes

To determine the origin of the enhanced diffusive motion in the presence of the substrate, we first evaluated the structural changes that occur during the catalytic cycle. There are two physical transformations the catalyst goes through that cause a decrease in its hydrodynamic radius. One is the dissociation of the coordinating phosphine and the other is the conversion of the pendent phenyl carbene to a methylidene moiety (Figure 3-6). Density functional theory (DFT) calculations were performed to probe each of these structural changes (Figure 3-7). In particular, molecular volume and effective radii were calculated for the species in Figure 3-7

(Table 3-4). The effective radius for species **1** (H_2IMes)(PCy_3)Cl_2Ru=CHPh (Grubbs' catalyst), obtained from DFT calculations was close to that experimentally calculated from the diffusion data (in the absence of substrate) using the equation:

$$D = \frac{kT}{6\pi\eta a} \tag{3-2}$$

where D is the diffusion coefficient, k is the Boltzmann constant, T is temperature, η is viscosity, and *a* is the particle radius. It should be noted that there is only a 20% difference between the largest and the smallest form of the catalyst; too small to account for the increased catalyst diffusivity at most substrate concentrations.

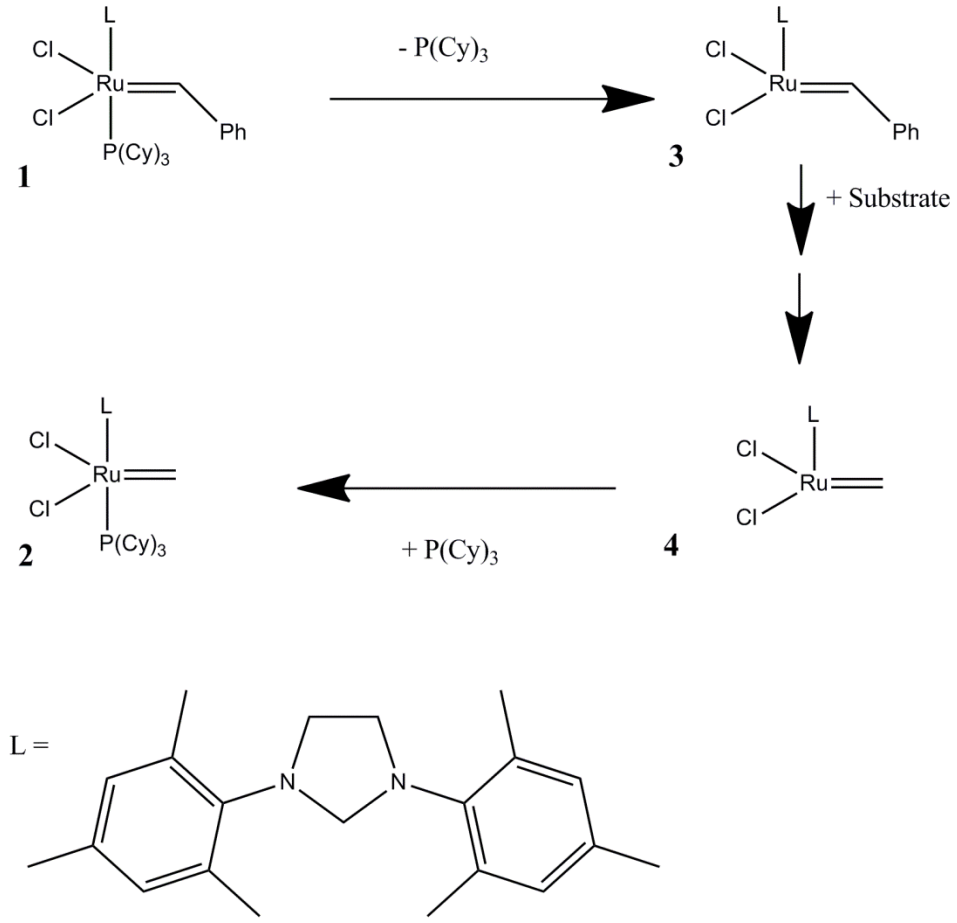

Figure 3-6: Structural changes to the catalyst molecule during the catalytic cycle.

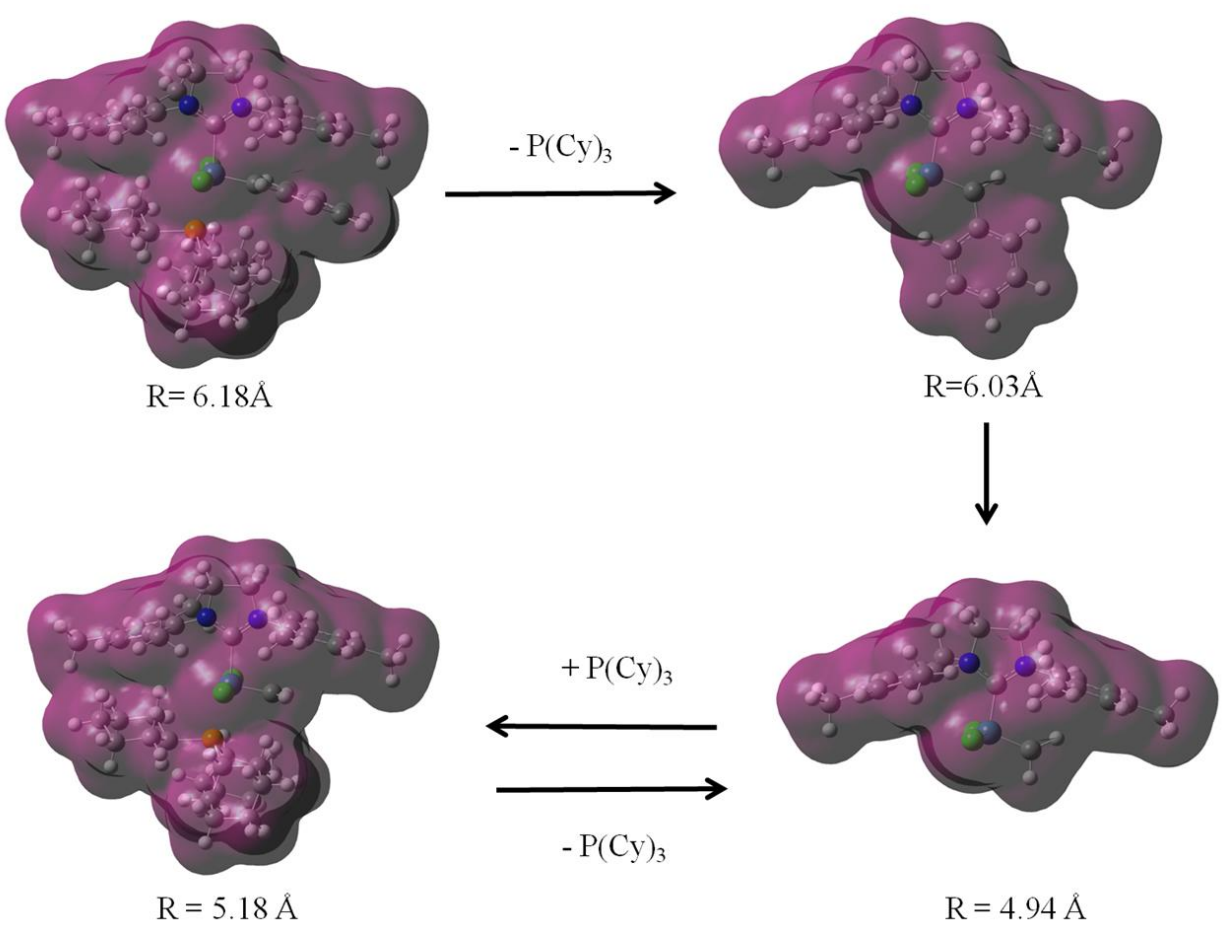

Figure 3-7: DFT calculated structures for (top left) $(H_2IMes)(PCy_3)Cl_2Ru=CHPh$, (bottom left) $(H_2IMes)(PCy_3)Cl_2Ru=CH_2$, (top right) $(H_2IMes)Cl_2Ru=CHPh$ (bottom-right) $(H_2IMes)Cl_2Ru=CH_2$, showing the change in effective radius during the catalytic cycle.

Table 3-4: Calculated effective radii from DFT of various intermediates.

Structure	System	Molecular volume ($Å^3$/mol)	Effective Radius from Volume (Å)	Difference (%)
1	$(H_2IMes)(PCy_3)Cl_2Ru=CHPh$	989.9230	6.18	-
2	$(H_2IMes)(PCy_3)Cl_2Ru=CH_2$	920.5719	6.03	2.4
3	$(H_2IMes)Cl_2Ru=CHPh$	580.7381	5.18	16.2
4	$(H_2IMes)Cl_2Ru=CH_2$	506.0585	4.94	20.1

3.4.2 Density functional theory calculations of molecular volume, radius and energetics

Computational calculations were performed using Gaussian 09.[37] Geometry optimizations of the ruthenium-containing species were performed using density functional theory (DFT) with the M06-2X functional [38] and the def2-SVP basis set .[39,40] The M06-2X functional has been shown to perform reliably for this class of catalysts with respect to geometries and thermochemical calculations.[41] Molecular volumes of the optimized species at each step in the catalytic cycle (Figure 3-7) were calculated from the volume contained within a contour of 0.001 electrons/bohr of electronic density at the M06-2X/SVP level (Table 3-4). Geometry optimizations of the CM and RCM reactants and products were performed using DFT with the M06-2X functional and the 6-311++G** basis set.[42] Geometries of the solvated species were optimized in solution using the conductor-like polarizable continuum model (C-PCM) method[43,44] with ε=4.711300 and ε_∞=2.090627. Analytic frequency calculations were performed on the optimized structures (with appropriate solvation) in order to calculate the relevant thermochemical quantities at 298K at the M06-2X/6-311++G** level. The enthalpies and free

energies of the CM reaction calculated using DFT were found to be similar to corresponding MP2/6-311++G** calculations.

For ring closing metathesis, the enthalpy of reaction was 7.9 kcal/mol and the free energy of reaction was -2.2 kcal/mol. For cross metathesis (Z-4-octene product), the enthalpy of reaction was 2.2 kcal/mol and the free energy of reaction was -3.7 kcal/mol. For cross metathesis (E-4-octene product) the enthalpy of reaction was 3.4 kcal/mol and the free energy of reaction was -2.6 kcal/mol.

3.5 ^{31}P NMR spectroscopy of the phosphine ligand

Experimental studies were also performed to help support the computational work. For the case of phosphine dissociation it is known that the ligand dissociates and re-associates even without the presence of substrate since catalysis proceeds through a dissociative pathway.[45-47] Thus, the base diffusion coefficient (without substrate) should encompass an average of both bound and unbound states. P^{31} NMR spectra were taken of the catalyst with and without the presence of substrate at room temperature. In both cases, there was only one resonance at 29 ppm. This single peak suggests that, at ambient temperature, the disassociation and re-association of the phosphine is slower than the NMR timescale and favors the bound state, which is consistent with the literature reports (Table 3-5).[35] The resonance for the unbound appears around 10 ppm.[48] This implies that while physical transformations can lead to a 20% increase in diffusion coefficient, it is unlikely that they contribute significantly to the observed enhancement.

The ^{31}P NMR signal for the phosphine ligand was monitored in the absence and presence of substrates, Table S4. There is only one observable resonance whose position did not change significantly. Thus, we conclude that the dissociation of the phosphine from the metal center is slow compared to the NMR time scale.

Table 3-5: ^{31}P NMR data for Grubbs' 2nd generation catalyst in the absence and presence of substrates.*

Substrate	Shift (ppm)	Remarks
0 M DDM	29.05	
0.05MDDM	29.04	
0.1MDDM	29.02	
0.1MDDM	28.96	Inhibited
0.1MDDM	29.00	Completed
0.5MDDM	28.96	
0.5MDDM	28.96	15 min. later
0.5M 1-Pentene	29.03	

* Measured at 295K in 0.6ml $CDCl_3$ by a AV-360MHz Bruker NMR with a ^{31}P-NMR probe. Catalyst concentration is 3mM and Inhibitor concentration is 0.2M.

3.6 Phoretic Effect

Thus, the positive entropic component of the free energy must play a role, suggesting the possibility of a phoretic mechanism. In the specific RCM reaction, two product molecules are formed for each substrate molecule consumed. This will result in a significant chemical gradient. In the CM reaction, two substrate molecules are converted into two product molecules and the chemical gradient formed will be lower. There will, however, still be a slight gradient because of

a difference in diffusion coefficients between the reactants and the products. Chemical gradients have been shown to theoretically cause an increase in motility if the catalyst encounters more collisions on one side than the other.[49-54] In the present case, however, the fast rotational time of the relatively small catalyst molecule and the fast diffusion times of the reaction products should prevent the generation of a sustained chemical gradient across the catalyst surface. Thus, the precise mechanism underlying the substrate-induced enhanced diffusion remains to be elucidated.

3.7 Efficiency

Irrespective of the actual propulsion mechanism, to ascertain that the observed enhanced diffusion is the result of the catalytic reaction; we calculated the ratio of the energy required for the enhanced diffusivity of the catalyst ensemble to the energy produced by the ensemble through catalysis. The resulting efficiency was ~10^{-6}%. While our system is inefficient, this does show that there is enough energy released in our system to account for the observed enhanced diffusion and establishes the viability of using catalytic reactions to power molecular motors.

Work done on a catalyst molecule due to a single turnover is given by,

$$\left(6\pi\eta Ru\right).\Delta d \tag{3-3}$$

where η is the coefficient of viscosity of the solvent (in N m^{-2} s), R is the radius of the catalyst molecule (in m), u is the velocity (in m/s) and d is the displacement of the molecule (in m) after the reaction. Rate of work done on the particle (in J/s) is,

$$\frac{\left(6\pi\eta Ru\right).\Delta d}{\Delta t} = 6\pi\eta Ru^2 \tag{3-4}$$

Considering N_{Cat} to be the number of moles of catalyst present in the system and ΔG to be the free energy of the system, then rate of production of free energy in the system is given by,

$$E = r \times \Delta G \times N_{\text{Cat}} \tag{3-5}$$

here, *r* is the turnover frequency measured in moles of substrate per mole of catalyst per sec.

If the efficiency of energy transformation is *e*, then the energy balance is,

$$6\pi\eta R u^2 = e.E = e.\left(r \times \Delta G \times N_{\text{Cat}}\right) \tag{3-6}$$

$$\text{or, } u^2 = \frac{e.\left(r \times \Delta G \times N_{\text{Cat}}\right)}{6\pi\eta R} \tag{3-7}$$

The rotational diffusion constant of a catalyst molecule is given by,

$$D_r = \frac{k_{\text{B}}T}{8\pi\eta R^3} \tag{3-8}$$

where k_{B} is the Boltzmann constant and T is the temperature of the system.

The diffusion enhancement is given by,

$$\Delta D = \frac{u^2}{4D_r} = \frac{e.\left(r \times \Delta G \times N_{\text{Cat}}\right) \times 8\pi\eta R^3}{4 \times 6\pi\eta R \times k_{\text{B}}T} = \frac{1}{3}\frac{R^2}{k_{\text{B}}T} e.\left(r \times \Delta G \times N_{\text{Cat}}\right) \tag{3-9}$$

$$\text{or, } e = \frac{3k_{\text{B}}T}{R^2\left(r \times \Delta G \times N_{\text{Cat}}\right)} \Delta D \tag{3-10}$$

We take the values of different parameters as follows $k_B = 1.38\times10^{-23}$ J K^{-1}, $T = 298$ K, $R = 6\times10^{-10}$ m, $\Delta D = 9\times10^{-10}$ m^{2}s^{-1} (Maximum enhancement in diffusion observed), $r = 9.7\times10^{-3}\,\frac{(\text{moles of substrate})}{(\text{moles of catalyst}).\,\text{s}}$, $\Delta G = 2.2\ \frac{\text{kcal}}{\text{moles of substrate}} = 9.21\ \text{x}10^3\ \frac{\text{J}}{\text{moles of substrate}}$, and $N_{Cat} = 3.6\times10^{-5}$ moles . Then from Eq. (3-10) we then have: e = 9.31x10^{-9}. Therefore, efficiency of energy conversion of this system is 9.31x10^{-9} % .

3.8 Conclusion

We have demonstrated that a working molecular catalyst can generate sufficient mechanical force to cause its own movement. This observation is consistent with those reported for single enzyme molecules.[5] The use of organometallic catalysts as chemomechanical transducers would vastly expand the available methods for powering nano- and micromotors due to their great diversity. These motors are expected to find applications in bottom-up assembly of structures, pattern formation, cargo delivery at specific locations, roving sensors, and related functions.

3.9 References

1. Goel, A.; Vogel, V. *Nat. Nanotech.* **2008**, *3*, 465.
2. Lipowsky, R.; Chai, Y.; Klumpp, S.; Liepelt, S.; Muller, M.J.I. *Physica A*, **2006**, *372*, 34.
3. Carlier, M.F.; Wiesner, S.; Clainche, C.L.; Pantaloni, D. *C.R. Biologies*. **2003**, *326*, 161.
4. Yu, H.; Jo, K.; Kounovsky, K. L.; de Pablo, J. J.; Schwartz, D. C. *J. Am. Chem. Soc.*, **2009**, *131*, 5722.

5. Muddana, H.S.; Sengupta, S.; Mallouk, T. E.; Sen, A.; Butler, P. J. *J. Am. Chem. Soc.* **2010**, *132*, 2110.
6. Schalley, C.A.; Beizai, K.; Vogtle, F. *Acc. Chem. Res*.**2001**, *34*, 465.
7. van Delden, R.A.; terWiel, M.K.J.; Pollard, M.M.; Vicario, J.; Koumura, N.; Feringa, B.L. *Nature*. **2005**, *437*, 1337.
8. Shirai, Y.; Osgood, A.J. ; Zhao, Y.; Kelly, K.F.; Tour, J.M. *Nano Lett.* **2005**, *5*, 2330.
9. Kay, E. R.; Leigh, D. A.; Zerbetto, F. *Angew. Chem. Int. Ed.* **2000**, *46*, 72.
10. Tseng, H. R; Vignon, S. A.; Stoddart, J. F. *Angew. Chem. Int. Ed.* **2003**, *115*(13), 1529.
11. Flood, A. H.; Stoddart, J. F.; Steurman, D. W.; Heath, J. R. *Science*, **2004**, *306*(5704), 2055.
12. Feringa, B. L. *J. Org. Chem.*, **2007**, *72*(18), 6635.
13. Li, D.; Paxton, W. F.; Baughman, R. H.; Huang, T. J.; Stoddart, J. F.; Weiss, P. S. *MRS Bulletin*, **2009**, *34*(9), 671.
14. Michl, J.; Sykes, E. C. H. *ACS Nano*. **2009**, *3* (5), 1042.
15. Khajn, R.;, Stoddart, J. F.; Grzybowski, B. A. *Chem. Soc. Rev.* **2010**, *39*, 2203.
16. Astumian, R. D. *Biophysical Journal*, **2010**, *98*, 2401.
17. Coskun, A.; Banaszak, M.; Astumian, R. D.; Stoddart, J. F.; Grzybowski, B. A. *Chem. Soc. Rev.*, **2012**, *41*, 19
18. Kline, T. R.; Paxton, W. F.; Wang, Y.; Velegol, D.; Mallouk, T. E.; Sen, A. *J. Am. Chem. Soc.* **2005**, *127*, 17150.
19. Paxton, W.F.; Sundararajan, S.; Mallouk, T.E.; Sen, A. *Angew. Chem. Int. Ed.* **2006**, *45*, 5420.
20. Ibele, M. E.; Wang, Y.; Kline, T. R.; Mallouk, T. E.; Sen, A. *J. Am. Chem. Soc.* **2007**, *129*, 7762.
21. Wang, J. *ACS Nano*. **2009**, *3*, 4.
22. Sanchez, S.; Pumera, M. *Chem. Asian. J.* **2009**, *4*, 1402.
23. Mirkovic, T.; Zacharia, N.S.; Scholes, G.D.; Ozin, G.A. *Small.* **2010**, *6*, 159.
24. Hong, Y.; Velegol, D.; Chaturvedi, N.; Sen, A. *Phys. Chem. Chem. Phys.* **2010**, *12*, 1423.
25. Wang, J.; Manesh, K.M. *Small,* **2010**, *6*, 338.
26. Jun, I.K.; Hess, H. *Adv.Mater*. **2010**, *22*, 4823.
27. Mei, Y.F.; Solovev, A.A.; Sanchez, S.; Schmidt, O.G. *Chem. Soc. Rev.* **2011**, *40*, 2109.
28. Pavlick, R.A.; Sengupta, S.; McFadden, T.; Zhang, H.; Sen, A. *Angew. Chem. Int. Ed.* **2011**, *50*, 9374.
29. Zhang, H.; Yeung, K.; Robbins, J. S.; Pavlick, R. A.; Wu, M.; Liu, R.; Sen, A.; Phillips, S. T. *Angew. Chem. Int. Ed.* **2012**, *51*, 2400.
30. Sengupta, S.; Ibele, M. E.; Sen, A. *Angew. Chem. Int. Ed.* **2012**, *51*, 8434.
31. Ebbens, S.J.; Howse, J.R. Soft Matter, **2012**, *8*, 3077.
32. Wu, D.; Chen, A.; Johnson, C. S. *J. Magnetic Resonance, Series A.* **1995**, *115*, 260.
33. Price, K.E.; Lucas, L.H.; Larive, C.K. *Anal Bioanal Chem.***2004**, *378*, 1405.
34. Pregosin, P.S. *Prog. Nucl. Mag. Res. Spec.,* **2006**, *49*, 261.
35. Sanford, M.S.; Love, J. A.; Grubbs, R. H. *J. Am. Chem. Soc.***2001**, *123*, 6543.
36. Booyens, S.; Roodt, A.; Wendt, O. F. *J. Organometallic Chemistry.* **2007**, *692*, 5508.
37. Frisch, M. J.; Trucks, G. W.; Schlegel, H. B.; Scuseria, G. E.; Robb, M. A.; Cheeseman, J. R.; Scalmani, G.; Barone, V.; Mennucci, B.; Petersson, G. A.; Nakatsuji, H.; Caricato,

M.; Li, X.; Hratchian, H. P.; Izmaylov, A. F.; Bloino, J.; Zheng, G.; Sonnenberg, J. L.; Hada, M.; Ehara, M.; Toyota, K.; Fukuda, R.; Hasegawa, J.; Ishida, M.; Nakajima, T.; Honda, Y.; Kitao, O.; Nakai, H.; Vreven, T.; Montgomery, J. A.; Peralta, J. E.; Ogliaro, F.; Bearpark, M.; Heyd, J. J.; Brothers, E.; Kudin, K. N.; Staroverov, V. N.; Kobayashi, R.; Normand, J.; Raghavachari, K.; Rendell, A.; Burant, J. C.; Iyengar, S. S.; Tomasi, J.; Cossi, M.; Rega, N.; Millam, J. M.; Klene, M.; Knox, J. E.; Cross, J. B.; Bakken, V.; Adamo, C.; Jaramillo, J.; Gomperts, R.; Stratmann, R. E.; Yazyev, O.; Austin, A. J.; Cammi, R.; Pomelli, C.; Ochterski, J. W.; Martin, R. L.; Morokuma, K.; Zakrzewski, V. G.; Voth, G. A.; Salvador, P.; Dannenberg, J. J.; Dapprich, S.; Daniels, A. D.; Farkas, J. B.; Foresman, J. V.; Ortiz; Cioslowski, J.; Fox, D. J. Gaussian 09, Revision B.01 (Wallingford CT, 2009).

38. Zhao, Y.; Truhlar, D. G. *Theor. Chem. Acc.***2008**, *120*, 215.
39. Andrae, D.; Haussermann, U.; Dolg, M.; Stoll, H.; Preuss, H. *Theor. Chim. Acta* **1990**, *77*, 123.
40. Weigend, F.; Ahlrichs, R. *Phys. Chem. Chem. Phys.* **2005**, *7*, 3297.
41. Eshuis, H.; Furche, F. *J. Phys. Chem. Lett.* **2011**, *2*, 983.
42. Krishnan, R.; Binkley, J. S.; Seeger, R.; Pople, J. A. *J. Chem. Phys.* **1980**, *72*, 650.
43. Barone, V.; Cossi, M. *J. Phys. Chem. A* **1998**, *102*, 1995.
44. Cossi, M.; Rega, N.; Scalmani, G. ; Barone, V. *J. Comput. Chem.* **2003**, *24*, 669.
45. Trnka, T.M.; Day, M.W.; Grubbs, R.H. *Angew. Chem. Int. Ed.* **2001**, *40*, 3441.
46. Sanford, M.S.; Love, J.A.; Grubbs, R.H. *J. Am. Chem. Soc.***2001**, *123*, 6543.
47. Love, J.A.; Sanford, M.S.; Day, M.W.; Grubbs, R.H. *J. Am. Chem. Soc.***2003**, *125*, 10103.
48. Schraml, J.; Capka, M.; Blechta, V. *Magnetic Resonance in Chemistry*. **1992**, *30*, 544.
49. Golestanian, R.; Liverpool, T.B.; Ajdari, A. *Phys. Rev. Lett.* **2005**, *94*, 220801.
50. Ruckner, G.; Kapral, R. *Phys. Rev. Lett.* **2007**, *98*, 150603.
51. Co´rdova-Figueroa, U. M.; Brady, J. F. *Phys. Rev. Lett.* **2008**, *100*, 158303.
52. Delogu, F. *J. Phys. Chem. C.* **2009**, *113*, 15909.
53. Ebbens, S.; Jones, R.A.L.; Ryan, A.J.; Golestanian, R.; Howse, J.R. *Phys. Rev. E.* **2010**, *82*, 015304.
54. Ke, H.; Ye, S.; Carroll, R.L.; Showalter, K. *J. Phys. Chem. A.* **2010**, *114*, 54

Chapter 4

Dynamic Coupling at the Nanoscale

4.1 Introduction

Synthetic systems that display collective behavior are of interest due their similarities to biological systems. These systems include microparticles that move and interact through self-generated overlapping ion gradients.[1-3] These synthetic active systems display unusual reversible patterning behavior in the presence of a chemical stimulus. Recently, another mechanism of inter-particle coupling has been reported in the literature, where a particle in motion transfers its momentum to a non-motive particle through hydrodynamic coupling. This process was previously thought to be insignificant at low Reynolds number regimes since inertial forces are dissipated rapidly due to the dominant role of viscosity.[4-6] However, Mino has shown that both active bacteria and bimetallic catalytic nanorods transfer their momentum to surrounding tracer particles at the micron scale, resulting in enhanced diffusive motion of the tracers.[7] Similarly, Gollub has reported that when algal cells were allowed to swim through a suspension of tracer particles, the particles exhibited enhanced motion.[8,9] The study postulated that the algae generate hydrodynamic perturbations in the surrounding fluid as they swim, thereby influencing the motion of the nearby tracers. In this paper, we show that such dynamic coupling can occur even for objects at the *sub-nm* regime. Our system consists of a collection of active organometallic molecular motors that exhibit a dynamic coupling between their motion and those in the nearby environment.

We recently reported a catalytically-driven molecular motor system that comprises of Grubbs' 2nd generation catalyst (hydrodynamic radius (R_H), 6 Å) and diethyl diallylmalonate

(DDM) as fuel.[10] The DDM is converted into the cyclic product, diethyl cyclopent-3-ene-1,1-dicarboxylate, and ethene via ring closing metathesis, RCM (Figure 4-1). The catalyst molecules, as a collective, displayed a diffusion coefficient up to twice the Brownian diffusion coefficient while performing the catalytic reaction.[10] Interestingly, this enhancement was observed even though the reaction is slightly *endothermic*. It was also observed that the increase in diffusion was dependent on the turnover frequency (TOF) of the reaction.[10] In contrast to the ring closing metathesis of DDM, the cross metathesis of 1-pentene, which involves the conversion of two 1-pentene molecules to 4-octene and ethene, showed no significant enhancement in catalyst diffusivity. While the detailed mechanism for enhanced diffusion remains to be elucidated, an entropically-driven phoretic mechanism remains a possibility.[11-17] In the specific ring closing metathesis reaction, two product molecules are formed for each substrate molecule consumed, resulting in a chemical gradient. In the cross metathesis reaction, two substrate molecules are converted into two product molecules and the formed chemical gradient will be significantly lower. Expanding on this work, we wished to determine if the catalyst influenced its environment as well as other catalyst molecules via the transfer of momentum, similar to what has been reported in the micron regime.[7-9] We employed diffusion ^{1}H Nuclear Magnetic Resonance (NMR) spectroscopy[10,18] to measure the diffusion coefficients of the catalyst and spectator molecules over a range of reaction rates and catalyst concentrations.

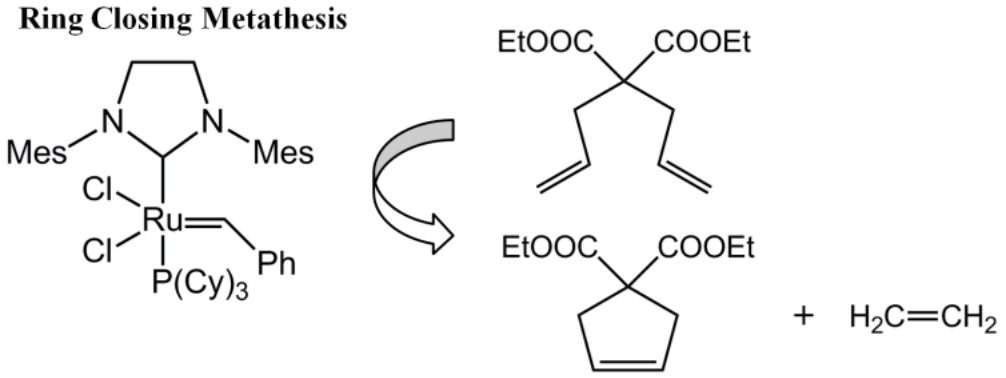

Figure 4-1: Schematic of the motor molecule catalyzing the ring closing metathesis of diethyl diallylmalonate.

4.2 Calculation of Diffusion Coefficient

Samples were prepared using between 1.0 to 10.0 mg of Grubbs' 2nd generation catalyst was dissolved in 1.2 mL of D-chloroform. Then, between 0.005 to 0.145mL of diethyl diallylmalonate was added (Table 4-1). For dichloromethane (DCM) an excess of 10 times the catalyst concentration was added to the catalyst solution (about 0.03M). For the polymer experiments, the concentration was 1.6 μM in the polymer solution of poly(dimethylsiloxane) monoglycidyl ether terminated M_n ~5000 (PDMS). For the cross metathesis (CM) experiments between 3.0 to 10.0 mg of catalyst was dissolved in 1.2 mL of d-chloroform. Then between 0.01 to 0.09ml of 1-pentene was added. Diffusion coefficients were calculated by using an 850 MHz NMR (Bruker) with a diffusion probe. The change in intensity was fit to the equation:

$$\ln\left(\frac{I}{I_0}\right) = -D\left(G\delta\gamma\right)^2\left(\Delta - \frac{\delta}{3} - \frac{\tau}{2}\right) \tag{4-1}$$

where I is the final resonance intensity, I_o is the initial intensity, D is the diffusion coefficient, G is the magnitude of the gradient, γ is the nuclear gyromagnetic ratio, δ is the gradient duration, τ

is the gradient relaxation time, and Δ is the time between gradient pulses.[18] Each sample was run three times and multiple samples were averaged together and then corrected for changes in viscosity, Table 4-1.

To analyze how the catalysts motion is influenced by the transfer of motion in the system, the diffusion coefficient was measured over several catalyst concentrations and rates (Figure 4-2). Then 0.6 mL of the solution was added to a NMR tube. The tube was allowed to equilibrate in the NMR for 15 minutes. The sample was then measured for the diffusion coefficient of the catalyst by focusing at the peak shift at 2.31 ppm.[10] Each sample was measured three times. This process was repeated for several catalyst concentrations and rates. As was previously reported[10] the enhancement in diffusion is directly related to the TOF of the catalyst at a given catalyst concentration. This was even observed over a greater range of rates and catalyst concentrations than was previously explored.

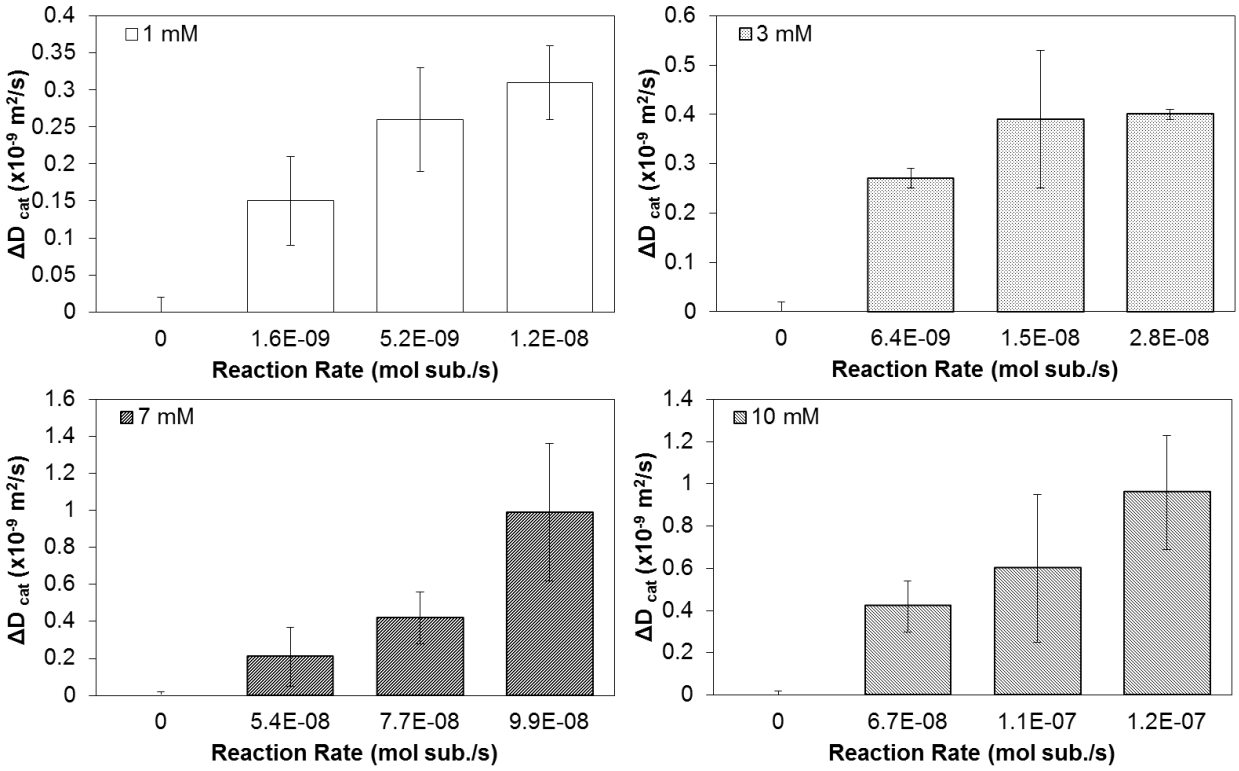

Figure 4-2: The change in diffusion coefficient of the catalyst as a function of reaction rate for four different catalyst concentrations. For each catalyst concentration, diffusivity increases with increasing DDM concentration due to the increase in total reaction rate in the system.

Table 4-1: Diffusion coefficients of the catalyst measured over a range of catalyst concentrations and rates. The T and P values were calculated by performing a two tailed equal variance T-test against the diffusion coefficient with no substrate.

Cat (mM)	Sub (M)	Diffusion Coefficient (10^{-9} m^2/s)	Stdev	T value	P value
1,3,7,10	0	0.66	0.02		
1	0.03	0.81	0.06	-7.0	0.0001
1	0.02	0.92	0.07	-10.7	0.0001
1	0.05	0.97	0.05	-16.9	0.0001
3	0.05	0.93	0.02	-25.6	0.0001
3	0.15	1.05	0.14	-8.4	0.0001
3	0.1	1.06	0.01	-45.0	0.0001
7	0.12	0.87	0.16	-4.0	0.0016
7	0.23	1.08	0.14	-9.0	0.0001
7	0.35	1.65	0.37	-8.0	0.0001
10	0.17	1.08	0.12	-10.4	0.0001
10	0.33	1.26	0.35	-5.1	0.0009
10	0.5	1.62	0.27	-10.6	0.0001

4.3 Diffusion of a Spectator (DCM)

In order to analyze how the enhanced catalyst motion influences the surrounding fluid, the diffusion of a spectator molecule, dichloromethane (DCM) (R_H, 1.4 Å), was observed over a range of catalyst concentrations and rates (Figure 4-3a). In 1.2 mL of chloroform-d, between 1.0 to 10.0 mg of Grubbs' 2nd generation catalyst was dissolved, followed by the addition of between 0.005 to 0.145 mL of diethyl diallylmalonate (Table 4-2). Then dichloromethane (DCM) was added so that it was in 10 times excess over the catalyst concentration. 0.6 mL of the solution was added to a NMR tube. The tube was allowed to equilibrate in the NMR spectrometer for 15

min. The sample was then measured for the diffusion coefficient of the spectator by focusing on the ^{1}H NMR peak for DCM. Each sample was measured three times. The diffusion of DCM is enhanced in the presence of the catalyst reaction. Furthermore, this enhancement was proportional to the reaction rate in the system. As a control, the diffusion was measured for cross metathesis (CM) using 1-pentene, which is known to not cause an enhancement in diffusion (Figure 4-3b).[10] As the reaction rate was increased in the presence of 1-pentene the diffusion did *not* increase to any significant degree. This confirms the catalyst molecules are only interacting through catalysis.

A

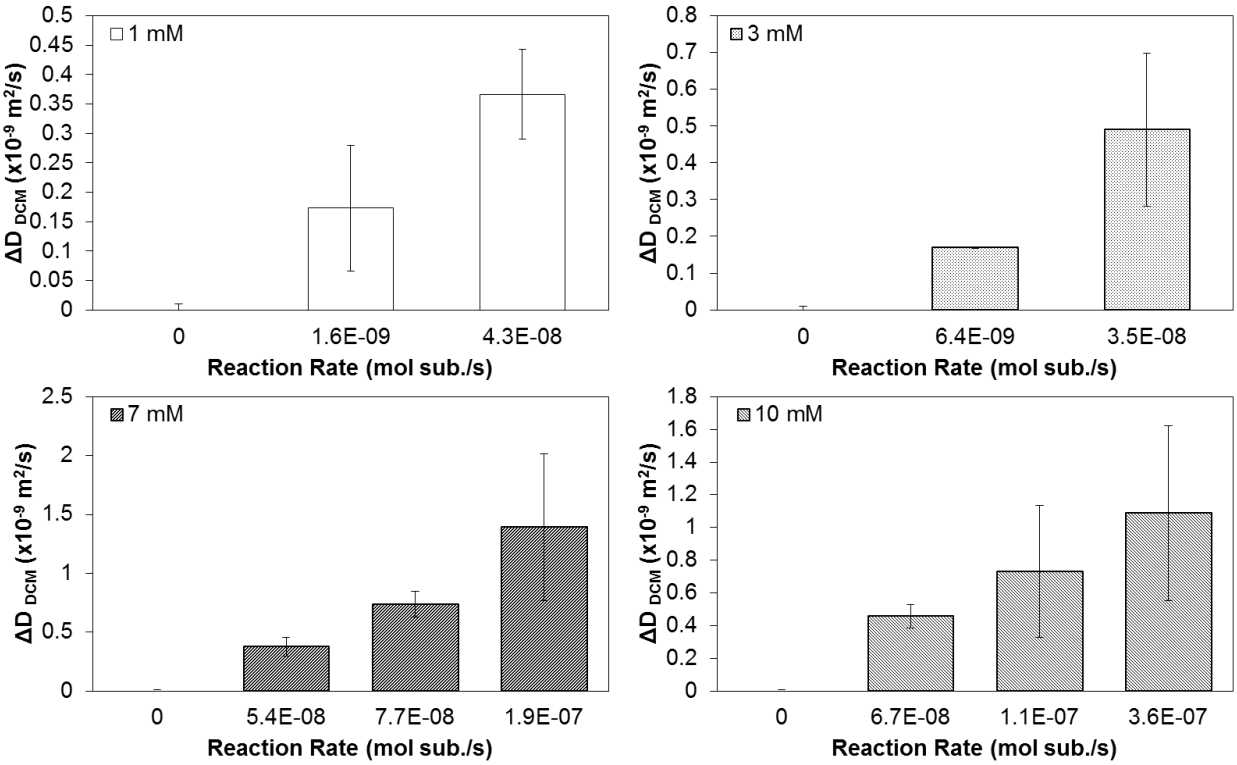
1 mM
3 mM
7 mM
10 mM
ΔD DCM (x10-9 m2/s)
Reaction Rate (mol sub./s)
0
1.6E-09
4.3E-08
6.4E-09
3.5E-08
5.4E-08
7.7E-08
1.9E-07
6.7E-08
1.1E-07
3.6E-07

B

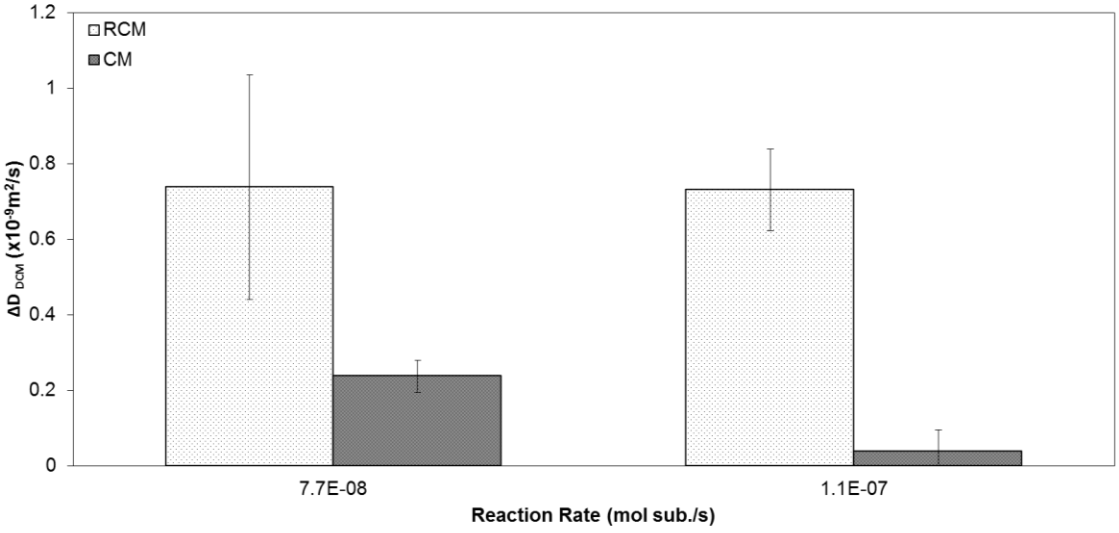
RCM
CM
ΔD DCM (x10-9m2/s)
7.7E-08
1.1E-07
Reaction Rate (mol sub./s)

Figure 4-3: (A) The change in diffusion coefficient of DCM as a function of reaction rate for four different catalyst concentrations. For each catalyst concentration, the diffusion increases with increasing DDM concentration due to the increase in total reaction rate in the system. (B) The change in diffusion coefficient of DCM in the presence of 1-pentene and DDM as a function of reaction rate. The cross metathesis of 1-pentene produced no significant increase in diffusion when compared to the ring closing metathesis of DDM, especially at higher rates.

Table 4-2: Diffusion coefficients of dichloromethane (DCM) measured over a range of catalyst concentrations and rates. The concentration of DCM was 0.03 M. The T and P values were calculated by performing a two tailed equal variance T-test against the diffusion coefficient with no substrate.

Cat (mM)	Sub (M)	Diffusion Coefficient (10^{-9} m^2/s)	Stdev	T value	P value
1,3,7,10	0	2.80	0.01		
1	0.03	2.97	0.11	-3.5	0.0243
1	0.17	3.17	0.08	-10.4	0.0005
3	0.05	2.97	0.00	-22.6	0.0001
3	0.5	3.29	0.21	-5.4	0.0058
7	0.12	3.18	0.08	-10.7	0.0004
7	0.23	3.54	0.11	-15.4	0.0001
7	1.17	4.19	0.62	-5.2	0.0066
10	0.17	3.26	0.07	-14.7	0.07
10	0.33	3.53	0.40	-4.2	0.0136
10	1.67	3.89	0.54	-4.7	0.0096

4.3.1 Increasing the amount of DCM

The enhanced motion of DCM was also monitored as the amount of DCM was increased compared to the catalyst concentration at a constant rate (Figure 4-4). There was no change in the diffusion of DCM at different DCM to catalyst ratios. This is consistent with the catalyst affecting the surrounding fluid and not just the spectator molecule directly.

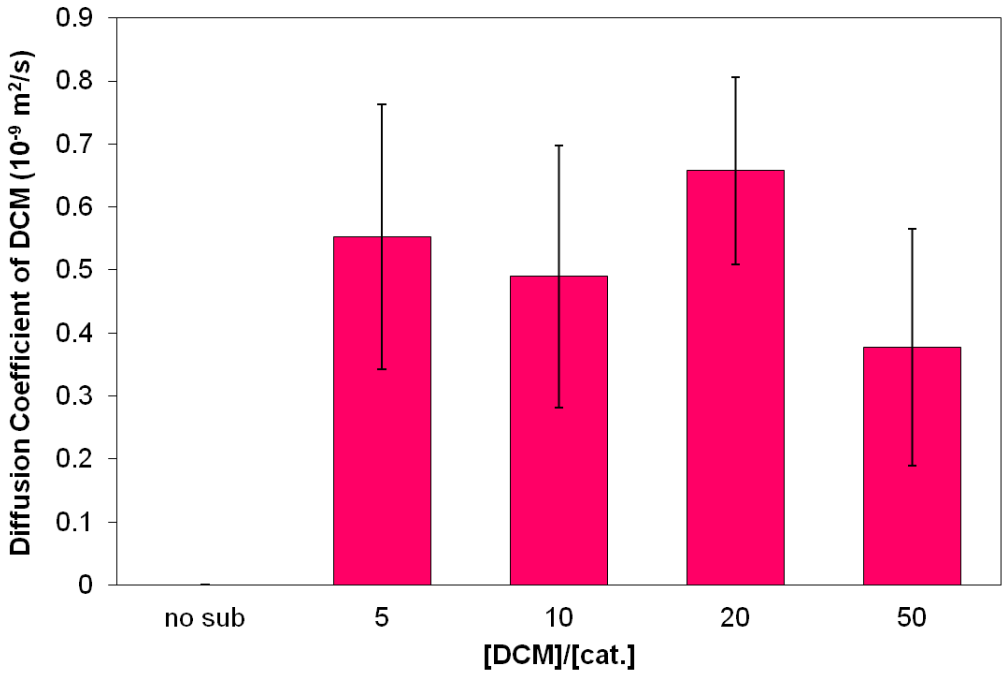

Figure 4-4: The diffusion of DCM was measured as the amount of DCM was increased compared to the catalyst concentration. There was a slight decrease in diffusion as the amount was raised from 5 times to 50 times.

4.4 Measurement of Reaction Rate

While the rate constants are known in the literature[19], the reaction rates were measured experimentally for all of the concentrations. The rates were calculated from experiments run for

30 min with NMR spectra taken every 10 min. The ethyl protons at the *1* position were standardized to integrate to 6 protons. The integration value for the protons at position *3* was divided by 4 to find the percent of substrate left in solution. This was then related to a molar value since the starting amount of substrate was known. The moles of substrate left in solution was plotted versus time and a linear fit was used to extrapolate the reaction rate (mol sub./s). The reaction rate was then divided by the amount of catalyst in solution to obtain the turnover frequency (TOF). The results are summarized in Table 4-3.

Table 4-3: Turnover frequencies and reaction rates of the catalyst at different substrate and catalyst concentrations.

Cat(mM)	Sub(M)	TOF (mol sub/ mol cat s)	Reaction Rate (mol sub./s)
1.0	0.02	1.32E-03	1.6E-09
1.0	0.03	4.40E-03	5.2E-09
1.0	0.05	1.00E-02	1.2E-08
1.0	0.17	3.64E-02	4.3E-08
1.6	0.28	3.44E-02	6.7E-08
2.1	0.07	6.18E-03	1.6E-08
2.9	0.05	1.80E-03	6.4E-09
2.9	0.10	4.20E-03	1.5E-08
2.9	0.15	7.80E-03	2.8E-08
2.9	0.50	1.00E-02	3.5E-08
4.0	0.07	2.91E-03	1.4E-08
6.9	0.12	6.60E-03	5.4E-08
6.9	0.23	9.37E-03	7.7E-08
6.9	0.35	1.20E-02	9.9E-08
7.0	0.81	2.28E-02	1.9E-07
9.4	0.48	1.20E-02	1.4E-07
9.8	0.17	5.69E-03	6.7E-08
9.8	0.33	9.39E-03	1.1E-07
9.8	0.50	9.96E-03	1.2E-07
10.0	1.67	3.01E-02	3.6E-07

4.5 Dependence on Reaction Rate

Over the range of reaction rates observed, the diffusion of both the catalyst (Figure 4-5) and the spectator molecule (DCM) show a near linear increase (Figure 4-6) - consistent with previous observations on advective displacement caused by active swimmers at the micron scale.[7,20-23] Our system, however, is the *smallest* motor system to display such coupling behavior. Higher total reaction rate in the system will cause an increased rate of net *momentum transfer*[7] through advective flows to the passive tracers causing a net enhancement in their diffusion. Mino *et al* have quantified the enhancement and found a linear dependence of the passive tracers' diffusion on the number density and average speed of micron-scale active swimmers, while Gollub showed a linear dependence between the volume fraction of the active algal swimmers and diffusion.[7-9] Both of these systems show a direct dependence of tracer diffusivity on the number of perturbations (reactions) occurring in the system. Remarkably, at the sub-nanometer scale, the diffusion of spectator molecules follows a similar linear relationship as the catalyst molecules themselves.

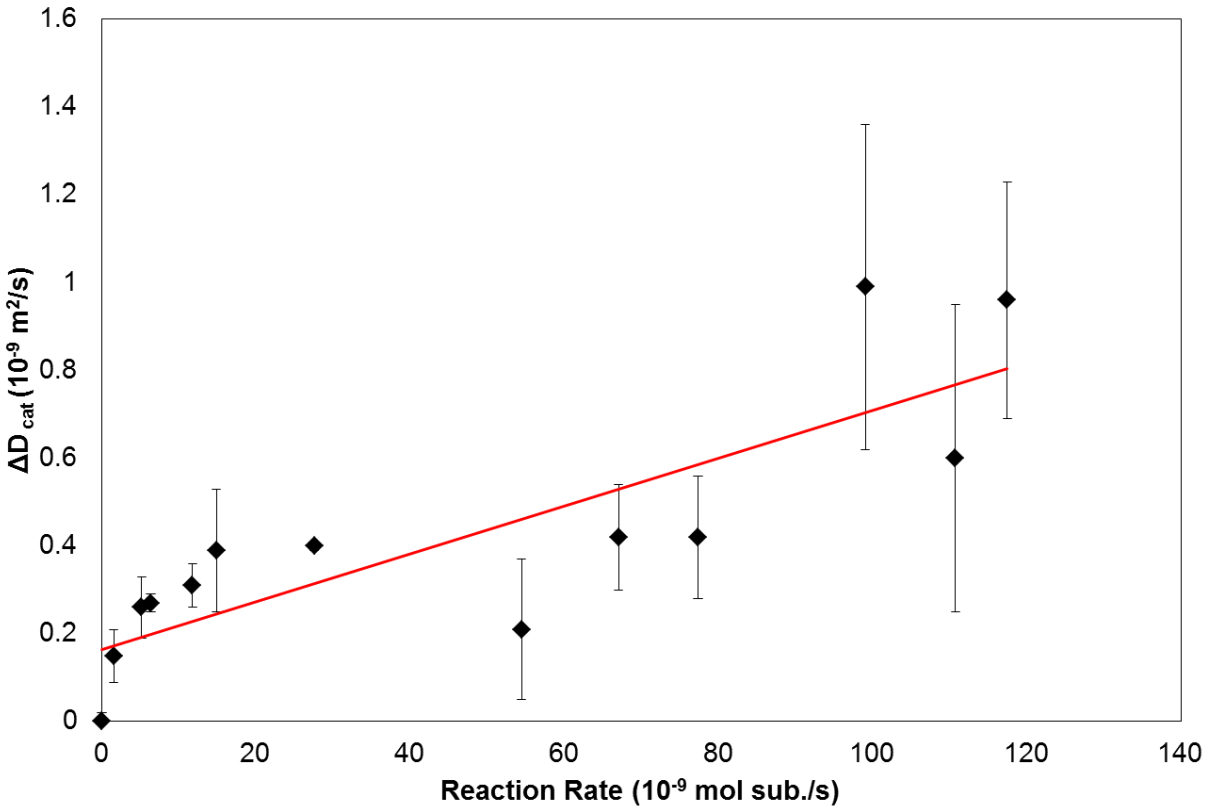

Figure 4-5. The change in diffusion of the catalyst was plotted against reaction rate of the system (mol sub. /s). The trend is generally linear, especially at high catalyst concentration.

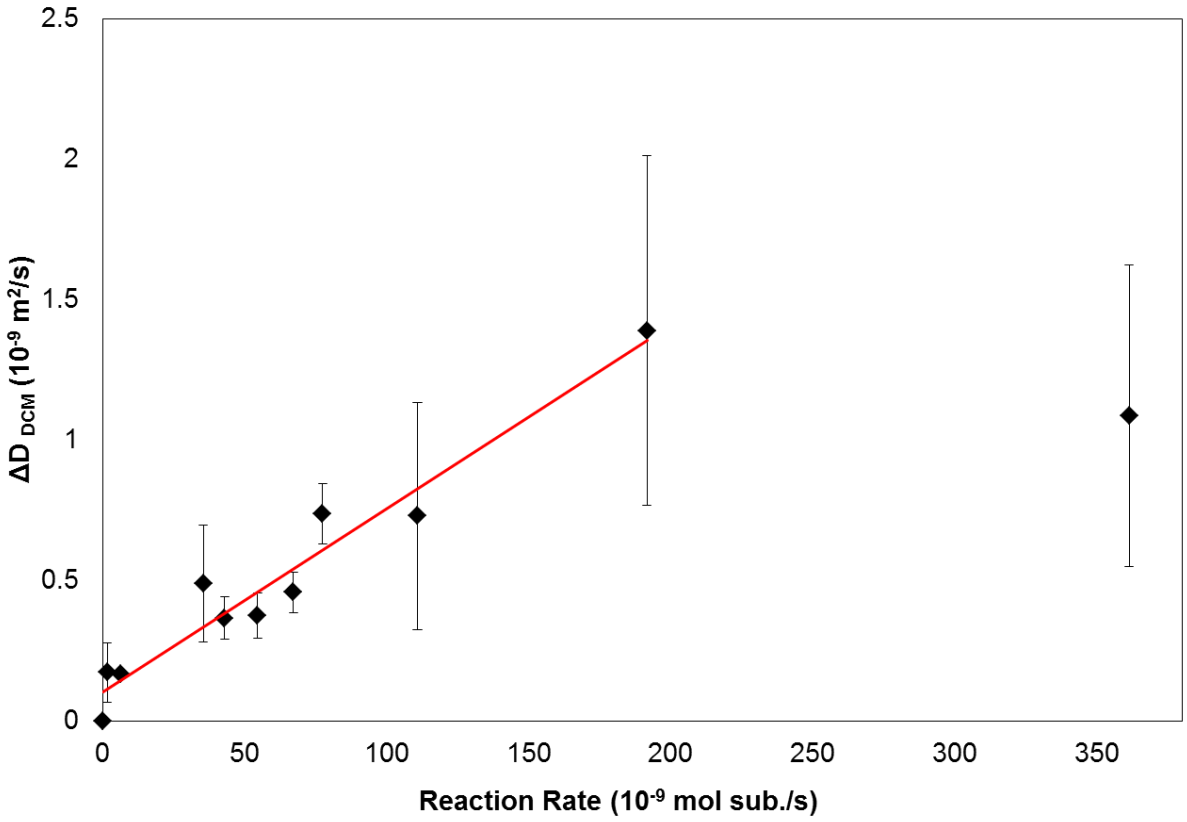

Figure 4-6. The change in diffusion of the catalyst was plotted against reaction rate of the system (mol sub. /s). The trend is generally linear but seems to saturate off at higher rates.

4.6 Dependence on Reaction Rate of a Polymer Tracer

We wished to see how this system affects the motion of a nanoscale object that is significantly larger than the catalyst. A polymer molecule, monoglycidyl ether-terminated poly(dimethylsiloxane), (PDMS; M_n, ~5000; R_H, 1.2 nm), was chosen as the object since its diffusion can be monitored via NMR spectroscopy (Table 4-4). The diffusion of the polymer was tracked as a function of catalyst concentration and rate (Figure 4-7). The polymer shows an enhanced diffusivity with the *same* reliance on rate as with the catalyst and DCM (Figure 4-8). Clearly, the coupling is strong enough to power the motion of a significantly larger molecule.

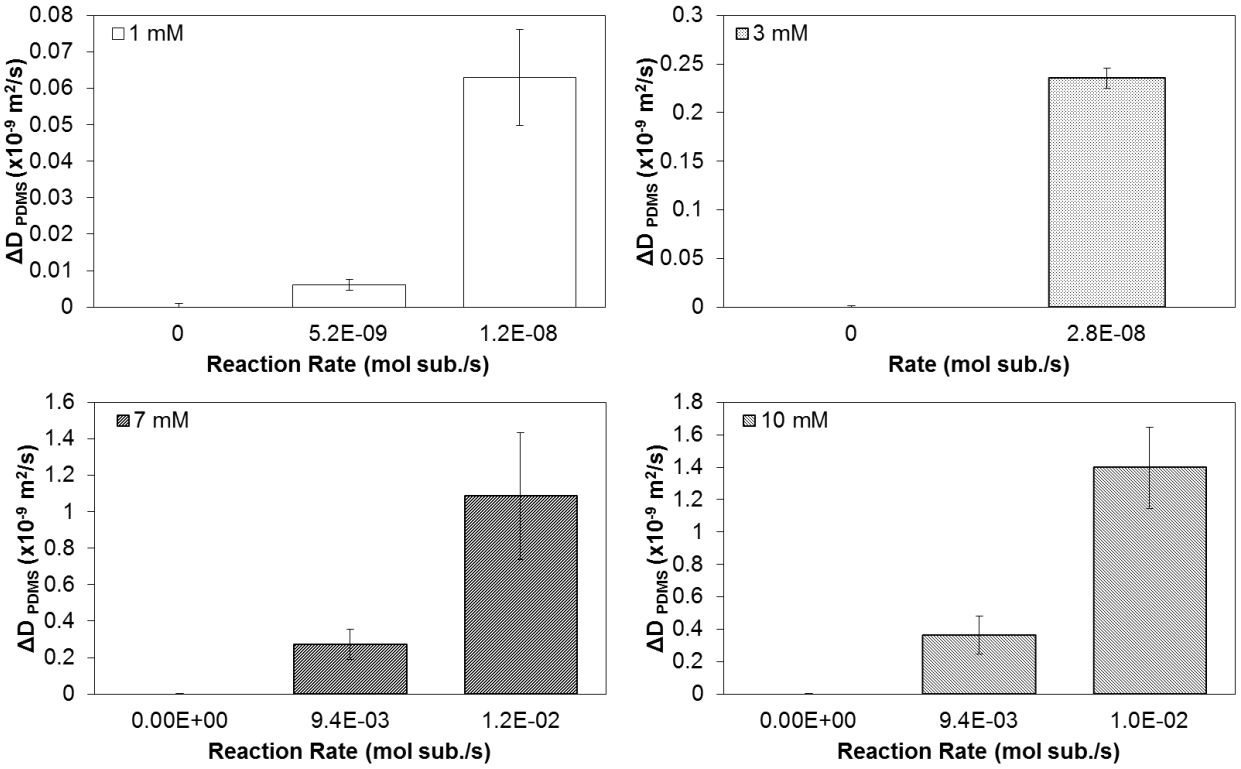

Figure 4-7. The change in diffusion coefficient of the PDMS as a function of reaction rate for four different catalyst concentrations. For each catalyst concentration the diffusion increases with increasing DDM concentration due to the increase total in reaction rate in the system.

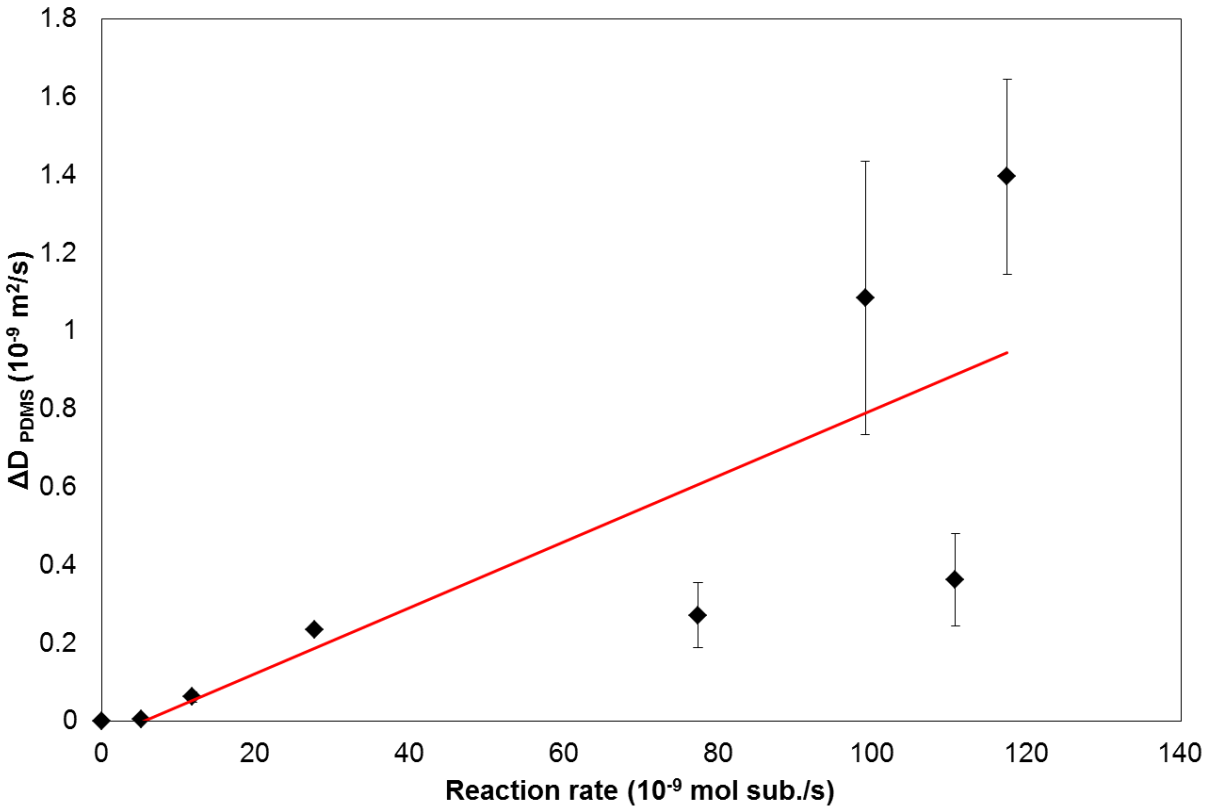

Figure 4-8. The change in diffusion of the polymer was plotted against reaction rate of the system (mol sub. /s). The trend is generally linear.

Table 4-4: Diffusion coefficients of monoglycidyl ether-terminated poly(dimethylsiloxane) M_n ~5000 (PDMS) measured over a range of catalyst concentrations and rates. The concentration of PDMS was 1.6 μM. The T and P values were calculated by performing a two tailed equal variance T-test against the diffusion coefficient with no substrate.

Cat (mM)	Sub (M)	Diffusion Coefficient (10^{-9} m^2/s)	Stdev	T value	P value
1,3,7,10	0	2.80	0.01		
1	0.03	2.97	0.11	-3.5	0.0243
1	0.17	3.17	0.08	-10.4	0.0005
3	0.05	2.97	0.00	-22.6	0.0001
3	0.5	3.29	0.21	-5.4	0.0058
7	0.12	3.18	0.08	-10.7	0.0004
7	0.23	3.54	0.11	-15.4	0.0001
7	1.17	4.19	0.62	-5.2	0.0066
10	0.17	3.26	0.07	-14.7	0.07
10	0.33	3.53	0.40	-4.2	0.0136
10	1.67	3.89	0.54	-4.7	0.0096

4.7 Effect of catalyst concentration at a Constant Reaction Rate

To expand on the work by Mino and Gollub, we wished to see if the observed diffusivity in our system was dependent on catalyst concentration or simply the reaction rate. We examined at the diffusion coefficient as a function of catalyst concentration keeping the number of reactions per unit time in the system constant, thus keeping the total disturbances in the system constant. For both the spectator and catalyst, there was no significant change in diffusion coefficient when increasing the catalyst concentration nearly 5 times (Figures 4-9, 4-10). This suggests that the enhanced motion in the system relies *solely* on the total reaction rate of the system and *not* on the number of catalyst molecules.

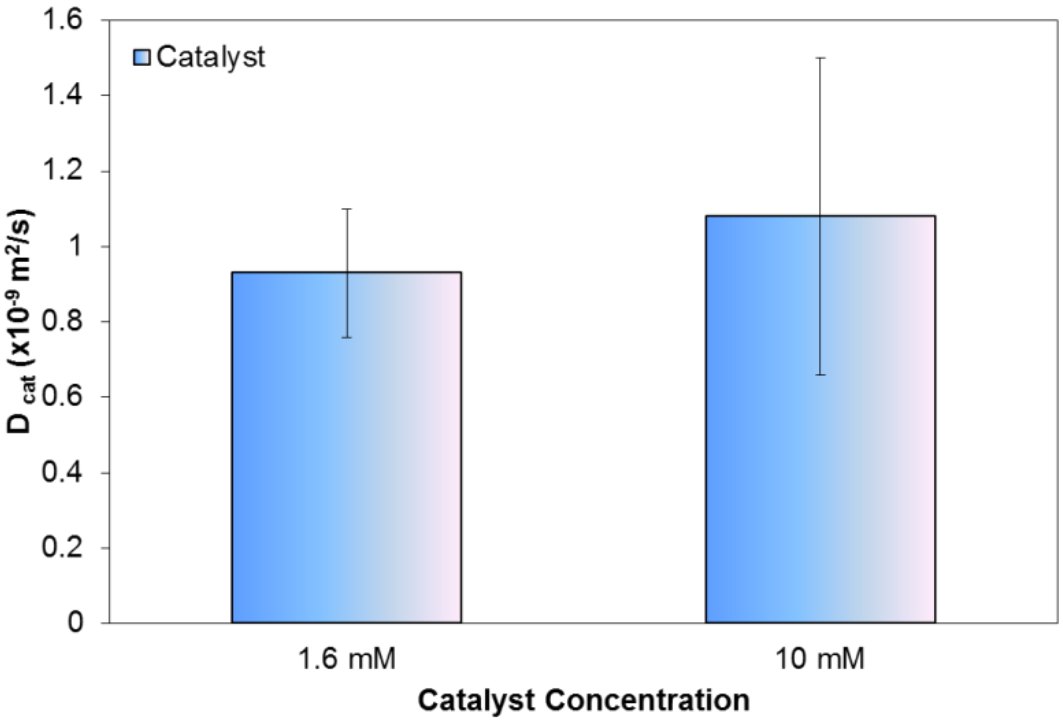

Figure 4-9. Diffusion of the catalyst as a function of catalyst concentration at a constant rate of 6.7 $x10^{-8}$ mol sub/ sec. There is no consistent trend between the diffusion and catalyst concentration suggesting that the number a reaction centers does not matter.

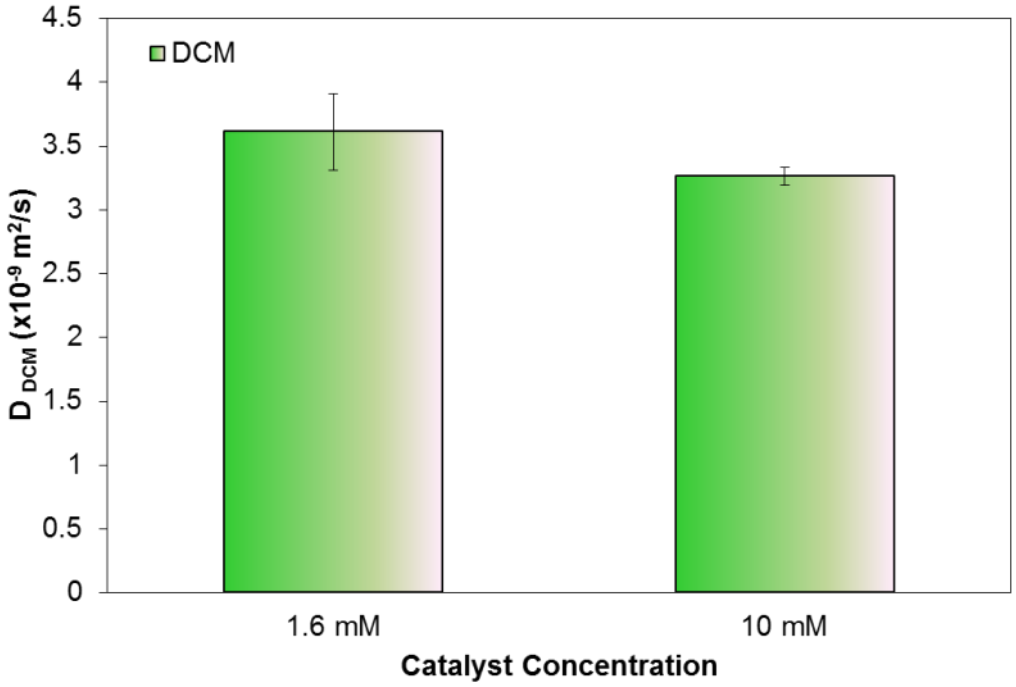

Figure 4-10. Diffusion of the spectator DCM as a function of catalyst concentration at a constant rate of 6.7 $x10^{-8}$ mol sub/ sec. There is no clear trend between the diffusion and catalyst concentration suggesting that the number a reaction centers does not matter.

4.8 Calculation of Power Output

A way to relate the observed diffusion to the energetics of the system is to calculate the power that is being generated. This is an important quantity because it does not only take into account the energy released but also the rate in which it is being released. Given a certain reaction rate (k) expressed as mol sub/s simply multiplying by the free energy of the reaction (ΔG), calculates the power released:

$$Power = k\ x\ \Delta G \quad (4\text{-}2)$$

The maximal diffusion increase for the catalyst is observed when the reaction rate in the system is 9.9 $x10^{-8}$ mol sub/s. The advantage of using this catalytic system is that we know the free energy that is released during the reaction, -2.3 kcal/ mol sub (9.6 $x10^{3}$ J/ mol sub).[10] So to observe the diffusion increase at this rate the catalyst needs to generate a power of 9.5 $x10^{-4}$ watts. This method is useful for potentially predicting the motion of motor systems.

4.9 Theory

The experimental observations discussed suggest the transfer of momentum from the active catalyst molecules to the surrounding medium. Although at this point it is not possible to comment on the underlying physics governing such momentum transfer, a number of possible mechanisms can be hypothesized. Recently, Pan et al. reported the existence of nonlinear instability in fluids above some critical flow conditions, even when the system is expected to be linear and dominated by viscous drag.[24] Our system may follow a similar physics, wherein, turbulence originating from the catalyst surface gets propagated across the system, introducing substantial non-linearity in its behavior. Also, owing to the comparable dimensions of the solvent, catalyst and tracer molecules, the solvent may help to efficiently transfer kinetic energy to the spectators, if their mutual interactions are assumed elastic, distributing the total momentum across the entire volume of observation. Another possibility is the propagation of nanoscale acoustic waves, generated through substrate turnover during a reaction cycle.

4.11 Conclusion

In conclusion, an ensemble of Grubbs' catalyst molecules have been shown to display dynamic coupling among each other, as well as the surrounding fluid. Our results show that active swimmers can interact with each other even at the molecular scale, a size regime that had not been previously explored. Interestingly, this system showed a near linear dependence of diffusion enhancement on the total disturbances in the system (number of reaction in the system per unit time), similar to the micron scale systems. The coupling was found to be strong enough to enhance the motion of objects much larger than the catalyst. This demonstrates that such coupling processes are *effective*, even at smaller length scales.

4.12 References

1. Ibele, M.; Mallouk, T. E.; Sen, A. *Angew. Chem. Int. Ed.*, **2009**, *48*, 3308.
2. Ibele, M.; Lammert, P.; Crespi, V.; Sen, A. *ACS Nano*, **2010**, *4*, 4845.
3. Kagan, D.; Balasubramanian, S.; Wang, J. Angew. Chem. Int. Ed. 2011, 50, 503.
4. Chwang, A. T.; Wu, T. Y. T, *J. Fluid. Mech.*, **1974**, *63*(3), 607.
5. Purcell, E. M., *Am. J. Phys.*, **1977**, *45* (1), 3.
6. Anderson, J. L., *Ann. Rev. Fluid. Mech.* **1989**, *21*, 61.
7. Mino, G.; Mallouk, T. E.; Darnige, T.; Hoyos, M.; Dauchet, J.; Dunstan, J.; Soto, R.; Wang, Y.; Rousslet, A.; Clement, E *Phys. Rev. Lett.* **2011**, *106*, 048102(1-4).
8. Kurtuldu, H.; Guasto, J. S.; Johnson, K. A.; Gollub, J. P. *Proc. Nat. Acad. Sci.* **2011**, *108*,10391.
9. Leptos, K. C.; Guasto, J. S.; Gollub, J. P.; Pesci, A. I.; Goldstein, R. E. *Phys. Rev. Lett.* **2009**, *103*, 198103 (1-4).
10. Pavlick, R. A.; Dey, K. K.; Sirjoosingh, A.; Benesi, A.; Sen, A. *Nanoscale*, **2013**, *5*, 1301.
11. Golestanian, R.; Liverpool, T. B.; Ajdari, A. *Phys. Rev. Lett.* **2005**, *94*, 220801 (1-4)
12. Ruckner, G.; Kapral, R. *Phys. Rev. Lett.* **2007**, *98*, 150603 (1-4)
13. de Buyl, P.; Kapral, R. *Nanoscale*. **2013**, *5*, 1337.
14. Co´rdova-Figueroa, U. M.; Brady, J. F. *Phys. Rev. Lett.* **2008**, *100*, 158303 (1-4)
15. Delogu, F. *J. Phys. Chem. C.* **2009**, *113*, 15909.
16. Ebbens, S.; Jones, R. A. L.; Ryan, A. J.; Golestanian, R.; Howse, J. R. *Phys. Rev. E.* **2010**, *82*, 015304(1-4).
17. Ke, H.; Ye, S.; Carroll, R. L.; Showalter, K. *J. Phys. Chem. A.* **2010**, *114*, 5462.
18. Wu, D.; Chen, A.; Johnson, C. S. *J. Magnetic Resonance, Series A.* **1995**, *115*, 260.
19. Sanford, M.S.; Love, J.A.; Grubbs, R.H. *J. Am. Chem. Soc.* **2001**, *123*, 6543.

20. Ishikawa, T.; Sekiya, G.; Imai, Y.; Yamaguchi, T. *Biophysics Journal*, **2007**, *93*, 2217
21. Kim, M. J.; Breuer, K. S. *Physics of Fluids*, **2004**, *16* (9), 78.
22. Drescher, K.; Goldstein, R. E.; Michel, N.; Polin, M.; Tuval, I. *Phys. Rev. Lett.* **2010**, *105*, 168101 (1-4).
23. Guasto, J.S.; Johnson, K. A.; Gollub, J. P. *Phys. Rev. Lett.* **2010**, *105*, 168102 (1-4).
24. Pan, L.; Morozov, A.; Wagner, C.; Arratia, P. E. *Phys. Rev. Lett.* **2013**, *110*, 174502 (1-4).

Chapter 5

Salt Triggered Detection and Polymer Deposition

5.1 Introduction

With the success of developing organometallic based motor systems, as shown in the previous chapters, the next step was to develop these systems towards useful applications. In this chapter a detection/ repair system was developed based on the knowledge acquired from these previous systems. Early polymer self-repair systems utilized an internal catalyst (Grubbs' Catalyst) and monomer (dicyclopentadiene, DCPD) embedded in the polymer itself to repair damage to the polymer.[1-4] More recent systems have utilized supramolecular interactions, photochemistry, and thermal heating to seal cracks.[5-7] However, these systems have rather long healing times. While the repair of microcracks and voids is well studied, little research exists on detecting their presence in materials. Examples from Pang and Bond have demonstrated that glass structures filled with a repair agent and UV dye imbedded in an epoxy resin could simultaneously leach dye to visualize the crack and epoxy to repair it.[8,9] This method suffers from two drawbacks: 1) it has a onetime use in a given location and 2) the stability of the UV dye will degrade over time if exposed to light. Recently a "repair and go" system was developed by Kolmakov et al. This system uses nanoparticle filled microcapsules to deliver nanoparticles to damaged areas in a polymer surface, allowing the damaged sites to be fluorescently detected.[10,11] One way to overcome the drawbacks in internal detection and repair is to use *external* components to detect and fix damage to a material. In this chapter, we present such a method

here that uses an aqueous solution containing either fluorescent quantum dots or emulsions with repair agents in combination with an appropriate coating to "find" cracks in a material.

Salt driven density flows can actively transport a detection material to its target. These flows occur when the salt concentration increases sufficiently to cause a local density change. These types of flows are very common in nature at mineral salt deposits and estuaries. Local fluid density varies with local salt concentration, causing flows dictated by the direction of gravity.[12-16] To make use of this mechanism, we embedded the salt into a polymer matrix creating an active coating. We chose to use calcium chloride ($CaCl_2$) because it is highly soluble in water (solubility= 74.5g/100ml at 20^0C)[17] and non-toxic. Calcium chloride crystals were embedded into a PDMS matrix, forming a composite material. Then the exposed surface was sealed with a thin layer of PDMS (Figure 5-1). When the surface is cracked, the calcium chloride begins to dissolve into solution creating a change in the local density.

For detection, we used a solution of fluorescent quantum dots (Q-dots). The solution was added to the damaged surface. As the salt leached out, the ionic strength increased, causing the particles' zeta potentials to drop. This drop decreases the repulsive forces between the particles, causing the Q-dots to aggregate at the damaged site. This focusing movement makes the fluorescence intensity inside the crack to be greater than that of the surroundings, allowing for detection. While effective for crack detection, this method does not repair the damage.

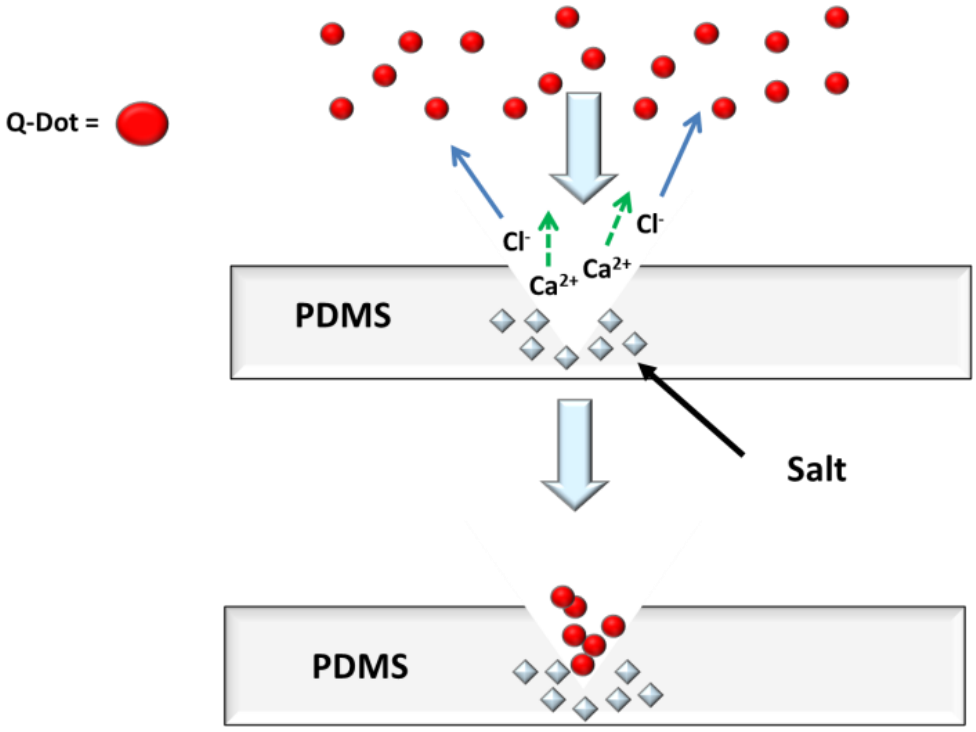

Figure 5-1: Diagram of the surface coating setup. The calcium chloride is mixed into a PDMS layer and sealed with a thin layer of PDMS. The surface is scratched, exposing the calcium chloride to the water causing an increase in the ionic strength. The quantum dots (Q-dots) then begin to aggregate due to the decreased electrostatic repulsion.

To perform repairs on the damaged site, we separated the polymerization catalyst and the monomer into two separate oil-in-water emulsions. The emulsion separation is itself important, for certain polymerizations occur too fast to allow adequate mixing of reactants, such as is seen in the well-known Grubbs' ring opening metathesis system. Thus, the development of latent catalytic polymerizations has been a prominent area of research.[18-22] When the surface of the

polymer is damaged, the salt is exposed, and addition of an aqueous solution generates density driven flows. This setup provided evidence towards a directed repair system, for as the flows circulate the emulsions over the crack, the high ionic strength at the damaged site causes the emulsions to break open and aggregate, allowing the catalyst and reactant to mix. This mixing causes polymer formation and deposition into the crack, repairing the damage (Figure 5-2).

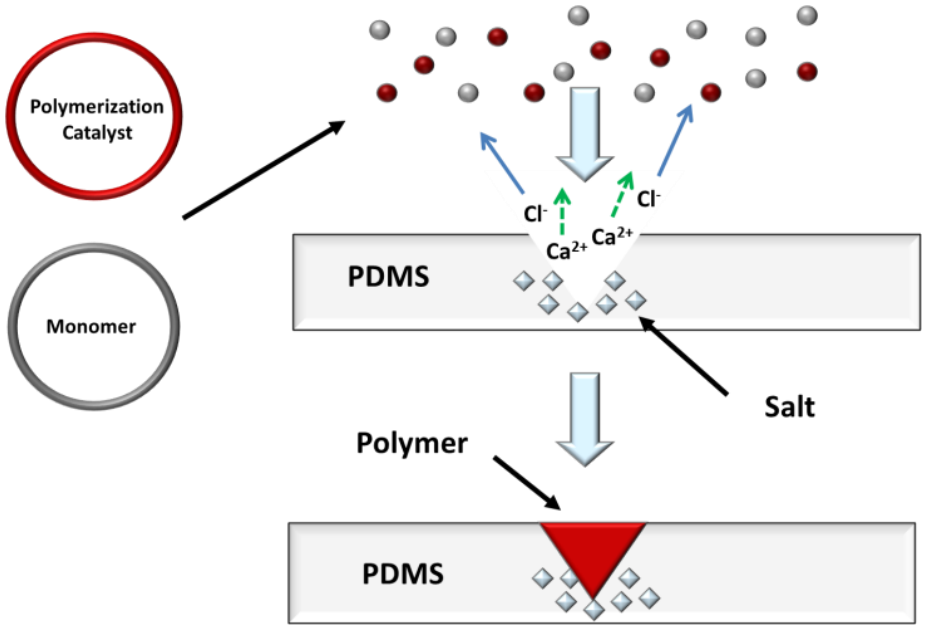

Figure 5-2: Schematic using salt/PDMS film as a coating for a repair system. The catalyst emulsions (red) and monomer emulsions (grey) flow over the crack due to density driven flows. At the crack the emulsion stability is perturbed due to the high ionic strength, and the emulsions begin to break apart and aggregate. This process causes polymer deposition.

5.2 Salt Flows

5.2.1 Coating Synthesis

The coating was first fabricated by mixing 10g of the PDMS precursor with 1g of crosslinker and 2.5g of finely ground $CaCl_2$. Then 3 g of this mixture was added to a 60x15mm polystyrene petri-dish and placed in a vacuum desiccator for 30 min. to remove bubbles from the mixture. The dish was then placed in an oven at 60^0C for 1 hr to cure the PDMS. Then 0.3 ml of a mixture of 10:1 PDMS and crosslinker was spin coated on top of the hardened PDMS. The coating was then again placed in the vacuum desiccators for 30 min. followed by curing at 60^0C for 30 min. A portion of the coating was cut out of the petri-dish and mounted onto a glass slide with epoxy.

5.2.2 Observation of Flows

The spacer gasket above the PDMS samples was then filled with the diluted emulsion mixture. The apparatus was inverted with the gasket face down, and the motion of the particles was recorded with an optical microscope (details) at 5x, 20x and 50x. Within 20 min of adding the particles, vigorous motion was detected in the vicinity of the crack and lasted over an hour.

A mixture of catalyst and monomer emulsions were inserted into spacers over PDMS/$CaCl_2$ that were cut with a scalpel. The width of the cuts ranged from 50-70μm, the length about 1 cm, and the depth about 1 mm. Upon exposure of the crack to the emulsion solution, unique flows were observed (Figure 5-3). The emulsions were seen to flow away from the crack close to the surface and towards the crack far from the surface at a speed of ~3.0±1 μm/s. Upon inverting the setup, the flow direction reversed such that the emulsions flowed

towards the crack at the surface and away from the crack far from the surface at a speed of ~4.0±1 μm/s (Figure 5-3). The flow directions were shown to be independent of tracer charge as identical patterns were observed for amine, carboxylate, and neutral polystyrene particles. This is indicative of a density driven flow, since the flow is dependent on the setup's orientation and not the charge of the tracers. These flows are useful in directing polymer deposition since they continuously transport emulsions near the crack.

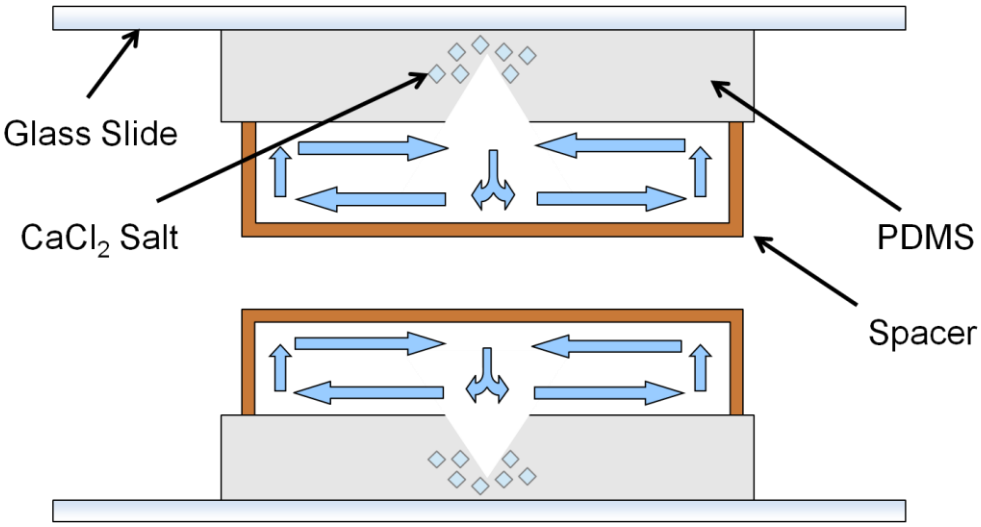

Figure 5-3: Inverted (top) and upright (bottom) setups showing the flow patterns (blue) caused by the salt leaching. The dependence of the flow direction on gravity suggests the flows are density driven.

5.3 Quantum Dot Based Detection

5.3.1 Confocal Experiments

10 μl of an 8 μM stock 655nm excitation quantum dot solution (amine or carboxylated) was first diluted to 1000 μl. The solution was added to the gasket on top of the coating until the gasket was filled. Then the gasket was sealed. The setup was inverted and then placed on the microscope. The fluorescence intensity was monitored at the crack with a 10x objective both as a function of time (every 10 min.) after an initial time of 5 min.

The surface was first scratched with a scalpel, forming a crack as discussed earlier. The damaged PDMS/$CaCl_2$ sample was then covered with a spacer. 0.16 μM of 20 nm carboxylated quantum dots was then added to the spacer. Using confocal microscopy, the fluorescence intensity at the crack was monitored over time.

The fluorescence intensity of carboxylated quantum dots remained approximately the same inside the crack, but the fluorescence around the crack decreased over time (Figure 5-4). This process is quantitatively shown by calculating the intensity ratio, which is defined as the fluorescence inside the crack is divided by the intensity 100 μm from the crack. At 5 min the ratio is 1; this increases to 13 after 35 min, an over one magnitude increase (Figure 5-5). This allows for easy detection of the crack. This phenomenon is seen in optical images of the cracks where, with salt, the quantum dots aggregate around the crack making it easy to distinguish (Figure 5-6). When the quantum dots were added over a sample containing no salt, there was no significant change in fluorescence intensity over time (Figure 5-7).

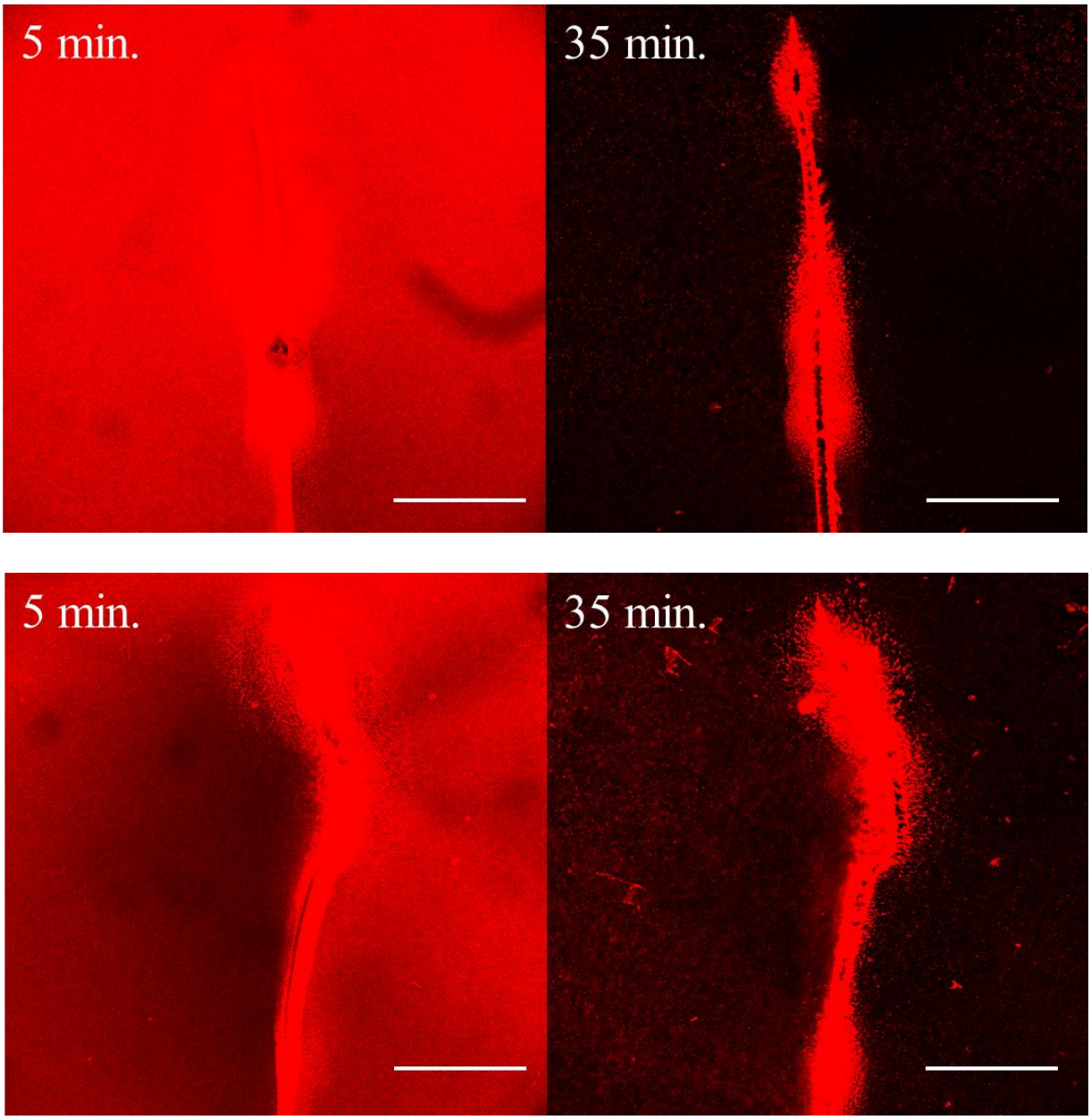

Figure 5-4: Fluorescence confocal imaging of the crack at 5 min and 35 min (Scale bar = 325 μm). The fluorescence intensity remains constant in the crack while the quantum dots outside the crack move away around the crack, showing a more defined fluorescence from the damaged site.

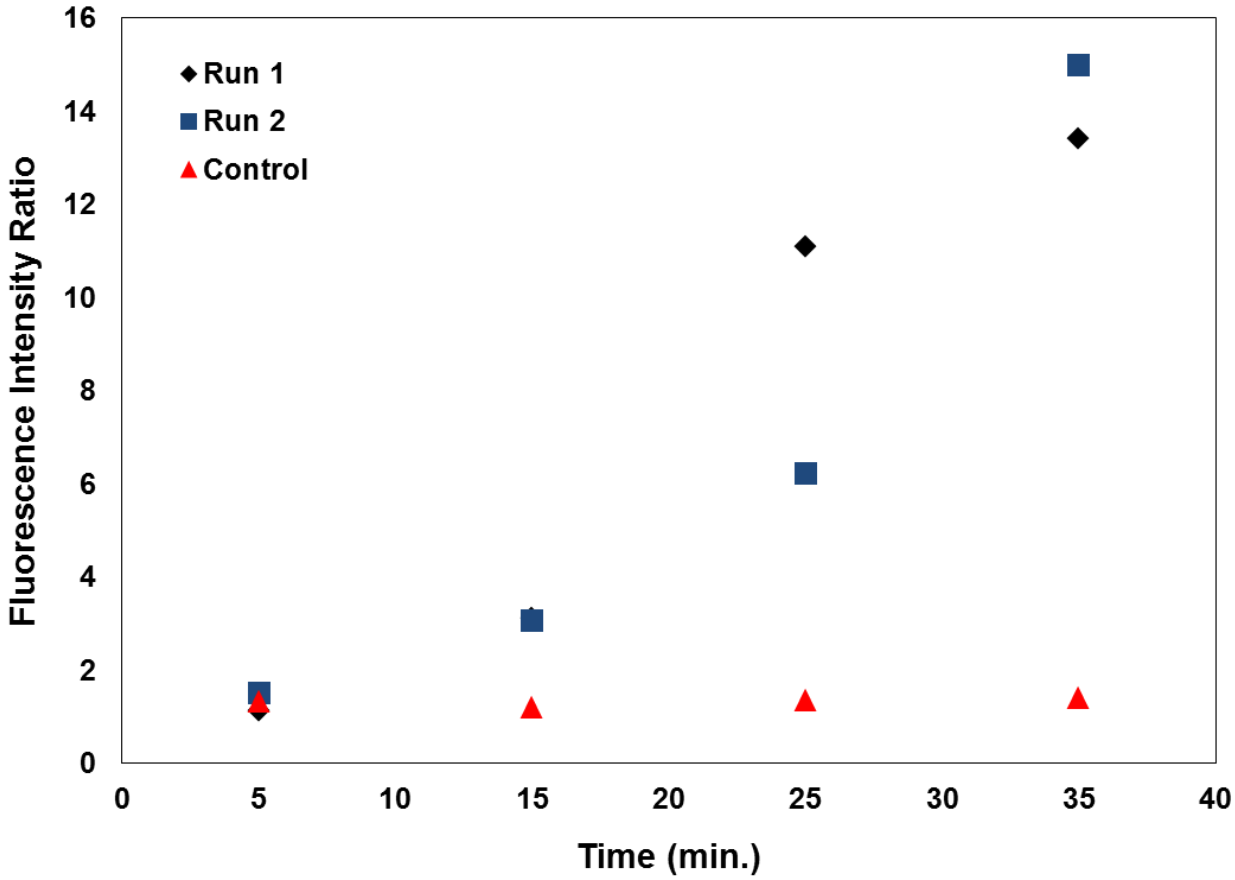

Figure 5-5. Fluorescence intensity ratio of the intensity in the crack divided by the intensity 100 μm away from the crack as a function of time. Run 1 shows the ratio change for the images in Figure 5-4. Run 1 and the control dhows the ratio change for the images in Figure 5-7. The ratio in run 1 increases linearly while in run 2 the increase is slightly exponential. However, the control shows no significant increase.

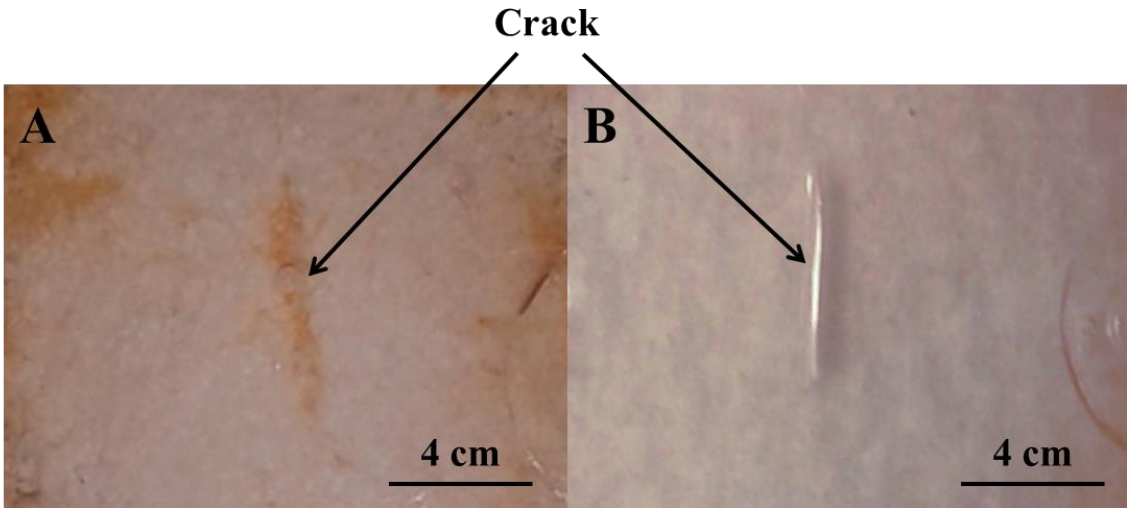

Figure 5-6: Image of the crack with a quantum dot solution a) with and b) without $CaCl_2$ after 1 hour. The quantum dots clearly concentrate at the crack when there is salt.

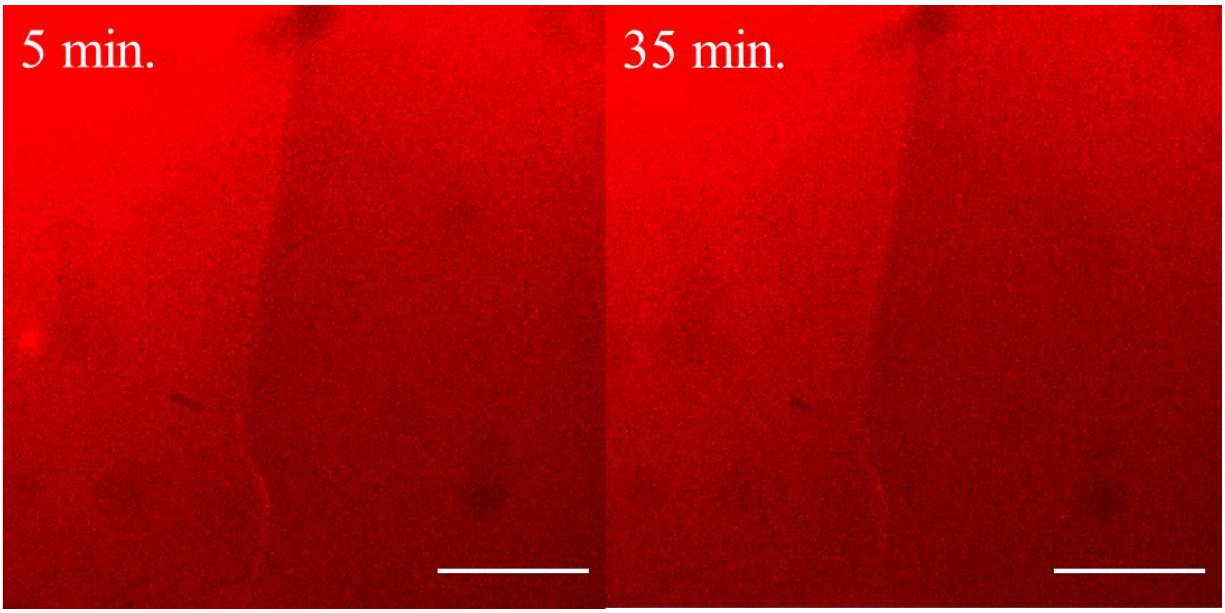

Figure 5-7: Fluorescence confocal images of carboxylated quantum dots over a crack in pure PDMS over time (Scale bar = 325μm). The fluorescence in and around the crack does not change with time.

Aggregation around the crack occurs because the high salt concentration causes the zeta potential of the particles to drop, decreasing the electrostatic repulsion between the particles. Particles further away from the crack seem to be transported away from the crack, most likely from the density flows.

5.4 Repair of Damaged Polymer Film

5.4.1 Emulsion Fabrication

Two different emulsions were fabricated. The catalyst emulsions were made by adding a 5% solution of Grubbs' 2nd generation catalyst in 1,1,2-trichloroethane to a solution of water with oleic acid. Two 1 mL centrifuge tubes were filled with 450 μL nanopure H_2O and 20 μL oleic acid. One tube was then filled with 40 μL 5% Grubbs' 2nd Generation Catalyst in 1,1,2-trichloroethane. To the other tube 40 μL dicyclopentadiene, heated to 43°C, was added. The tubes were then emulsified for 200 seconds each forming the emulsions, Figure 5-8. The emulsions ranged from 2 to 5μm in diameter. Finally, the catalyst emulsion solution and the monomer emulsion solution were combined. For microscopy experiments, this mixture was diluted until the solution became translucent. For the deposition experiments, the solution was used without dilution.

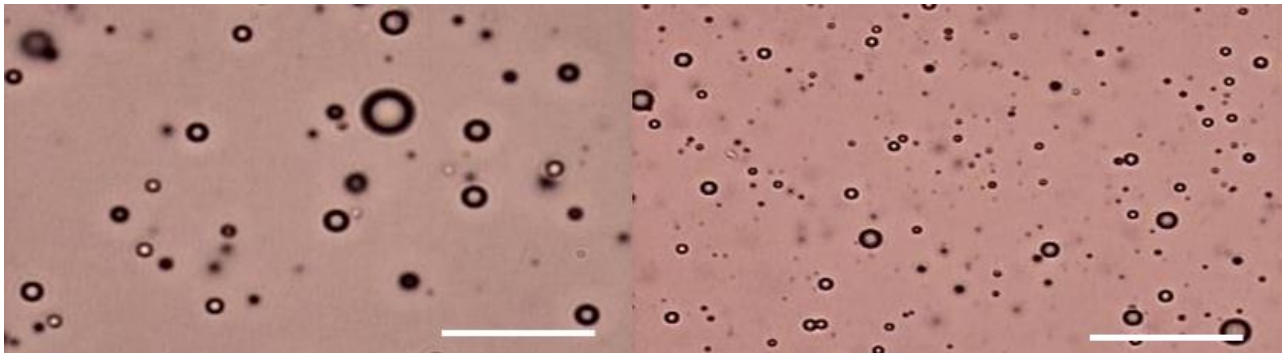

Figure 5-8: Optical Images of oil in water emulsions containing dicyclopentadiene (left, scale bar = 25 μm) and Grubbs' 2nd generation catalyst (right, scale bar = 50 μm).

5.4.2 Stability of Emulsions in Varying Ionic Strengths

The instability of emulsions in high ionic strength is an important component in the overall scheme. To evaluate exactly how the salt perturbs the stability of the emulsions, the emulsions were suspended in solutions ranging from 0 M to 1 M $CaCl_2$ and allowed to sit for 1 hour. As the salt concentration increased, fewer emulsions were observed and more floating polymer deposits were observed. The number of emulsions was counted in each solution, and a clear decrease in emulsion concentration is observed as a function of salt concentration (Figure 5-9a). The instability was noticeable after 20hrs, where the 0 M solution still looks turbid but the solutions from 0.1 M to 1 M were clear and show deposits floating on top (Figure 5-9b). This perturbation occurs because, as the ionic strength increases, the zeta potential decreases, lowering the repulsive forces between emulsions. This loss in repulsive forces allows the emulsions to begin to coalesce and flocculate, causing the reactants to mix.[23]

A

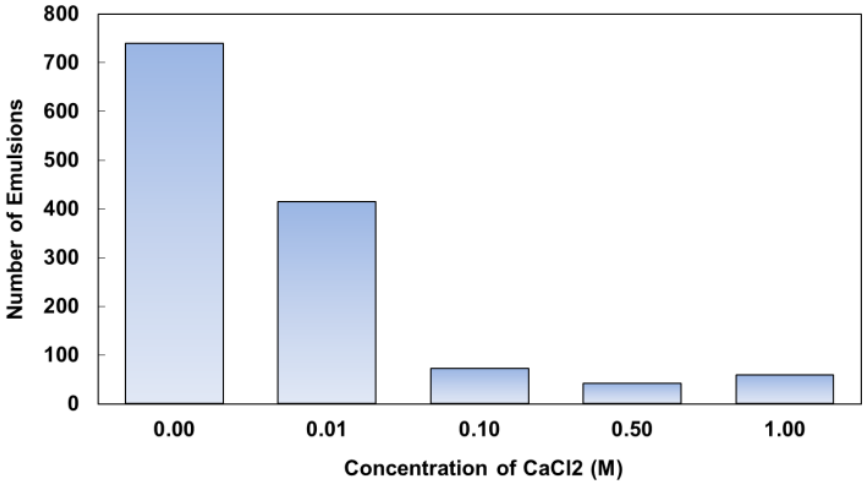

B

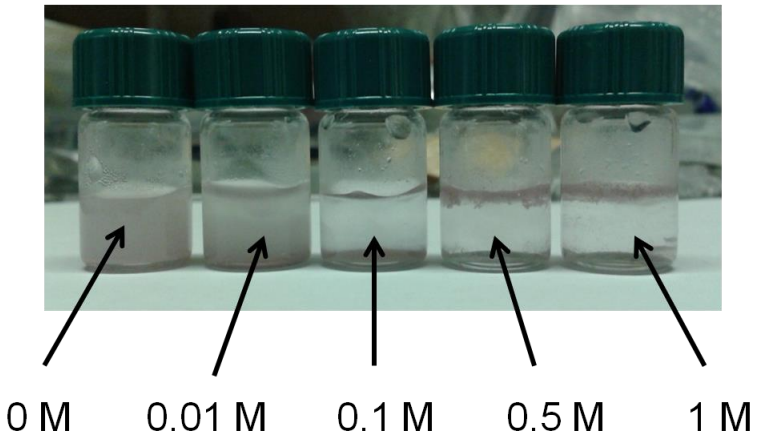

Figure 5-9: a) Graph displaying the number of particles observed at 100x as a function of concentration. There is a clear dramatic drop in concentration as the $CaCl_2$ concentration approaches 0.1 M. c) Picture of the solution of oil-in-water emulsions after 20 hrs. The 0M and 0.01M salt solutions are still turbid while the high salt concentrations are clear and show floating polymer deposits.

5.4.3 Salt Triggered Polymer Deposition

Since the basic principles of this method were successful, we chose to apply them to a polymer repair system. A mixture of catalyst and monomer emulsions were introduced into the spacers over PDMS/$CaCl_2$ samples that where cut using a scalpel as with the detection setup. Two setups were tested; one inverted and one upright, since different orientations cause different flows. The spacers were then removed after 1 hr. and the samples dried and studied with an environmental scanning electron microscope (ESEM) (Figure 5-10). A control was run by just adding the emulsion solution over a cut in PDMS. This experiment showed very little polymer deposits overall and no polymer deposition in the crack.

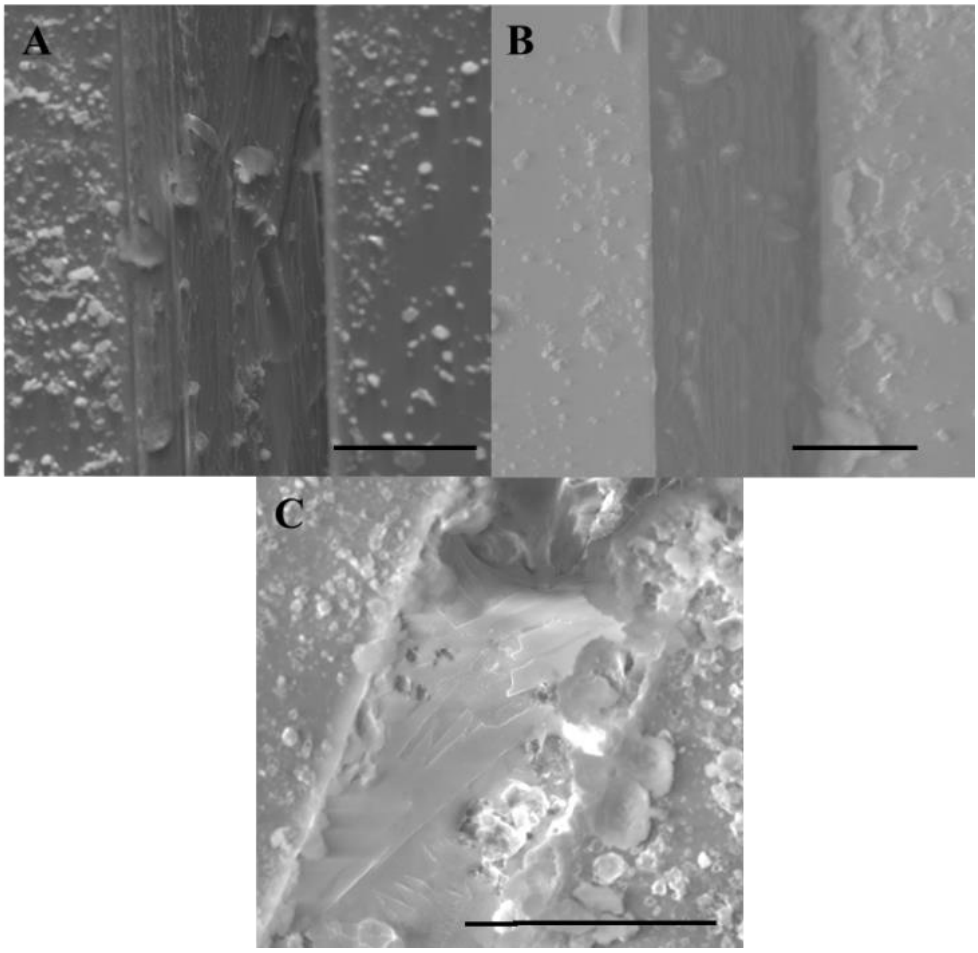

Figure 5-10: ESEM images of selected areas of the cut showing polymer deposition (Scale bar = 50 μm). a) The image of cut before treatment with emulsions. b) Cut in polymer with no salt c) $CaCl_2$ inverted after 1hr exposure to emulsions.

The samples showed partial filling of the crack. Moreover, certain areas, especially those near the edges of the crack, showed complete deposition. Visually, it is observed that the deposition was centered around the crack. Deposition was more complete in the inverted

samples, since the flow at the surface was directed towards the crack. Micro AT-IR was used to analyze the polymer deposits.

5.4.4 Analysis of Polymer Deposition via Micro AT-IR

IR measurements were performed on a Hyperion 3000 FT-IR Microscope with a 20x attenuated total reflectance objective using a germanium crystal. The crystal was placed in the crack and the IR spectrum was collected. This was done for samples before and after polymerization. The IR showed key peaks for polyDCPD at 1665 cm^{-1} and 956 cm^{-1} for the acyclic C=C and acyclic =C-H respectively.(Figure 5-11).[24,25]

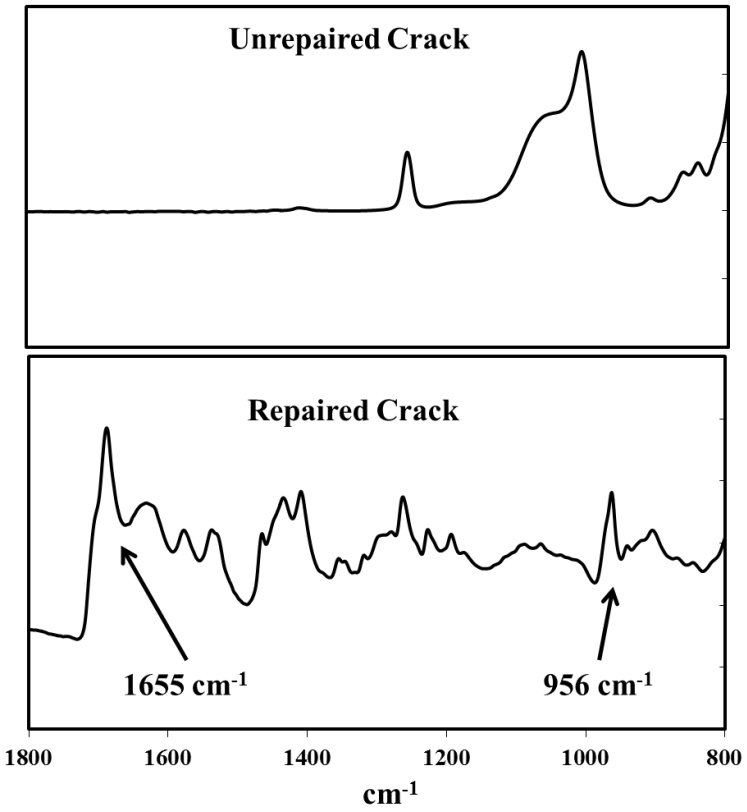

Figure 5-11: Micro AT-IR spectrum showing key peaks for polyDCPD (1665 cm^{-1} and 956 cm^{-1} for the acyclic C=C and acyclic =C-H respectively) compared to the flat spectrum for the unrepaired crack.[24,25]

5.5 Conclusions

These salt powered systems have been shown to be useful for both crack detection and repair processes. The flows generated by the salt direct the quantum dots and emulsions towards the crack without the addition of an external energy source. The high ionic strength focuses the Q-dots at the site of damage for both fluorescent and visual imaging. The salt triggered polymerization system is a useful method for directed deposition and crack repair. External reactant delivery facilitates the use of reagents that do not have long shelf lives. This method is useful for coatings on materials that are not easy to remove and repair. Lastly, this methodology is easily transferable to different host polymers and other catalyst/monomer systems. Future systems will improve the deposition process and allow for restoration of the polymer properties.

5.6 References

1. White, S. R.; Sottos, N. R.; Geubelle, P.H., Moore, J.S.; Kessler, M. R.; Sriram, S. R.; Brown, E. N.; Viswanathan, S. *Nature,* **2001**, *409*, 794.
2. Kessler, M.R.; Sottos, N.R.; White, S.R. *Composites: Part A*, **2003**, *34*, 743.
3. Jones, A.S.; Rule, J.D.; Moore, J.S.; White, S.R.; Sottos, N.R. *Chem. Matter.*, **2006**, *18*, 1312.
4. Rule, J.D.; Sottos, N.R.; White, S.R. *Polymer*, **2007**, *48*, 3520.
5. Wu, D.Y.; Meure, S.; Solomon, D. *Prog. Polym. Sci.*, **2008**, *33*, 479.
6. Nosonovsky, M.; Amano, R.; Lucci, J.M.; Rohatgi, P.K.. *Phys. Chem. Chem. Phys.*, **2009**, *11*, 9530.
7. Wojtecki, R.J.; Meador, M.A.; Rowan, S.J. *Nature Mater.*, **2011**, *10*, 14.
8. Pang, J.W.C.; Bond, I.P. *Compos. Sci. Technol*., **2005**, *65*, 1791.
9. Pang, J.W.C.; Bond, I.P. '*Composites: Part A*, **2005**, *36*, 183.
10. Kolmakov, G.V.; Revanur, R.; Tangirala, R.; Emrick, T.; Russell, T.P.; Crosby, A.J.; Balazs, A.C. *ACS Nano*, **2010**, *4*, 1115.

11. Kratz, K.; Narasimhan, A.; Tangirala, R.; Moon, S.C.; Revanur, R.; Kundu, S.; Kim, H.S.; Crosby, A.J.; Russell, T.P.; Emrick, T.; Kolmakov, G.; Balazs, A.C. *Nature Nanotech.*, **2012**, *7*, 87.
12. Middleton, G.V. *CJES*, **1966**, 3, 523.
13. Anderson, R.Y.; Kirkland, D.W. *Geol.*, **1980**, 8, 66.
14. Devantier, B.R.; Larock, B.E. *Int. J. Numer. Meth. Fluids*, **1986**, *6*, 241.
15. Linden P.F.; Simpson. J.E. *J. Fluid Mech.*, **1986**, *172*, 481.
16. Alavian, V. *J. Hydraul. Eng.* **1986**, 112, 27.
17. Lide D.R.; CRC Handbook of Chemistry and Physics, 87th Edition, 8-54.
18. Ben-Asuly, A.; Tzur, E.; Diesendruck, C. E.; Sigalov, M.; Goldberg, I.; Lemcoff, N.G. *Organometallics*, **2008**, *27*, 811.
19. Monsaert, S.; Vila, A.L.; Drozdzak, R.; Van Der Voort, P.; Verpoort, F. *Chem. Soc. Rev.* **2009**, *38*, 3360.
20. Drozdzak, R.; Nishioka, N.; Recher, G.; Verpoort, F. *Macromol. Symp.* **2010**, *293*, 1.
21. Thomas, R.M.; Fedorov, A.; Keitz, B.K.; Grubbs, R.H. *Organometallics*, **2011**, *30*, 6713
22. Ernst, C.; Elsner, C.; Prager, A.; Scheibitz, B; Buchmeiser, M.R. *J. Appl. Polym. Sci.*, **2011**, *121*, 2551.
23. Washingtion, C. *Adv. Drug Deliv. Rev.*, **1996**, *20*, 131.
24. Jeong, Y.; Duncan, B.; Park, M.H.; Kim, C.; Rotello, V.M. *Chem. Commun.*, **2011**, *47*, 12077.
25. Dragutan, V.; Dragutan, I.; Dimonie, M. Green Metathesis Chemistry, NATO Science for Peace and Security Series A: Chemistry and Biology, **2010**, 369.

Chapter 6

Conclusions

Organometallics as a catalytic power source has been demonstrated in several motor-type systems. Through attachment to a bead and as a single molecules Grubbs' catalyst has particularly been a useful resource for its high catalytic activity, stability, and variety in the reactions it can accomplish. Novel phenomenon has also been observed in these systems including non-biological chemotaxis and dynamic coupling of momentum. Furthermore, these principles have inspired a materials repair and detection system.

Attaching a catalytic source asymmetrically to a bead allows propulsion of the bead through a phoretic mechanism. The exact mechanism, however, can only be theorized since the small scale of the motor makes it hard to probe. Though not very efficient, the motor still displays an increase of nearly 70% supporting organometallics as a viable catalytic source. With further design and optimization this motor-type will be improved to achieve even greater enhancement and directionality. The chemotactic component of this motor is important, since this is only the second system to show chemotaxis outside of biology. Though this mechanism seems to be slow acting, it does allow for directing these motors. A useful enhancement that should be made on this system is to allow its operation in an aqueous environment, which is a more flexible solvent system.

A sub-nanometer molecular motor is a powerful advance in motors research for it allows an in-depth look at not only how catalytic sources work but also what is happening during a

catalytic reaction. When Grubbs' performs a reaction that produces a non-equal distribution of reactants and products a diffusion increase of over 2 times is observed. This enhancement makes these molecules useful as a motor system and provides information on how catalysts behave during reaction. The latter is useful when considering reaction kinetics, especially when discussing diffusion limited reactions. However, this enhancement is only observed at certain concentrations where the overall reaction rate is high enough. Therefore, this motion is a collective phenomenon rather than a single molecule phenomenon. This circumstance is interesting in itself for this collective behavior is theorized to be caused from momentum transfer of the reaction force to the surrounding environment. The enhancement of the motion of spectators in solution supports the fact that the environment is being effected by the reaction. The exact pathway through which this is occurring, however, is still a mystery. A more theoretical framework needs to be developed to shed some light on this phenomenon.

Developing applications for motor systems is an important step for the development of the field. While the repair/detection system described in chapter 5 does not directly use organometallics as the power source for motion, it does still exploit their catalytic behavior. Moreover, it utilizes a density driven salt flow, a mechanism that has not been explored in the motors field. The methodology of the system is powerful in its generality and flexibility allowing for both detection and repair depending on the solution that is used. To be more valuable, the repair solution needs to be tuned to the substrate to allow for repair of the substrates properties. The current system only allows for a more cosmetic repair that can reduce the proliferation of future damage. Still, this is a great step for giving applications to motor systems.

Motors research, in general, is a novel field still in its infancy. Work still needs to be pursued in understanding motor mechanisms, exploring new power sources, and developing applications for known/future systems. However, effort so far has bared valued and novel observations that have spiked interest in the field. With this immense interest in this field important breakthroughs are surely only around the corner.

VITA

Ryan A. Pavlick

Ryan Anthony Pavlick was born in Bayonne, New Jersey on August 5th 1987 to William and Marylin Pavlick. He grew up an only child in East Brunswick, New Jersey. He was always interested in science even from a young age. Probably the first moment was in the 5th grade where each pair of students had to assemble and design a rocket. His was black with a silver nozzle. It crashed head first into the ground when the parachute failed to open. It was awesome. From there his interest in science rose as he succeeded in his physics, chemistry, and biology courses. Initially wanting to be a lawyer, his interest drifted towards forensics. Seeking to be a forensic scientist he chose a major in chemistry at The College of New Jersey. Over the four years, his interests shifted to more inorganic chemistry and a desire to expand his knowledge beyond a Bachelorette level. After advisement by Dr. Georgia Arvanitis and Dr. Benny Chan he chose and was accepted to the PhD chemistry program at the Pennsylvania State University. There he researched nanoscale motors and their applications under Dr. Ayusman Sen. After completion of his PhD he moved on to industry accepting a position at the Intel Corporation as a process engineer.